A NOVEL DI-IRON LIGAND COMPLEX FOR WATER OXIDATION CATALYSIS AND THE DEVELOPMENT OF BIS-BIPYRIDINIUM-BASED GEMINI SURFACTANTS FOR TEMPLATE-DIRECTED SELF-ASSEMBLY

A Thesis

by

HA HOANG TRAN

BS, Texas A&M University-Corpus Christi, 2020

Submitted in Partial Fulfillment of the Requirements for the Degree of

MASTER OF SCIENCE

in

CHEMISTRY

Texas A&M University-Corpus Christi
Corpus Christi, Texas

August 2022

August 2022

A NOVEL DI-IRON LIGAND COMPLEX FOR WATER OXIDATION CATALYSIS AND THE DEVELOPMENT OF BIS-BIPYRIDINIUM-BASED GEMINI SURFACTANTS FOR TEMPLATE-DIRECTED SELF-ASSEMBLY

A Thesis

by

HA HOANG TRAN

This thesis meets the standards for scope and quality of
Texas A&M University-Corpus Christi and is hereby approved.

Mark A. Olson, PhD
Chair

Fereshteh Billiot, PhD
Co-Chair

Nicolas E. Holubowitch, PhD
Committee Member

August 2022

ABSTRACT

This thesis reports the designs and synthetic routes for a variety of organic molecules that served as the starting materials for the construction of supramolecular complexes via non-covalent interactions. The first project involved the development of a rationally designed dinucleating ligand that would form various stable diiron complexes as potential water oxidation catalysts (WOCs). The WOCs can promote the clean production of hydrogen gas, a green and potential fuel to replace traditional carbon-based fuels, by lowering its cost and increasing its efficiency. The second research project focused on synthesizing novel bis-bipyridinium-based gemini amphiphiles that were capable of self-assembling or co-assembling with a template molecule (the neurotransmitter melatonin) to form π-π donor-acceptor charge-transfer complexes. This research provided fundamental insights into the structure-property relationships between the amphiphiles and their self-assembly processes which are important for developing methodology that uses self-assembly to construct complex stimuli-responsive functional molecular architectures. The target compounds, which include the ligand and gemini amphiphiles were synthesized using a two-step S_N2 route. Supramolecular complexes were formed from the combination of two species (1^{st}: the ligand and an iron salt, and 2^{nd}: the amphiphile and the template). The obtained compounds were characterized by various techniques including ^{1}H-NMR, ^{13}C-NMR, 2D-COSY, 2D-HSQC, and TOF-ESI-MS. The synthesis of the ligand was achieved with a yield of 86% for the 1^{st} step and 45% for the second step. The ligand was later used to form diiron complexes which can be great WOCs due to their ability to form high valent intermediates for O-O bond formation. The synthesis of the gemini amphiphiles had a yield of 62% for 1^{st} step and 62 – 79% for the 2^{nd} step. The formation of π-π donor acceptor charge transfer complexes were verified by UV-Vis, ^{1}H-NMR, 2D-ROESY NMR, and 2D-DOSY NMR. Melatonin demonstrated its ability

to serve as “molecular glue” that can minimize the Coulombic repulsion among positive charged tetracationic gemini amphiphiles as they underwent self-assembly. This resulted in 1) the formation of larger aggregates; 2) a more thermodynamically favorable self-assembly process; and 3) an overall increase in the efficiency of the amphiphiles to self-assemble into micellar superstructures at lower concentrations.

DEDICATION

To my beloved parents, I am grateful for the life you have gifted me. Your love is my strength and motivation. Sometimes I am not sure if I deserve this enormous and powerful love. Life is so hard without your nearby presence. I love you to the moon and back!

To Ms. My Kim, Truc La, Duy Le, Maryam Tolentino, Demori E. Lawrence, Lien Hankins, Adam Hankins, and Ajitha Chandrika Prasanna Kumaran, you are my second family in Corpus Christi. Although we are not bonded by blood somehow, fate has brought us together. Thank you for not letting go of my hand at my darkest times. Thank you for accepting me as who I am and treating me with patience and kindness.

To all my family members, teachers, and friends in Viet Nam and Corpus Christi, I am thankful for our encounter in this giant world with 7 continents, 193 countries, and more than 7.7 billion people. Life works in such a magnificent way!

Without all of you, I cannot be the person I am today. You are my inspiration and reason why I have learnt to appreciate life, face all my difficulties and challenges, and grow as a person. You taught me about love, gratitude, kindness, forgiveness, and selflessness. I feel blessed that you have placed my name in your prayers! I dedicate my thesis to all of you.

ACKNOWLEDGEMENTS

I am thankful that I am able to finish my thesis. First, I would like to acknowledge the supports that I have received from Texas A&M University, Corpus Christi, and the Chemistry Department. I have been granted the opportunity to be a Teaching Assistant, which provided me a chance to build my teaching skills, leadership, and responsibilities. I appreciate all the financial supports I have been granted, including Welch's fellowship and other scholarships.

I have been very fortunate to receive precious guidance from my committee chair, Dr. Mark Olson, who always pushes me to step out of my comfort zone and challenge myself. I want to thank Dr. Mark Olson for teaching me essential skills and work ethics as a chemistry researcher. I am grateful for advice from Dr. Fereshteh Billiot, Dr. Nicolaus Holubowitch, Dr. Eugene Billiot, and Dr. Hussain Abdulla. Without it, I could not make progress and finish my thesis project. I thank my ex-chair, Dr. Jai Prakash, for teaching me a foundation in research and lab skills from which I continue to develop a better understanding of chemistry.

Last but not least, I would like to acknowledge all my past and current lab mates: Michael Kayne, Uyen Le, and Vandan Jakharia, for their assistance and cooperation. Furthermore, I am greatly thankful for the technical support I received from other friends: Huyen Bui, Alexis Burghoff, and Justin Elliot.

TABLE OF CONTENTS

PAGE

LIST OF FIGURES

Page

LIST OF TABLES

Page

CHAPTER I

REVIEW OF IRON COMPLEXES AS WATER OXIDATION CATALYSTS FOR ENERGY APPLICATIONS

1. Introduction

For a prolonged period, fossil fuels such as oil, coal, and natural gas have been humans' primary energy sources. However, the fossil fuels will be exhausted in the future because energy consumption is increasing every year, while it takes millions of years for fossil fuels to regenerate.[1] The burning of fossil fuels has sped up the rate of global warming by producing greenhouse gases such as carbon dioxide, carbon monoxide, water vapor, and nitrous oxide. All of which cause adverse consequences on our environments, including ice melting in polar regions, increasing acid rain showers, and more frequent and severe weather.[2,3] Hence, it is critical to develop alternative fuels that are clean, inexpensive, and renewable to replace fossil fuels. Hydrogen fuel is one promising candidate that can meet these requirements. It can be produced from the oxidation of water, a theoretically emissions-free process. Many efforts have been made to increase the efficiency and lower the cost of production through the development of iron complexes as WOCs. This chapter provides the fundamental understandings of hydrogen fuels, their green production, and the development of iron complexes as WOCs.

2. Literature Review

2.1. Hydrogen Fuels: Their Potential and Challenges

Hydrogen fuel has many advantages that make it a promising option to displace fossil fuels. First, hydrogen's sources are plentiful as hydrogen atoms make up 75% of the universe and are also one of the most abundant elements in the Earth's crust.[3] Hydrogen fuel can be extracted from multiple sources such as water, natural gas, or biomass.[3] Second, it is a non-toxic, safe, and clean

fuel for both human health and the environment.[3] Unlike fossil fuels, the usage of hydrogen releases only water as a by-product.[3,4] Third, hydrogen has a very high energy content, although its formula is the simplest among other fuels, making it a very efficient fuel. Liquid hydrogen has been used by the United States National Aeronautics and Space Administration (NASA) to power space shuttles and rockets since the 1970s.[5] The energy contained in hydrogen fuel (119,600 kJ/kg) is about double that in JP-8 (43,190 kJ/kg), a fossil fuel used widely in aircraft.[4] Finally, hydrogen is extremely flammable which means for its combustion process to start, only a small amount of energy needs to be used.[4]

Unfortunately, hydrogen fuel has some disadvantages which prevent it from being practical for daily energy consumption. First, it is challenging to store and transport hydrogen fuel because hydrogen has a very low density (0.09 kg/m^3) compared to other fuels like gasoline (750 kg/m^3) or JP-8 (800 kg/m^3).[2] The storage and transportation of hydrogen always require high pressure and low temperature to keep it in its liquid state.[3] Its extreme flammability is also a potential danger.[3] Another disadvantage lies in the production of hydrogen. Hydrogen gas cannot be obtained directly from nature but only be harnessed from substances containing it like water or organic compounds.[3] The current hydrogen production processes strongly depend on fossil fuels. The usage of fossil fuels (natural gas, off-gas, and coal) as chemical feedstocks or process fuels contributes up to 96% of hydrogen produced globally due to the low cost and large scale of production.[6,7] Only a small percentage of hydrogen is produced from water and this process still largely relies on electricity generated from fossil fuels.[6]

2.2. Green Hydrogen Production

Hydrogen fuel can be produced from water through a water-splitting process in which water molecules are split into H_2 and O_2 (equation (1)).[8] Water splitting contains two half-

reactions: H_2 formation (equation (2)) and water oxidation (equation (3)).[8] The process emits no greenhouse gases that are harmful to the environment. Moreover, water is plentiful on the earth and hence acts as a cheap raw material for this process. Water-splitting has been considered as a possible sustainable energy source which can help to solve the world energy crisis and environmental deterioration.

$2H_2O \rightarrow 2H_2 + O_2 \qquad \Delta G^0 = 4.92$ eV (113 kcal mol^{-1}) Equation (1)

$4H^+ + 4e^- \rightarrow 2H_2$ Equation (2)

$2H_2O \rightarrow O_2 + 4H^+ + 4e^- \qquad E^0 = 1.23$ V Equation (3)

Unfortunately, it is not easy to obtain hydrogen fuel from this method. The water oxidation reaction poses a huge challenge for chemists because the reaction involves a net transfer of four electrons, a cleavage of four O-H bonds, and a formation of an oxygen-oxygen double bond which demands very high energy and is associated with high redox potentials.[8,9] Therefore, it is essential to develop inexpensive and efficient WOCs so that hydrogen fuel can become more applicable and practical.

2.3. The Oxygen Evolving Complex, an Inspiration for Artificial Water Oxidation Catalysts

Nature has shown humans how water can be oxidized efficiently during photosynthesis, a process in which cyanobacteria, algae, and plants use sunlight to synthesize carbohydrates and dioxygen (O_2) from carbon dioxide and water.[10] Water oxidation is catalyzed by the oxygen-evolving complex (OEC) of photosystem II located in the thylakoid membranes of these photosynthetic organisms.[11] The complex can catalyze the water oxidation reaction at a low overpotential (<200 mV) and yield about 100-300 O_2 molecules per second (Turnover frequency (TOF) = 100-300 s^{-1}) with an estimated turnover number (TON = mol O_2 produced per mol of catalyst used) of about 500,000.[12] The OEC has inspired scientists to develop artificial WOCs to

convert solar energy into chemical fuels. The structure of OEC has been studied extensively by X-ray crystallography and its active site was reported to have a tetra-manganese complex, Mn_4CaO_5, supported by six carboxylates, one imidazole, and four water molecules (**Figure 1**).[13,14]

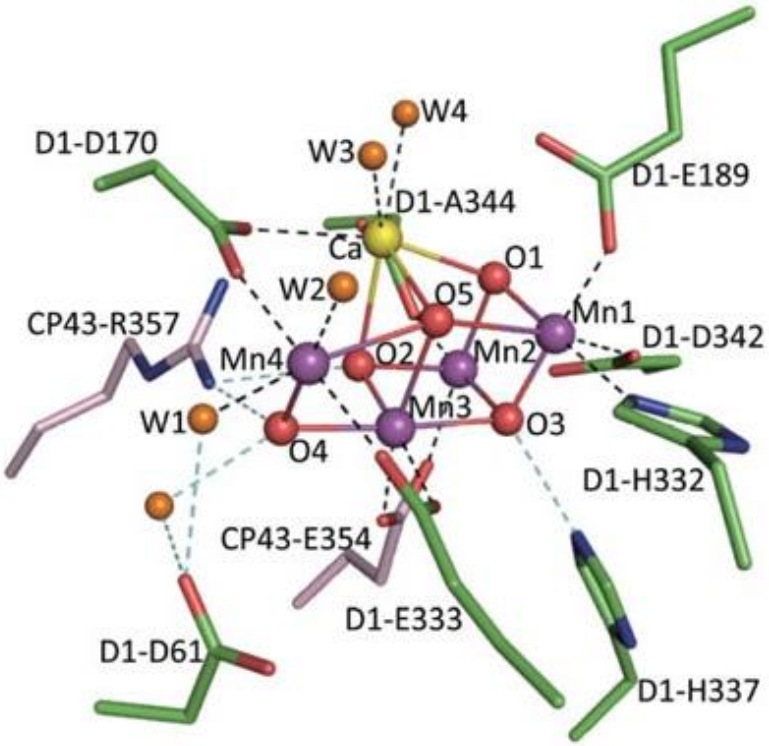

Figure 1. Stereo view of the Mn_4CaO_5 cluster and its ligand environment. The core is supported by six carboxylate ligands (D1-D170, D1-E189, D1-E333, D1-D342, D1-A344, and CP43-EE354), one imidazole ligand (D1-H332) and four water ligands (W1-W4). Reprinted with permission from reference 13. Copyright 2011, Springer Nature.

The water oxidation process in photosystem II is known as the Kok cycle which contains five "S-state" intermediates (from S_0 to S_4) in which S_0 is the most reduced state and S_4 is the most oxidized.[12] The absorption of a photon triggers the transfer of an electron and a proton in each stage which is also called a proton-coupled electron transfer (PCET) step.[15] PCET prevents an overall buildup of charges which lowers the redox potentials and allows the intermediates to reach high oxidation states.[12,15] From S_0 to S_4, the valences of four manganese ions keep increasing (S_0:

$Mn^{III}_3Mn^{IV}$, S_1: $Mn^{III}_2Mn^{IV}_2$, S_2: $Mn^{III}Mn^{IV}_3$, S_3: Mn^{IV}_4, and S_4: $Mn^{V}Mn^{IV}_3$ or Mn^{IV}_4) (the oxidation states of S_3 and S_4 is still under debate).[12] The O-O bond formation happens at S_4, and S_0 is regenerated after that.[12] There are several mechanisms that have been proposed for O-O bond formation during the Kok cycle (**Figure 2**). The first mechanism suggested that $Mn_{(V)}$=O of S_4 intermediate undergoes a nucleophilic attack by a water molecule bound with a Ca^{2+} ion.[11,12] The second mechanism is the intramolecular O-O bond formation between two $Mn_{(IV)}$-O radicals, also known as direct coupling mechanism in which two oxygen atoms from the same metal-oxo species are bound together.[12]

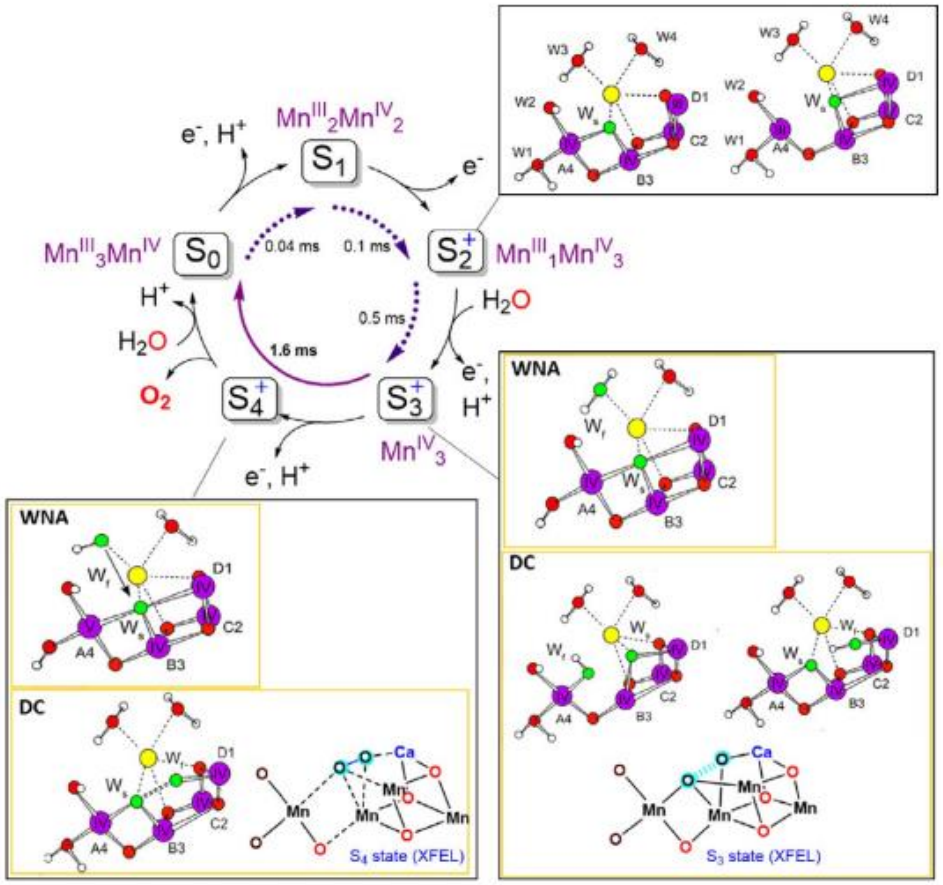

Figure 2. Kok cycle and possible "S-state" intermediates' structures. Different O-O bond formation pathways were proposed including WNA, water nucleophilic attack and DC, direct coupling. Reprinted with permission from reference 12. Copyright 2019, Elsevier.

Although the understanding about OEC is not complete, it still provides some guidelines for constructing efficient artificial WOCs. During the Kok cycle, the Mn_4CaO_5 cluster of the catalyst is further oxidized after each step to promote O-O bonding before returning to its original oxidation state. Therefore, it appears that a WOC should contain one or more transition metals due to its wide range of oxidation states. Moreover, research has shown that the electron-rich ligands: carboxylate and imidazole, assist in stabilizing the high valent states of the cluster.[16, 17] On account of these reasons, transition metal complexes are desirable candidates to be investigated as artificial WOCs.

2.4. Iron Complexes - A Key to Cheap and Highly Efficient Artificial Water Oxidation Catalysts

Inspired by nature, many transition metal complexes have been developed as WOCs. Transition metal complexes based on ruthenium and iridium have been developed as WOCs and have good performance.[18] For example, Ru-bda (bda^{2-} =[2,2'-bipyridine]-6,6'-dicarboxylate) complexes have a catalytic TON of over 100,000 and a TOF of $1000s^{-1}$.[19-22] However, these metals are less abundant in the earth's crust, so their cost is expensive and thus not suitable for mass production[23,24]. For this reason, many WOCs based on earth-abundant metals such as iron, cobalt, manganese, nickel, and copper have been synthesized and developed recently. Among these earth-abundance metals, iron is the most abundant transition metal in the earth's crust.[24] It is a redox-active metal whose oxidation states range from -1 to +6,[24] it is less toxic,[23] and it is also much cheaper than other transition metals.[23]

Iron complexes have recently been gaining attention for their ability to catalyze the water oxidation reaction. The first series of iron-based complexes were reported in 2010 in the research of Bernhard, and Collins, et al. to be able to stimulate water oxidation but with small TOF and

TON values (highest value of TOF and TON in the study are 1.3 s^{-1} and 16, respectively).[25] Since then, many other iron complexes have been developed as WOCs and their catalytic performance has improved significantly. In 2011, Fillol, and Costas, et al. reported that mono iron complexes bearing neutral tetradentate nitrogen ligands that leave two cis labile sites can efficiently catalyze water oxidation with faster rates and can last up to a few hours.[8] Their TON values ranged from 200 to over 1000, and the highest TOF was more than 800 s^{-1}.[8] In 2019, Fillol, and Costas, et al. introduced a robust monoiron complex that can yield a TON of more than 3400 and a TOF of more than 1400 s^{-1}.[26] Up to now, the majority of reported iron complexes are mononuclear iron complexes,[24] meanwhile, only a few dinuclear and polynuclear iron complexes have been developed. Ma et al. examined the catalytic activity of a dinuclear iron complex, $[(TPA)_2Fe_2(\mu\text{-}O)(\mu\text{-}OAc)]^{3+}$, for water oxidation and the highest TON of 2380 was obtained under the optimum conditions.[27] Akermark et al. successfully synthesized a nonanuclear iron complex which was capable of catalyzing water oxidation with a TON of 27.[28] In 2016, Masaoka et al. synthesized a pentanuclear iron complex which exhibited an excellent catalytic performance in water oxidation with a TON of about 10^6-10^7 for 120 minutes, and a TOF value of about 140-1400 s^{-1}, but it required a high overpotential of more than 0.5V.[29]

2.5. Factor Affecting the Catalytic Performance of Iron Complexes in Water Oxidation

Although many iron complexes have been synthesized and showed promising results in catalyzing the oxidation of water, they still have some limitations in practical applications such as low efficiency or the requirement of a high overpotential - a required voltage to drive a redox reaction.[24,29] Many efforts have been made to investigate what affects the catalytic performance of iron complexes as WOCs so that more highly efficient WOCs will be developed, and their ability can be optimized. The first factor that affects the catalytic performance of iron complexes in water

oxidation is the nature of the complexes themselves. Iron complexes are formed by iron ions (the electron acceptors) and one or more ligands containing electron-donor atoms.[30] Therefore, the properties of a metal complex rely heavily on the nature of metal ions and ligands. The choices of oxidants and reaction conditions are also significant to enhance the catalysts' performance.

Several research papers have shown that the number of iron ions in one complex can influence its performance. Most of the studies supported an idea that when the complex contains more iron ions, its catalytic ability increases. For example, Najafpour et al. successfully synthesized a dinuclear Fe complex using tpa (tpa: tris(2-pyridylmethyl)amine) ligand whose turnover frequency was 6 times higher than that reported for the mono-iron complex made from the same ligand.[31] The research of Ma et al. and Thummel et al. are another cases in which the activity of the diiron complexes were more active than their mononuclear counterparts.[27,32] It is believed that a synergistic effect between two metals can decrease the energy barrier and activate some chemical transformations which mononuclear complexes cannot access.[33] Dinuclear iron complexes typically adopt an dinuclear cooperative mechanism in which two M-O units interact to form the O-O bond.[33] Meanwhile, water oxidation catalyzed by mononuclear iron complexes is likely to undergo the water nucleophilic attack (WNA) mechanism in which a water or hydroxide entity attacks a high valent metal oxo-species (**Figure 3**).[12,33,34] The dinuclear cooperative catalysis (I2M mechanism and O-insertion pathway) requires lower energy than the nucleophilic attack mechanism because it promotes the reaction via the intramolecular pathway and it does not require the formation of high valent metal-oxo intermediate (**Figure 3**).[33] Another case that supported the idea is the research of Akermark et al. in which the nonanuclear iron complex had slightly better results than the dinuclear complex even though they were based on the same ligand.[35] On the other hand, in the research of Sakai et al. with two iron complexes: iron tris(2-methylpyridyl)amine

(TPA) and iron 1-(bis(2-methylpyridyl)amino)-2-methyl-2-propanoate (BPyA), the mononuclear forms of these two iron complexes showed higher catalytic activity than the dinuclear forms in the water oxidation driven with sodium periodate.[36] The mechanism indicated in this research was a nucleophilic attack by water during O-O bond formation.[36] This research showed that metal complexes with more iron ions are not always more active than those with few iron ions. Other factors need to be considered so that a highly efficient iron complex can be designed, in particular, factors that can contribute to the intramolecular interactions in the catalytic mechanism.

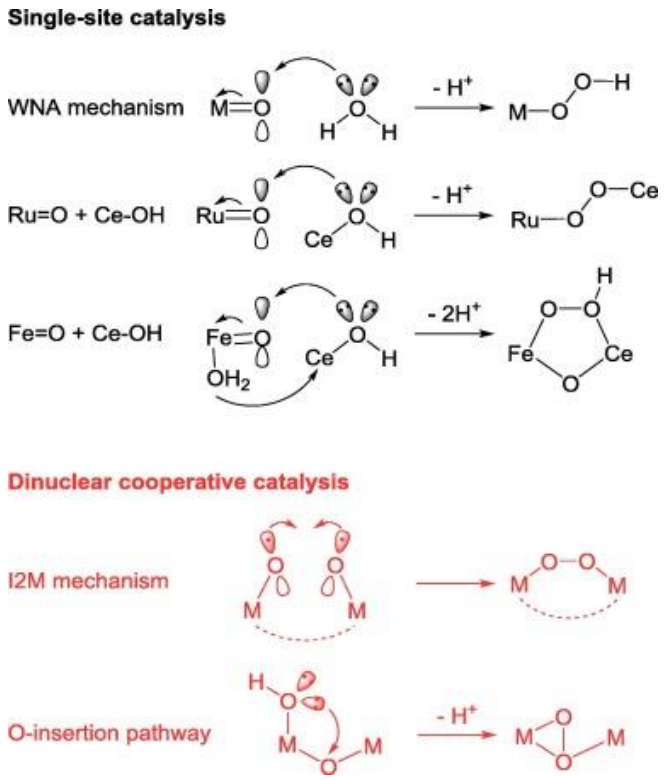

Figure 3. Mechanisms for O-O bond formation during the water oxidation by mononuclear (top, black) and dinuclear (bottom, red) metal complexes. Reprinted with permission from reference 33. Copyright 2018, Elsevier.

Ligand structure can determine how iron complexes will be formed and critically influence their catalytic performance as WOCs. It affects the number of iron atoms that can be coordinated. Thummel et al. used two ligands with similar structures to construct iron complexes: ppq (2-(pyrid-

2′-yl)-8-(1″,10″-phenanthrolin-2″-yl)-quinoline) and dpa (bis-phenanthroline amine) (**Figure 4**).[32] Both ligands had the quaterpyridine-like backbone and a square planar arrangement, but the ppq ligand formed a dinuclear iron complex while the dpa ligand formed a mononuclear iron complex.[32] It is suggested that N-isopentyl group of dpa caused steric hindrance which inhibited the formation of the diiron complex.[32] Moreover, if a small variation in structure exists between two iron complexes, their efficiency in catalyzing water oxidation can have a huge difference. In the research of Collins et al., five iron (III)-tetraamido macrocylic ligand complexes (Fe^{III}-TAMLs) with varying the number of electron-withdrawing substituents to the ligand (etc. Cl^-, F^-, NO_2^-), were synthesized and utilized to perform water oxidation in excess ceric ammonium nitrate (CAN) at pH 0.7.[25] The rates of oxygen evolution were higher in the reaction with the iron complexes containing stronger electron-withdrawing groups or higher number of these groups (**Figure 5**).[25] The substituents on the ligand can also impact the electronic properties of iron complexes. Leitner et al. (2019) examined several complexes constructed on H-dpaq ligands with different substituents at the 5-position of the quinoline ring (dpaq = 2-[bis(pyridine-2-ylmethyl)]amino-N-quinolin-8-yl-acetamide) (**Figure 6**).[37] When the proton was replaced by electron-withdrawing groups ($-NO_2^-$ and $-CF_3^-$), both the catalytic current and the overpotential of the complexes increased; meanwhile, with the presence of electron-donating groups (-OMe), the potential of iron complex oxidation became negative and no catalytic current was observed which meant the water oxidation could not happen.[37] Furthermore, the incorporation of a pyrenyl group (four fused benzene rings) into one of the pyridine groups of the H-dpaq ligands could raise the peak current and lower the overpotential; showing greater catalytic ability.[37]

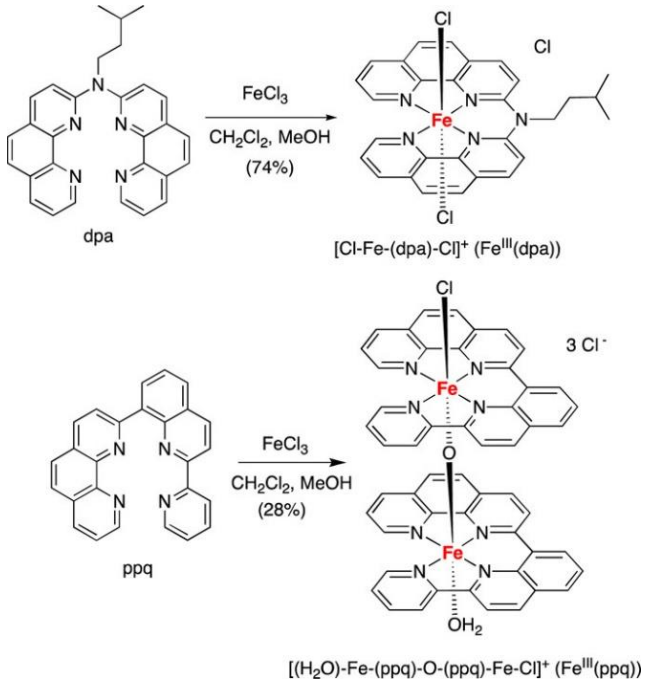

Figure 4. Synthetic scheme of Fe^{III}(dpa) complex (top) and of Fe^{III}(ppq) complex (bottom). Reprinted with permission from reference 32. Copyright 2015 American Chemical Society.

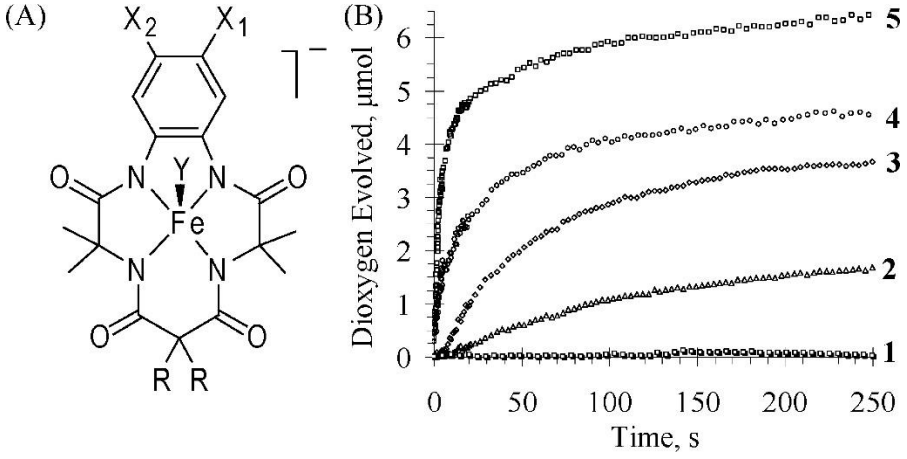

Figure 5. The effect of different substituents on TAML on the oxygen evolution rate. (A) Fe^{III}-TAMLs synthesized in the research of Collins et al. (2010): **1**, $X_1 = X_2 = H$, $R = CH_3$; ***2***, $X_1 = X_2 = H$, $R = (CH_2)_2$; **3**, $X_1 = X_2 = H$, R = F; **4**, $X_1 = NO_2$, $X_2 = H$, R = F; **5**, $X_1 = X_2 = Cl$, R = F. (B) Plots of O_2 evolution with time of complexes **1-5**. Reprinted with permission from reference 25. Copyright 2010, American Chemical Society.

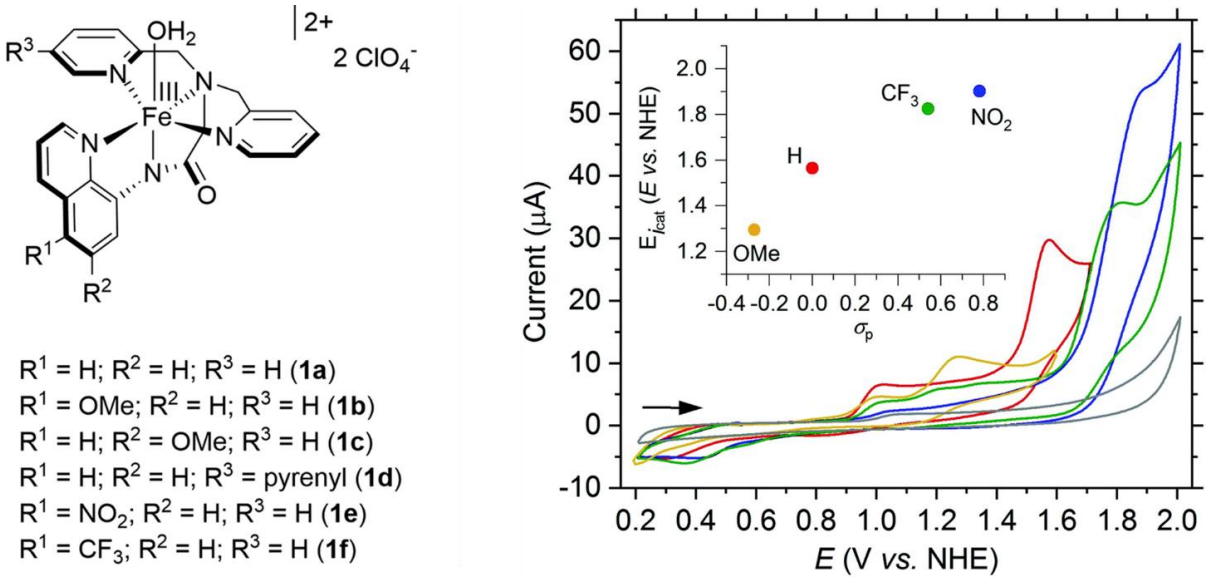

Figure 6. The effects of different substituents on the dpaq ligands on electronic properties of the corresponding iron complexes. Iron dpaq complexes in the study (left) and CV of Fe(dpaq) complexes in a mixture of propylene carbonate and water at a scan rate of 75 mV s^{-1} with R = H (1a, red), OMe (1b, orange), NO_2 (1e, blue) or CF_3 (1f, green) and in the absence of a complex (grey). Inset: Plot of E_{icat} vs. the Hammett substitution constant σ_p of R. Reprinted with permission from reference 37. Copyright 2019, CC BY 3.0.

In addition to a WOC catalyst, an oxidant is necessary to drive water oxidation. The choice of oxidants is significant in the optimization of a catalyst's performance. Water oxidation can be driven by light, chemical oxidants (e.g. cerium (IV) ammonium nitrate (CAN), hypochlorite, potassium peroxymonosulfate (Oxone), periodate), or electrochemical cells.[12] Due to the ease of setting up the experiment with chemical oxidants, they are used widely to carry out water oxidation. The chemical oxidant that has high reduction potential can assist in catalyzing the water oxidation reaction more efficiently, but it also can drive other unfavorable side reactions or lead to the degradation of catalyst like CAN or sodium peroxydisulfate.[38] Milder oxidants like the ruthenium(III) tris(bipyridine) ($[Ru^{III}(bpy)_3]^{3+}$) cation is less likely to cause side reactions but it cannot work for many water-oxidation catalysts.[38] Also, because several WOCs form unstable complexes when they undergo one-electron oxidation, a two-electron oxidant like Oxone or sodium periodate can be applied in those cases.[38] Some oxidants require a certain iron complex

structure to trigger a water oxidation reaction. Fillol et al. investigated the activity of two topological isomers of $Fe^{II}(CF_3SO_3)_2$ (**1-α** and **1-β**) in chemically driven water oxidation (**Figure 7**).[39] Although the reactions were carried out under the same condition, **1-α** was highly active and yield a significant amount of O_2; meanwhile, **1-β** was a very poor catalyst. The reaction was monitored by UV-Vis, manometry, and cold-spray ionization high-resolution mass spectroscopy (CSI-HRMS). An intermediate containing $O=Fe^{IV}$-O-Ce^{IV} was captured during the water oxidation reaction catalyzed by **1-α**.[39] It was concluded that the key reaction intermediate in this water oxidation had $O=Fe^{IV}$-O-Ce^{IV} core, which suggested that iron-based catalysts require a framework that allows the formation of iron-oxo-cerium.[39] The possible reason that the complex **1-β** could not generate this intermediate might come from its steric or electronic nature.[39]

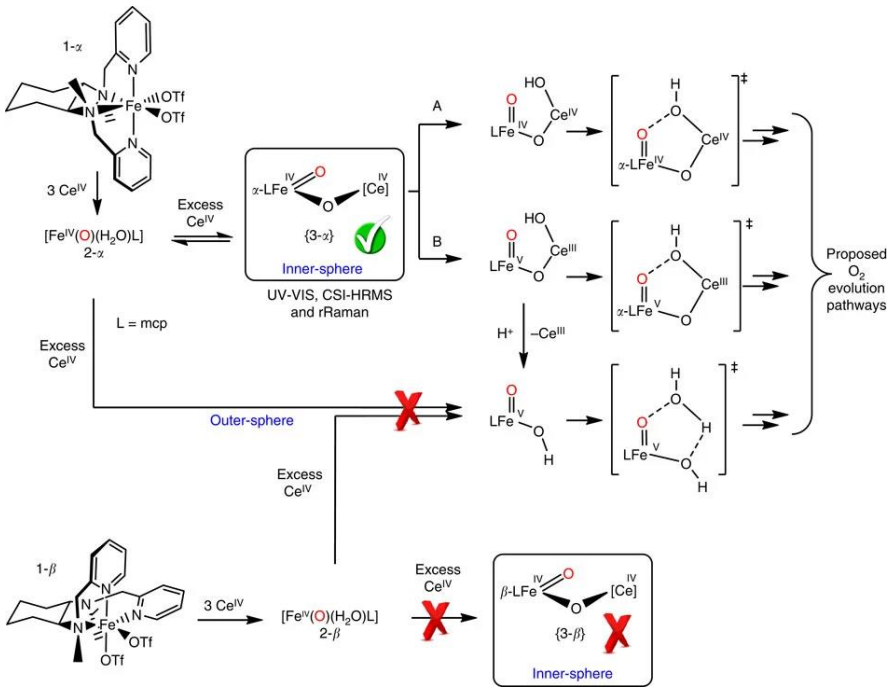

Figure 7. Reactivity difference between two topological isomer 1-α and 1-β in the research of Fillol et al. (2015). Reprinted with permission from reference 39. Copyright 2015, Springer Nature.

Reaction conditions like pH or temperature have effects on both iron complexes and oxidants. Iron complexes behave differently in acidic and basic environments (**Figure 8**). Iron

complexes can catalyze the water reaction in the presence of CAN or IO_4^- at low pH values,[8,25, 40] but ligand dissociation processes which released iron ions and free ligand occurred at the same time. However, under neutral and basic conditions, iron complexes decomposed to iron oxide or iron hydroxide nanoparticles.[40,41]

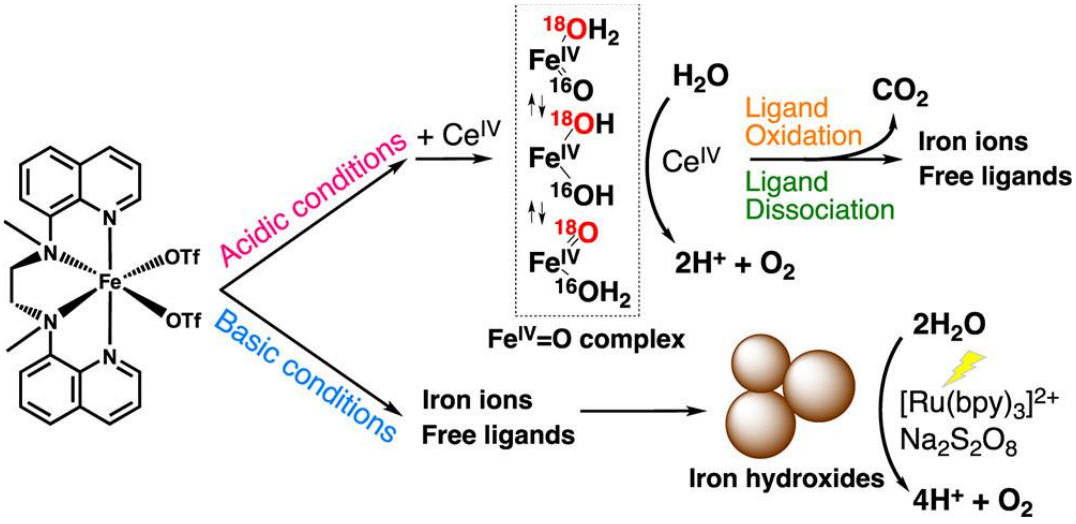

Figure 8. Iron Catalysts derived from a nonheme iron complex in catalytic water oxidation at different pHs. Reprinted with permission from reference 40. Copyright 2013, American Chemical Society.

Najafpour et al. also reconfirmed this statement by examining a pentanuclear iron complex under neutral and basic condition. As expected, a trace of iron (III) oxide was found on the surface of electrode.[42] The stability of oxidants also relied on the pH of the reaction environment. For example, CAN is only stable under highly acidic condition and the typical CAN solution has a pH of approximately 0.9.[38] $[Ru^{III}(bpy)_3]^{3+}$]) is stable in acidic solution with pH values < ~4.[38] Meanwhile, Oxone can be stable in solutions with pH values close to neutral (up to pH of 5.5).[38] Sodium periodate is stable in solutions having pH values from 2 to 7.5.[38] In addition to pH, temperature was also reported to be able to affect the catalytic activity of iron complexes towards water oxidation.[31] The results showed the nature log of the rate of oxygen evolution and inverse temperature (1/T) are directly proportional in a linear fashion.[31] This research showed that

temperature was one of the factors that need to be considered for the efficiency of the water oxidation reaction. However, it is often unclear how temperature directly affects the catalyst itself. Further investigations are required to understand this phenomenon.

3. Conclusions

Hydrogen fuels are abundant, environmental-friendly, and rich in energy so that they can be seen as a great alternative for fossil fuels. However, there are several challenges to solve if humans want to make the most of this resource such as the strict requirements in storage and transportation, the danger caused by its extreme flammability, and the high cost of its production from water oxidation. Inspired by the oxygen-evolving complex (OEC) in photosystem II of plants, a powerful WOC, many transition metal complexes have been developed to catalyze the water oxidation reaction. Among different metal complexes, iron complexes have attracted huge attention lately due to its abundance, wide range of oxidation states, low toxicity, and low cost. Previous research has provided significant insights into what influences the catalytic performance of iron complexes in water oxidation. Three main factors that determine the efficiency of the catalyst are its structure, the oxidants, and the reaction conditions. The structures of iron complexes are varied by the number of iron ions coordinated, and the structure of ligands. Several studies have showed that in many cases, when the number of iron ions increased, the activity of the catalyst also raised due to the synergistic effect between two or more metal ions and the ease in adopting intramolecular mechanism. The way that ligand affects the complex is that it can influence which form of complexes can be synthesized: monoiron, diiron, triiron, or polyiron species. Moreover, different groups attached to the ligand can have a great effect on the rate of the water oxidation, as well as the electronic properties of the iron complexes. In addition to the structure of the catalyst itself, the oxidant used in the water oxidation reaction also affects the iron complexes'

performance. Strong oxidants can drive the reaction faster, but they can degrade the iron complexes. On the contrary, mild oxidants are good for the stability of the complexes but weaker in driving the reaction forward. Therefore, to use the strong oxidants, a tight-binding and chemically robust ligand is required. Furthermore, some oxidants only allow certain structures of iron complexes to run the reaction because they are involved in the intermediate stage of the catalysts. Lastly, reaction conditions such as pH and temperature have some influences on the efficiency of the water oxidation reaction. Some researchers have showed that at low pH, oxidants like CAN and the iron complexes are stabilized but at high pH, decomposition could happen. Temperature is related to the rate of the reaction but how it affects the iron complexes was not clear.

The chapter reported the progress in the development of iron complexes and factors influencing its efficiency and effectivity as WOCs. There was an improvement in performance of iron complexes throughout the years thanks to the modification in the ligands' structure and the number of iron incorporated, as well as, the selection of oxidants and reaction conditions. Meanwhile monoiron complexes for water oxidation reactions have been studied extensively. However, not many studies have been reported for diiron complexes, there are several reports which indicate that diiron complexes are likely to have better catalytic performance than monoiron complexes.[27,31,32,35] Therefore, this study aims to develop a fast and efficient synthetic route for constructing a series rationally designed ligands that would form various stable diiron complexes as potential water oxidation catalysts.

CHAPTER II

DESIGN AND SYNTHESIS OF A DINUCLEATING LIGAND TO CONSTRUCT DIIRON COMPLEXES AS WATER OXIDATION CATALYSTS FOR ENERGY APPLICATIONS

1. Introduction

Chapter II reported a two-step synthetic route for a novel dinucleating ligand that is capable of forming diiron complexes. The ligand structure was validated by several types of nuclear magnetic resonance spectroscopy (NMR) including ^{1}H NMR, ^{1}H-^{1}H Double-Quantum Filtered Correlation Spectroscopy (DQF-COSY), ^{13}C NMR, and ^{1}H-^{13}C Heteronuclear Single Quantum Coherence Spectroscopy (HSQC) and Time-of-flight- Electrospray Ionization - Mass Spectrometry (TOF-ESI-MS). The formation of diiron complexes were examined by ^{1}H NMR and TOF-ESI-MS. The selectivity of this ligand structure toward different types of iron salts in forming diiron complexes were revealed. From the development of the new dinucleating ligand, a new family of diiron complexes could be constructed and subjected to catalytic tests for water oxidation reaction in later research which will contribute significantly to the progress of achieving an affordable and effective WOC for hydrogen production.

2. Materials and Methods

2.1. General Methodology

Starting materials including dimethyl isophthalate, ethylene diamine, and 2-(chloromethyl) pyridine hydrochloride were bought from Acros Organics. Iron (II) chloride was purchased from Sigma Aldrich. Iron (II) triflate salt was synthesized according to procedures reported in previous literature.[43] Solvents used in the experiments were reagent grade unless otherwise noted. NMR spectra including ^{1}H NMR, DQF-COSY, ^{13}C NMR, and HSQC were recorded on a Bruker Avance 300 MHz spectrophotometer using methanol-D_4 solvent purchased

from Cambridge Isotope Laboratories, Inc. Mass spectral analyses were run by Xevo G2-XS QTof Quadrupole Time-of-Flight Mass Spectrometry using HRMS grade methanol containing 1% formic acid as a solvent for ligand sample and HRMS grade acetonitrile as a solvent for the iron complexes.

2.2. Design and Synthesis of the Ligand

Before being able to obtain a stable diiron complex, a strong ligand backbone that can stabilize two metal centers is required. The structure of the ligand consists of three major components: the basal platform, the linkers, and the metal-binding units (**Figure 9 & 10**).

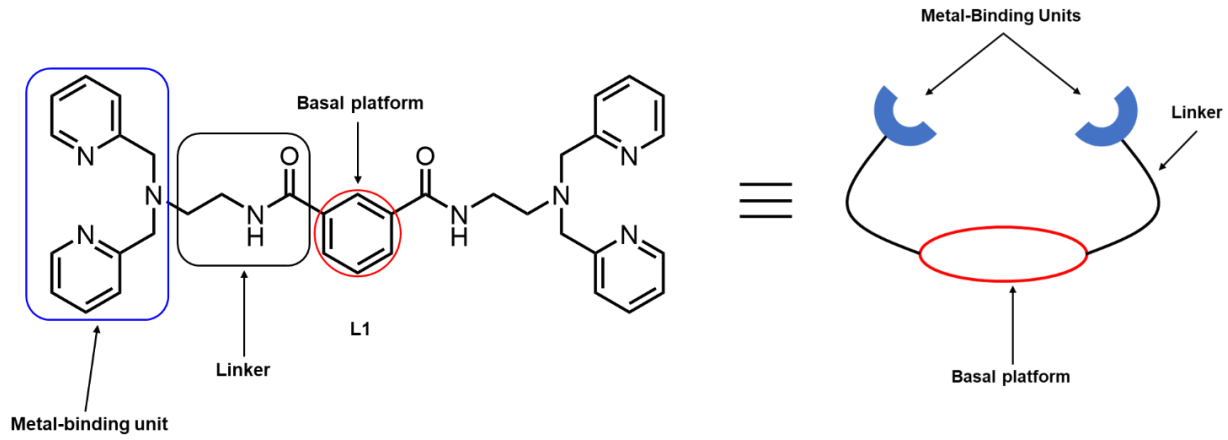

Figure 9. Molecular structure of the ligand, L1, in this study (left) and a graphical representation of the ligand (right). The basal platform is displayed in red color; linkers are black, and metal-binding units are blue.

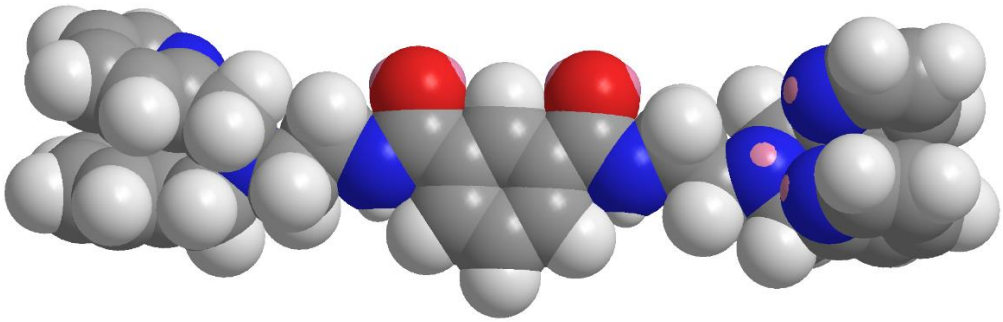

Figure 10. MM2 mimimized 3D space-filling model of the ligand L1 (white balls: hydrogen atoms, gray balls: carbon atoms, blue balls: nitrogen atoms, red balls: oxygen atoms, and pink balls: lone pairs of electrons).

The phenyl moiety has been chosen as the basal platform because it is a conjugated six-membered ring that is chemically stable, and it provides two sites for linker attachment within a short distance. Similarly, other research groups have successfully incorporated linkers and metal binding units for constructing iron-sulfur complexes[44-46] and manganese-oxygen clusters.[47] The linkers consist of medium-sized hydrocarbon chains containing from 3 to 5 carbon atoms that will be connected to the basal platform via amide bonds. The medium-sized linkers are believed to be flexible and close enough to allow for the interaction between the two metals captured by the metal-binding units. The last step of the ligand synthesis is the incorporation of the metal-binding units, which are comprised of N and O donor atom containing functional groups such as polypyridines, amines, and carboxylates. The reason that the metal-binding units should have several N or O atoms is that N and O are electron rich, and thus act as electron donors in the formation of dative covalent bonds with the iron centers and stabilizers when the oxidation state of irons increases. As some studies have shown, one iron often forms six covalent bonds with ligands and adopts an octahedral or pseudo-octahedral geometry.[48,49] The multi-binding unit should have three or four donor atoms to make sure that each iron in the diiron complexes will have at least one labile site at which a metal-ligand bond can be easily broken so that the substrate can come in and promote the formation of O-O bonds. **Scheme 1** illustrates the two-step synthetic route to the target ligand, in which the first step is the formation of the bond between the basal platform and the linkers. The second step is the attachment of metal-binding units. The ligand structure was characterized by NMR, and TOF-ESI-MS.

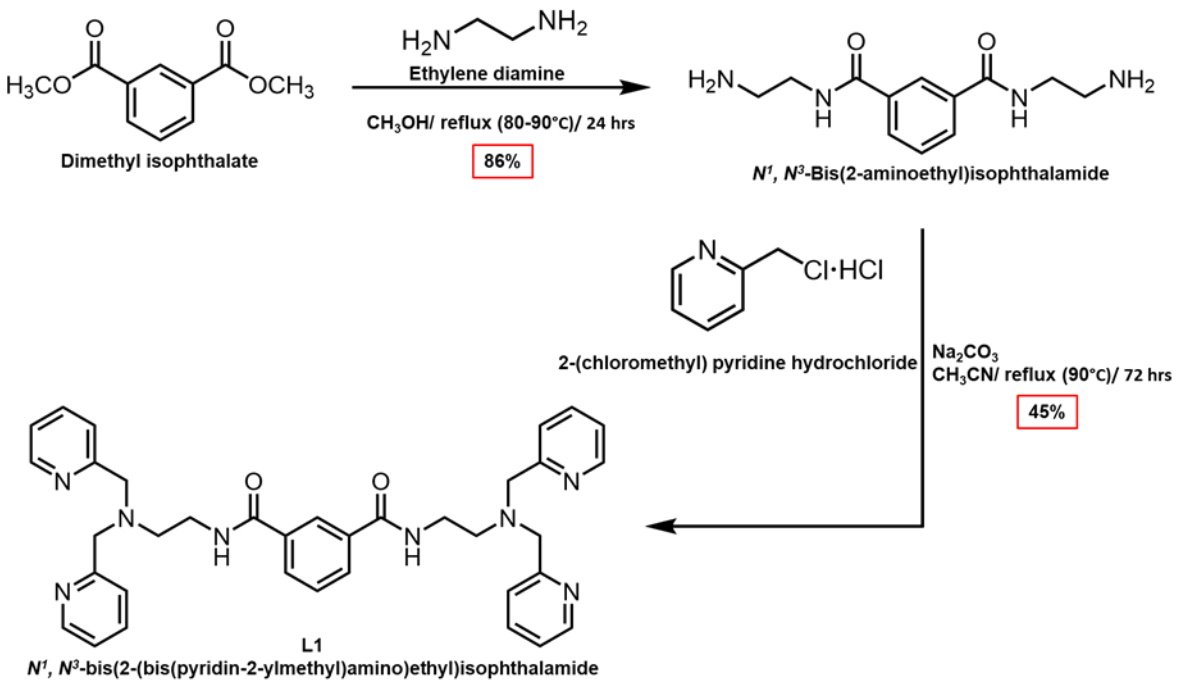

Scheme 1. Synthetic route for the L1 ligand.

2.2.1. Synthesis of *N*^{1}, *N*^{3}-Bis(2-aminoethyl)isophthalamide ($C_{12}H_{18}N_4O_2$, Mw = 250.30 g/mol): In the first step, dimethyl isophthalate (0.486 g, 2.5 mmol) was reacted with ethylenediamine (6.8 mL, 0.1 mol) in methanol under reflux at 80-90°C for 24 hours. Excess ethylene diamine and solvent were evaporated under reduced pressure after mixing the reaction mixture with toluene (50 mL, 3 times). Ethylene diamine has a high boiling point (~116°C), so it is hard to remove on a rotary evaporator unless high temperature water bath is used. However, by adding toluene into the ethylene-diamine-containing-solution, an azeotropic mixture is formed and can be removed at low temperature. After the excess solvent was removed, the product was further dried by putting it under high vacuum for one day. A light yellow gel was obtained as our product with 86% yield (0.538 g, 2.15 mmol). ^{1}H NMR (MeOD, 300 MHz, 25°C): δ = 2.86 (t, J = 6.3 Hz, 4H), 3.47 (t, J = 6.3 Hz, 4H), 7.57 (t, J = 7.8 Hz, 1H), 7.99 (dd, J = 7.8, 1.8 Hz, 2H), 8.32 (t, J = 1.6 Hz, 1H); ^{13}C NMR (MeOD, 100 MHz, 25°C): δ = 42.09, 43.76, 127.47, 129.93, 131.33, 136.24, 169.75.

2.2.2. Synthesis of the ligand (L1) – N^1, N^3-bis(2-(bis(pyridin-2-ylmethyl)amino)ethyl)isophthalamide ($C_{36}H_{38}N_8O_2$, Mw = 614.75 g/mol): N,N'-Bis(2-aminoethyl)isophthalamide (0.538 g, 2.15 mmol) was then treated with 2-(chloromethyl) pyridine hydrochloride (1.76 g, 10.75 mmol) in acetonitrile (20 mL) and sodium carbonate (2.28 g, 21.5 mmol). More specifically, 2-(chloromethyl) pyridine hydrochloride was mixed with sodium carbonate for 10 minutes in 25 mL of anhydrous acetonitrile to afford 2-(chloromethyl) pyridine. N,N'-Bis(2-aminoethyl)isophthalamide was then dissolved in a small amount of methanol (2-3 mL) and added dropwise into the reaction mixture. The reaction was refluxed at 90°C for 3 days under an argon atmosphere. The color of the reaction mixture changed from bright orange to dark red. The reaction was cooled and Na_2CO_3 was filtered out and the dark red gel product was obtained after one day under high vacuum. The purity of the product was examined with thin layer chromatography using alumina plates and a solvent of 10% methanol (MeOH) and 90% ethyl acetate (EtOAc). It turned out that the crude product contained at least five different compounds (**Figure 11**). These compounds were separated using column chromatography. The stationary phase of the column was alumina gel and four different solvent systems were used as the mobile phase with an increasing order of polarity (1st: 100% EtOAc, 2nd: 5% MeOH + 95% EtOAc, 3rd: 10% MeOH + 90% EtOAC, 100% MeOH). Each of the samples from the column was characterized using ^{1}H-NMR to identify the ligand. The ligand was the fourth spot from the top of the TLC plate with Rf value about 0.6 (**Figure 11**). The column chromatography gave the product as a yellow-orange gel (0.594 g, yield 45%). ^{1}H NMR (MeOD, 300 MHz, 25°C): δ = 2.78 (t, J = 5.9 Hz, 4H), 3.57 (t, J = 5.9 Hz, 4H), 3.82 (s, 8H), 7.14 – 7.31 (m, 4H), 7.48 – 7.68 (m, 9H), 7.99 (dd, J = 7.8, 1.8 Hz, 2H), 8.30 (t, J = 1.6 Hz, 1H), 8.39 (ddd, J = 5.0, 1.8, 1.0 Hz, 4H); ^{13}C NMR (MeOD, 100 MHz, 25°C): δ = 38.98, 54.91, 60.98, 123.93, 125.23, 127.73, 129.95, 131.25, 136.38,

138.76, 149.63, 160.42, 169.14; TOF-MS: calculated m/z for $[L1+H]^+$: 615.3196, found 615.5187; calculated m/z for $[L1+2H]^{2+}$: 308.1637; found 308.2944.

Figure 11. TLC result of the crude product of the ligand. The spot of the pure ligand was the spot circled in red. Individual fractions collected from first trial of column chromatography were examined with NMR to confirm the ligand spot position.

2.3. Synthesis of the Iron-Ligand Complexes

After the ligand was obtained and characterized, it was reacted with different iron salts (iron(II) chloride and iron(II) triflate) to form diiron(II) complexes (**Scheme 2**). The metalation was performed inside a glove box filled with N_2 gas to prevent oxidation of the iron complexes by O_2. In case that oxygen is present, mixed-valent dinuclear iron complex might arise because the Fe_{II} center is easily oxidized to form Fe_{III}.

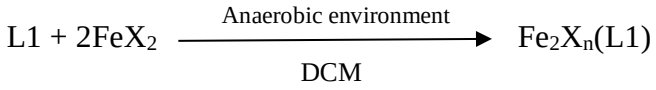

($X = Cl^-$ or $^-OSO_2CF_3$)

(n = number of anions coordinated with iron ions)

Scheme 2. A general synthetic scheme to construct diiron complexes

2.3.1. Synthesis of $Fe_2Cl_n(L1)$ complex: The ligand L1 (~0.15 g, 1 equiv.) was first dissolved in 5 mL of anhydrous dichloromethane (DCM). Two equivalents of iron (II) chloride ($FeCl_2$) were added, and the reaction was allowed to stir overnight. The mixture was then filtered, and a yellowish powder was obtained. Yield: 55%. TOF-MS: calculated m/z for $[Fe^{II}_2Cl_2(L1)]^{2+}$: 398.0597, found 398.1971; calculated m/z for $[Fe^{II}_2Cl_3(L1)]^+$: 831.0882, 833.1121 found 831.3140, 833.3115; calculated m/z for $[Fe^{II}Fe^{III}Cl_2(L1)]^+$: 796.1193, found 796.3277; and calculated m/z for $[Fe^{II}Fe^{III}Cl_4(L1)]^+$: 866.0571, 868.0698, found 866.2841, 868.2814.

2.3.2. Synthesis of $Fe_2(OTf)_n(L1)$ complex: One equivalent of the ligand L1 (~0.15 g) dissolved in 5 mL of anhydrous DCM was mixed with two equivalents of iron triflate salt $Fe^{II}(OTf)_2.2CH_3CN$ for 24 hrs. Unlike the synthesis of the $Fe_2{}^{II}Cl_4(L1)$ complex, in this reaction, no solid was formed. 5 mL of anhydrous ethyl ether was mixed into the solution for another 24 hrs. and a brownish gel was observed in the bottom of the vial. After the solution was poured out, the gel was allowed to stir in 3 mL of anhydrous ethyl ether for an additional 24 hrs. The mixture was filtered, and a brownish powder was afforded with a yield of 67%.

2.3.3. Recrystallization of the diiron complexes. After the diiron complexes were characterized by NMR and mass spectroscopy, they were then dissolved back in acetonitrile and placed in a chamber containing ethyl ether for recrystallization so that crystals suitable for X-ray crystallography analysis can be obtained. Unfortunately, no crystals were obtained for the complexes.

2.4. Characterization of Chemical Structures by NMR Techniques and TOF-ESI-MS

NMR spectroscopy is a powerful analytical method which can provides information about the chemical structures of organic compounds. This method also has high reproducibility, non-destructive characteristics, and a simple sample preparation. NMR spectroscopy principle relies on the influence of the external magnetic field (B_0) on nuclei (**Figure 12**).[50] Atoms with odd mass number such as ^{1}H and ^{13}C can create a magnetic field around them when spinning. They randomly oriented in space, and all have the same energy state. However, under effect of B_0, these nuclei are aligned in either the same or opposite direction with B_0, which leads to the arising of different energy states: lower energy states and higher energy states. NMR spectroscopy utilizes radiofrequency radiation (RF) which have long wavelengths, and thus low energy and frequency as its source of energy. When the external RF energy matches the energy difference (ΔE) between states, it is absorbed causing the nucleus to "spin-flip" moving from lower energy state to a higher energy state and come back. This absorption and emission RF energy can be detected by the NMR spectrometer, as a result, a NMR spectrum is generated. The difference in the absorption of radiofrequency provides critical information for structural elucidation. The frequency at which a nucleus absorbs is determined by its electronic environment. When a nucleus surrounds by higher number of electrons, it experiences less the external magnetic field, thus the energy it needs to absorb to "spin-flip" is smaller. The absorption of smaller energy will generate a signal in the upfield of the spectrum. By contrast, the signal will show in the down-field of the spectrum if the nucleus is shielded by a small number of electrons. The information of molecular structures can also be derived from the magnetic interaction of NMR-active nuclei that are close to each other as their interaction results in the spin-spin coupling (the splitting of NMR signals).

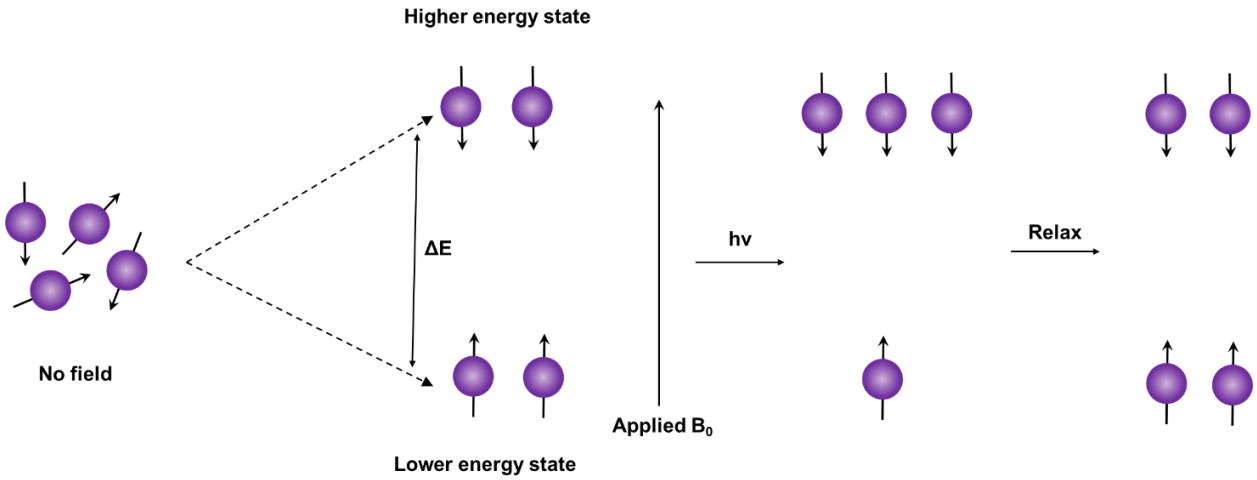

Figure 12. Diagram depicts the basic principle of NMR spectroscopy.

The common NMR techniques such as ^{1}H NMR and ^{13}C NMR which provide one dimension information with plots of amplitude against one frequency dimension typically show limitation when resolving signals of large and complex molecules.[51] The two-dimensional NMR spectroscopy (2D NMR) is capable of overcoming this limitation. Two-dimensional NMR spectroscopy (2D NMR)[51,52] utilizes a sequence of RF pulse with two independent variable time intervals (the acquisition time t_2 and the incremental delay time t_1) to generate plots of amplitude against two frequency axes. It differs from 1D NMR by having two extra stages: evolution and mixing in between acquisition stage and excitation stage (**Figure 13**). One scan of 2D NMR spectrum contains three steps. In the first step (preparation step), the sample is excited by one or more RF pulses. Next, in the evolution stage, nuclei become magnetic freely. Then, the sample is further excited and the magnetization of one nucleus transferred to another nucleus, or the magnetization is pushed around in a controlled fashion (mixing period). In the acquisition stage, the NMR signals is acquired by recording the frequency of both nuclei as a function of t_2. With extra stages in one scan of analysis, 2D NMR makes it possible to resolve overlapping peaks in 1D NMR spectra, as well as evaluate connectivity between two atoms of the same element

(homonuclear) or two different atoms (heteronuclear). COSY can be employed to study the homonuclear correlation of protons coupled to each other while HSQC is used to study the correlation between proton and carbon connected via one single bond. Moreover, through-space correlation can be examined with nuclear Overhauser effect spectroscopy (NOESY) and rotating-frame nuclear Overhauser effect spectroscopy (ROESY). The disadvantages of the 2D NMR technique are that it requires longer experiment time and larger computer data storage.[53]

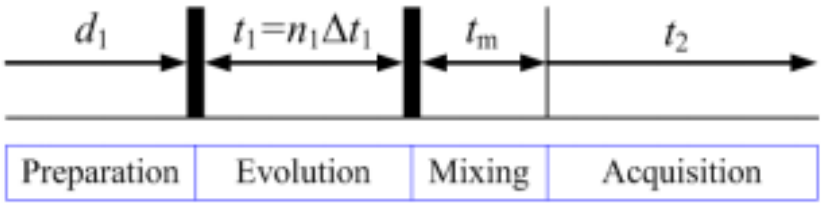

Figure 13. General scheme for 2D NMR spectra. Reprinted with permission from reference 52. Copyright 2011, CC BY.

Mass spectroscopy (MS)[54-56] is an analytical technique measuring mass-to-charge (m/z) ratios of charges species from which important structural information of organic/inorganic compounds could be extracted. Every mass spectrophotometer is built with three main compartments: an ionization source, a mass analyzer, and a detector (**Figure 14**). First, an analyte sample is subjected to go through an ionization process in which it is transformed into gas-phase ionized species. These ionized species then are sorted out by the mass analyzed based on their m/z values before reaching to the detector. The detector provides the data of m/z values with their relative abundances so that a mass spectrum can be created from a computer software. In this research, TOF-ESI-MS was utilized for the characterization of the ligand and the diiron complexes for several reasons. The electron spray ionization (ESI) is a soft ionization technique in which the analyte solution is turned into charged droplets after going through a small capillary with a high

voltage applied and then these droplets are further evaporated when passing a heating capillary to form ions. The ESI allowed the organic compounds or inorganic complexes to be ionized but remained intact. With the ESI, it is easier to determine the molecular weight of the compounds as little to no fragmentation is created from this ionization technique. Based on the fact that the charged species have different velocity due to their various m/z values, a time-of-flight analyzer measures the time that each ion needed to reach the detector to generate m/z ratios data.

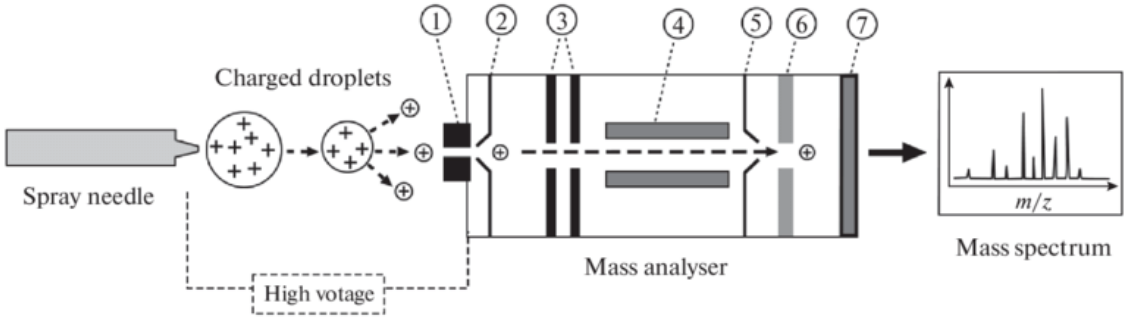

Figure 14. Schematic representation of ESI MS. 1-heated gate, 2-skimmer, 3-lenses, 4-focusing chamber, 5-gating lens, 6-ion trap, 7-detector. Reprinted with permission from reference 56. Copyright 2019, Springer Nature.

3. Results and Discussion

3.1. Synthesis and Characterization of the Ligand (L1)

The synthesis of ligand, L1, was achieved with a total yield of 38.7%. The first step of the synthesis had a high yield of 86% and was straight-forward, facile, and easy to repeat. However, the second step of the synthesis suffered from a low yield of 45% which brought down the total yield. Based on the TLC analysis, the reaction was either not complete or it generated too many side products. Furthermore, a portion of the target compound might have been lost to the column. Characterization of the isolated ligand from NMR and MS spectra supported that the collected sample was the target compound.

3.1.1. Characterization of N^1, N^3-Bis(2-aminoethyl)isophthalamide

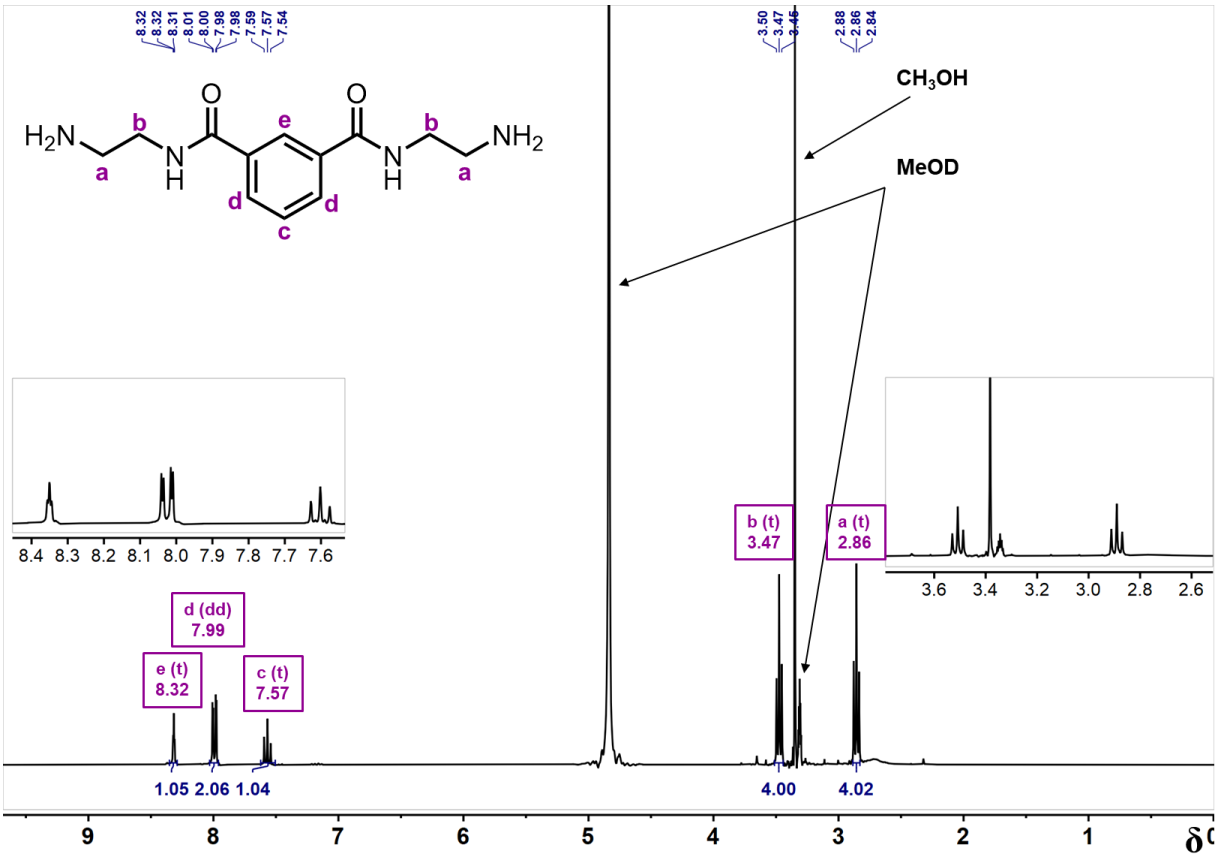

Figure 15. ^{1}H-NMR of N^1, N^3-Bis(2-aminoethyl)isophthalamide. The sample was prepared in MeOD solvent at 25°C.

Different NMR techniques including ^{1}H NMR, ^{13}C NMR, ^{1}H-^{1}H DQF-COSY, and ^{1}H-^{13}C HSQC were able to confirm the structure of N^1, N^3-Bis(2-aminoethyl)isophthalamide. **Figure 15** depicts the ^{1}H-NMR spectra of N^1, N^3-Bis(2-aminoethyl)isophthalamide. The spectrum showed five different groups of signals corresponding to five different types of protons as expected for the sample. If ethylene diamine molecules were attached only at one side of dimethyl isophthalate, there would have been seven distinct peaks instead. Two triplet signals in the regions from 2.5 – 3.5 ppm corresponded to two methylene (-CH_2-) groups situated next to one another. Three signals situated between 7.5 – 8.5 ppm corresponded to aromatic protons. Based on signal integration,

chemical shift values, and peak multiplicity in the NMR spectrum, it was possible to assign which group of protons was represented by which signal as indicated in **Figure 15**. The chemical shift of the signal for H_b is more downfield than the signal for H_a due to the deshielding effect caused by the adjacent amide group. The integral values of three signal peaks of the aromatic protons at 7.60, 8.03, and 8.35 ppm were 1:2:1 respectively. This indicated that the peak at 8.03 ppm belongs to H_d. Among the three different proton chemical environments in the aromatic ring, H_e was the most de-shielded proton due to its proximity to the C=O bond. By contrast, H_c was the most shielded. The signal of H_c showed an obvious triplet, but the triplet of H_e looked more like a singlet due to longer range (^{4}J) proton-proton coupling to two H_d. ^{1}H-NMR spectrum analysis further verified the symmetric structure of the compound, the presence of an aromatic ring, and two adjacent methylene groups. The positions of different types of protons were affirmed by ^{1}H-^{1}H DQF-COSY spectrum (**Figure 16**). In the DQF-COSY spectrum, H_a correlated with H_b, and H_c correlated with H_d as expected. There was a weak correlation between H_d and H_c which indicated the presence of a long-range coupling that normally occurs in aromatic systems.[57]

The compound's symmetry was re-confirmed by its ^{13}C-NMR spectrum which revealed seven types of carbons (**Figure 17**). According to the chemical shift values, the carbon groups were assigned as in the **Figure 17**. There were two signals that could be easily identified based on their chemical shift values. The highest chemical shift at 169.75 ppm was the carbon in C=O groups as it is directly bonded to an electronegative atom like oxygen. The signal at 136.24 ppm has the second highest chemical shift which belongs to the α-carbon to the C=O groups in the aromatic ring. The signals from 120 to 140 ppm represented the carbon atoms of the aromatic ring. Two signals at 42.09 and 43.76 ppm corresponded to carbons in the methylene groups. Thanks to ^{1}H-^{13}C HSQC, it was possible to determine the exact signals for the remaining carbons by

disclosing the proton-carbon single bond correlations in the structure (**Figure S1** in Appendix A). ^{1}H-^{13}C HSQC spectra agreed with ^{13}C-NMR analysis that there was no hydrogen attached to carbon at position 6 and 7. All the information extracted from the various NMR techniques supported the conclusion that the product of the first step in the ligand synthesis was *N*^{1}, *N*^{3}-Bis(2-aminoethyl)isophthalamide.

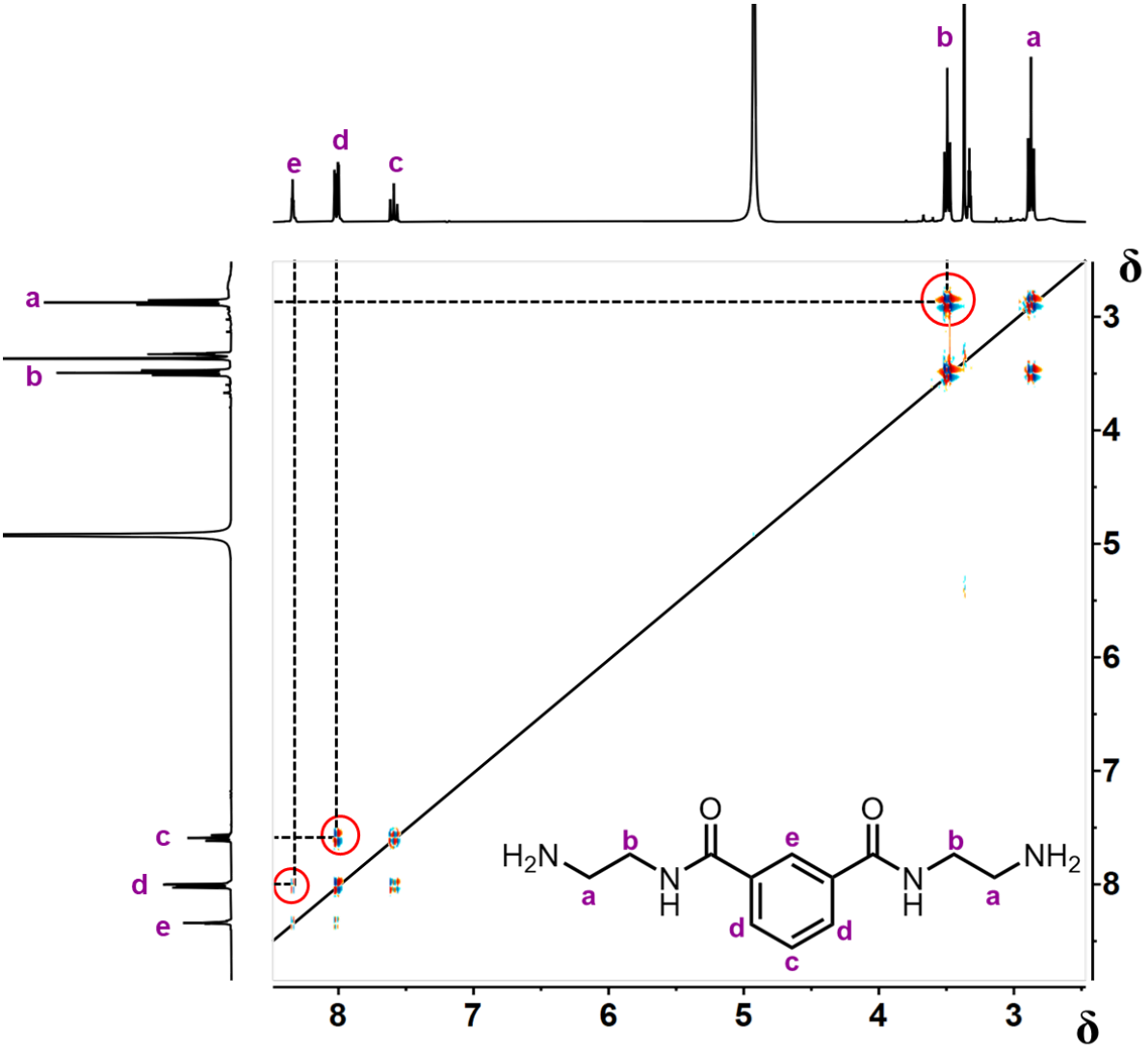

Figure 16. ^{1}H-^{1}H DQF-COSY spectrum of *N*^{1}, *N*^{3}-Bis(2-aminoethyl)isophthalamide (MeOD, 25°C).

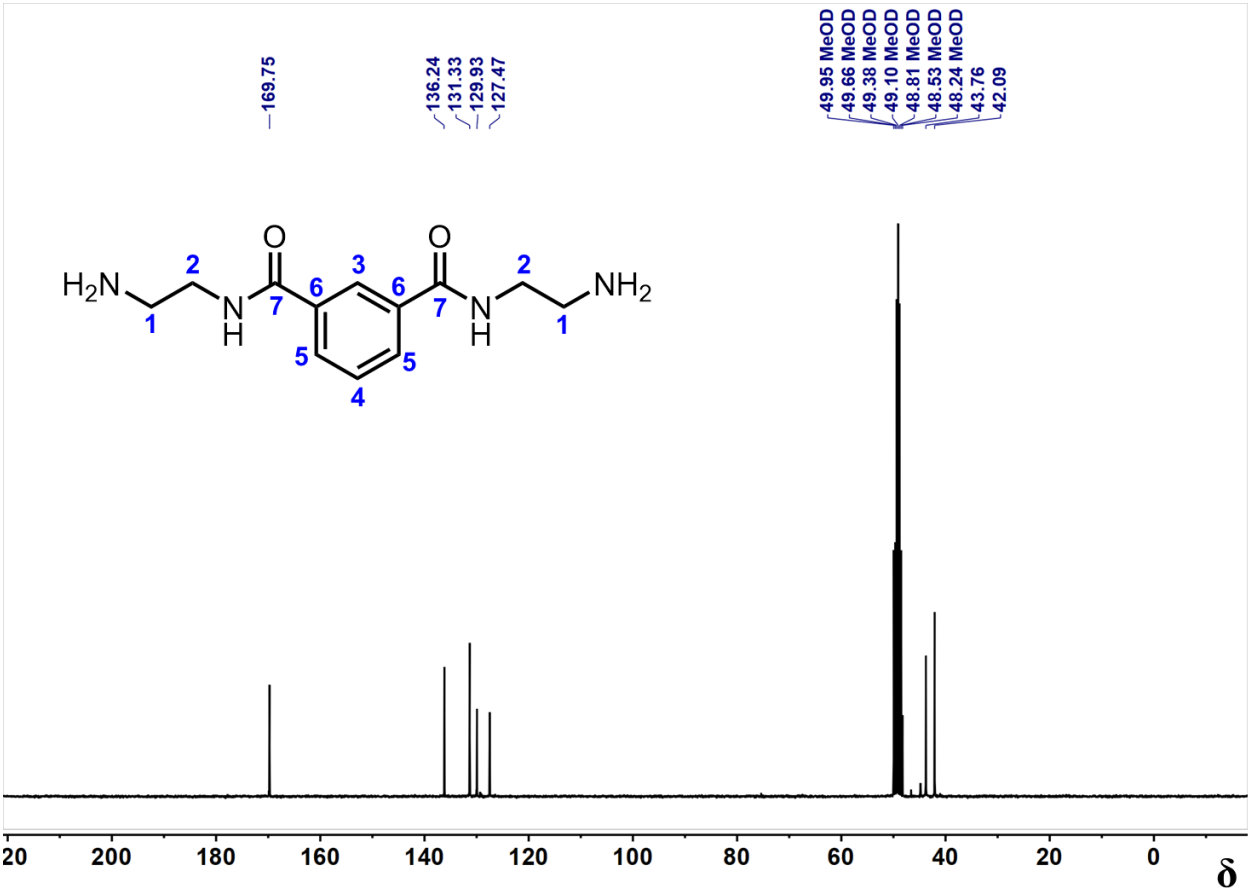

Figure 17. ^{13}C-NMR of of *N*^{1}, *N*^{3}-Bis(2-aminoethyl)isophthalamide (MeOD, 25°C).

3.1.2. Characterization of the ligand L1

The structure of ligand L1, also known as *N*^{1}, *N*^{3}-bis(2-(bis(pyridin-2-ylmethyl)amino)ethyl)isophthalamide, was elucidated by various NMR techniques (^{1}H-NMR, ^{13}C-NMR, ^{1}H-^{1}H DQF-COSY, and ^{1}H-^{13}C HSQC) and TOF-ESI-MS. In ^{1}H-NMR (**Figure 18**), the sum of all integral values matched with the total number of protons attached on carbons of the ligand L1. Combined with chemical shift information, integral values, and signal multiplicity, all protons in the molecular structure could be accounted for in **Figure 18**. Two triplets at 2.78 and 3.57 ppm represented the protons of neighboring methylene groups (H_a and H_b). The singlet at 3.82 with an integral value of 8 belonged to the protons of group **c**. The signals from 7.0 to 8.5

ppm corresponded to protons directly attached to an aromatic ring. This region was complicated to analyze due to many overlapping peaks. Protons **k** was believed to have the highest chemical shift because they were aromatic protons nearest to the nitrogen in the ring. Compared to the ^{1}H-NMR of the starting material, *N*^{1}, *N*^{3}-bis(2-aminoethyl)isophthalamide, the second and third highest chemical shift could be assigned for protons at position **j** and **h**, respectively. Protons **d** were believed to be the most shielded protons among aromatic protons because the nitrogen in the ring does not remove electron density from the position **d** by resonance and they had the farthest distance to the second nitrogen outside the ring. Therefore, the signals of 9 protons at **e**, **f**, and **g** positions were the ones which overlapped with each other at 7.6 ppm.

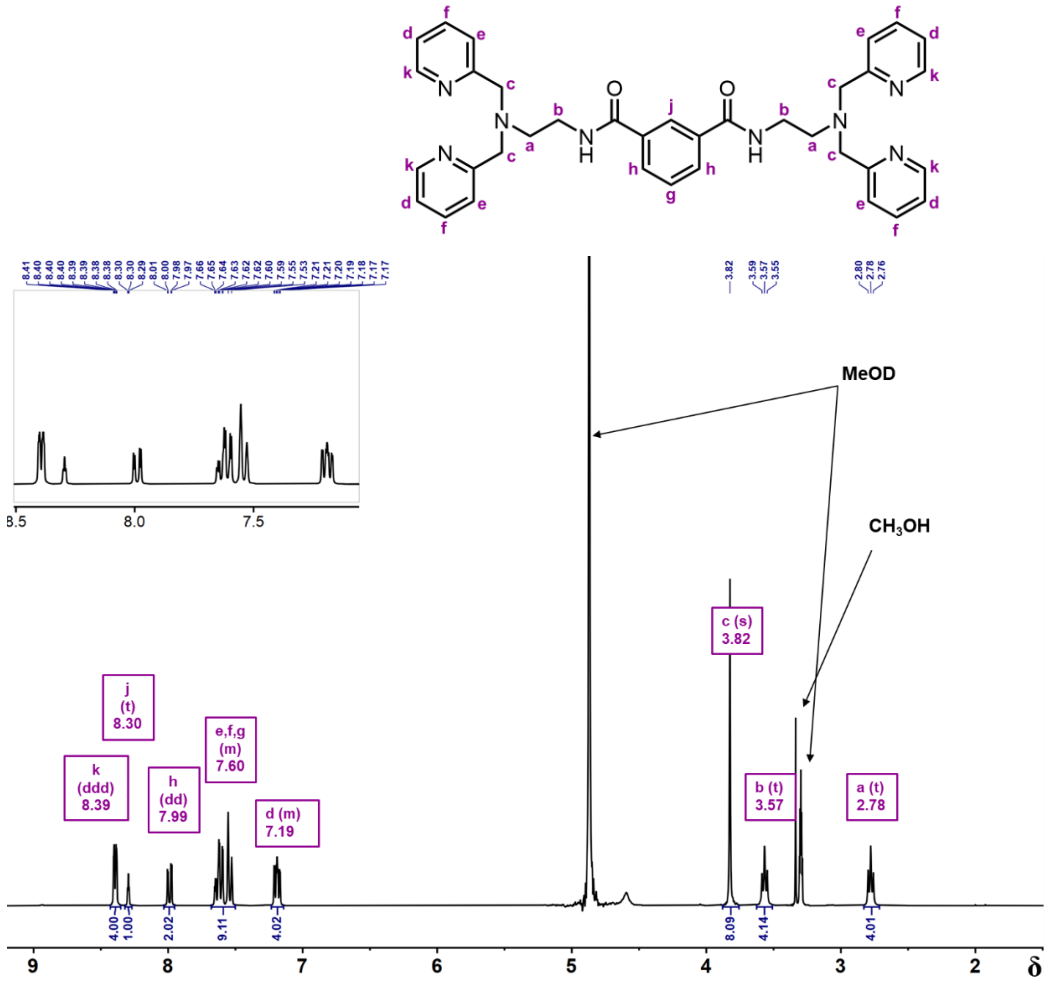

Figure 18. ^{1}H-NMR spectrum of the ligand L1 (MeOD, 25°C). Chemical structure of the ligand L1 (top) with labeled protons that correspond to signals on the ^{1}H-NMR spectrum (bottom).

The matching of protons and NMR signals were confirmed by ^{1}H-^{1}H DQF-COSY spectrum (**Figure 19**). In the ^{1}H – ^{1}H DQF-COSY spectrum, as predicted, H_a and H_b were correlated; H_d was correlated with H_k and H_f; H_g and H_h were also correlated. Additionally, ^{1}H-^{1}H DQF-COSY showed weak correlation of H_j to H_h due to their ^{4}J long-range coupling.

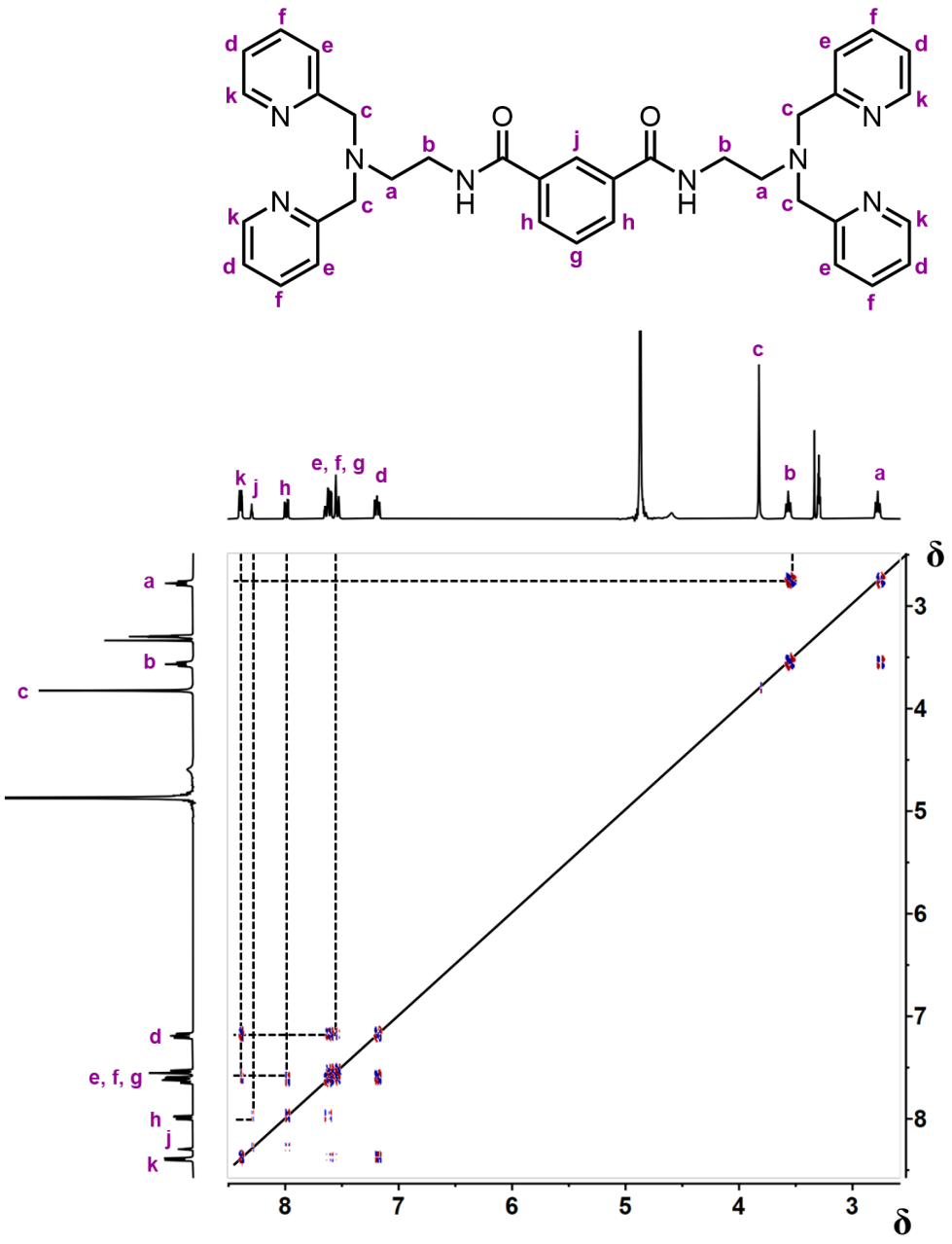

Figure 19. 2D ^{1}H-^{1}H DQF-COSY spectrum of the ligand L1 (MeOD, 25°C).

The number of peaks on the ^{13}C-NMR spectrum for the ligand L1 (**Figure 20**) was correctly found to be 13. Carbonyl carbons at C13 were expected to have the highest chemical shift because they directly bonded to oxygen atoms. Signals from 120 to 161 ppm belonged to aromatic carbons while the signals from 35 to 65 ppm were non-aromatic carbons. The second highest chemical shift is C12 on account of it being an aromatic proton directly connected to the nitrogen atom in the ring and only one carbon away from tertiary amine. C11 is the third highest chemical shift as it also bonded with the nitrogen in the ring, but further away from the tertiary amine. In the upfield region (δ25-65 ppm), C3 carbons are the most de-shielded because they are located between the aromatic ring and the tertiary amine. Further signal assignments were accomplished using ^{1}H-^{13}C HSQC NMR (**Figure 21**). In addition to NMR results, mass spectroscopy supported the positive identification of the ligand L1 as well. The calculated m/z values for $[L1+H]^{+}$ and $[L1+2H]^{2}$ were 615.3196 and 308.1637 correspondingly, both of which were close to the experimental m/z values found in the mass spectrum $[L1+H]^{+}$: 615.5187, $[L1+2H]^{2+}$: 308.2944 (***Figure 22***).

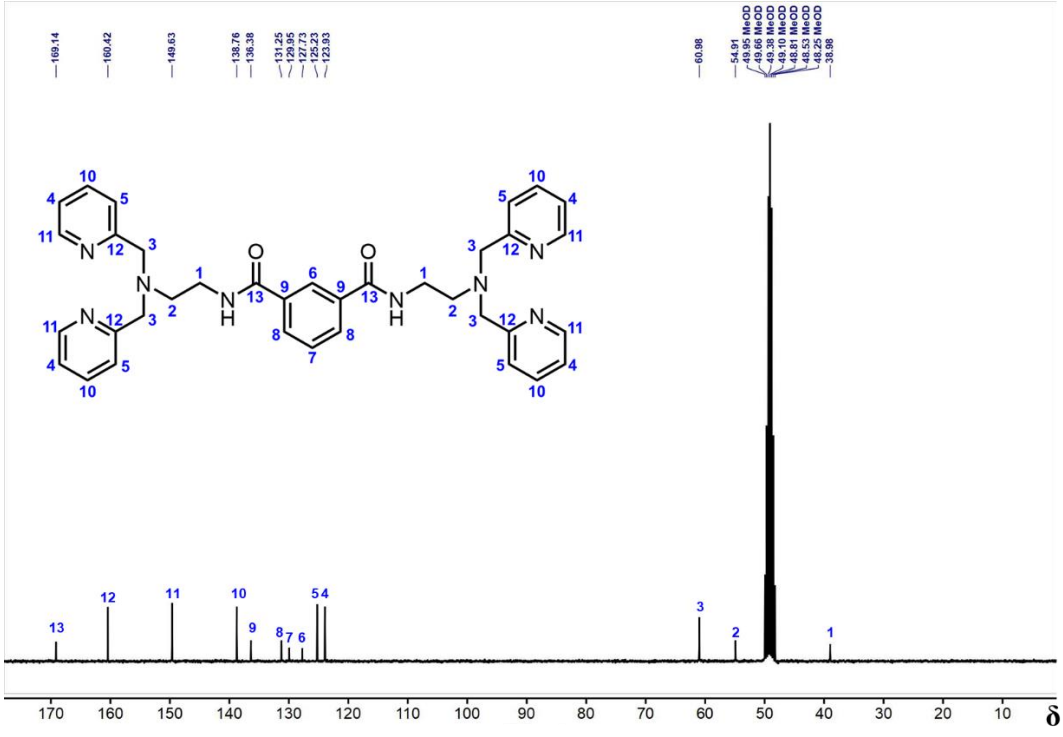

Figure 20. ^{13}C-NMR spectrum of ligand L1 (MeOD, 25°C).

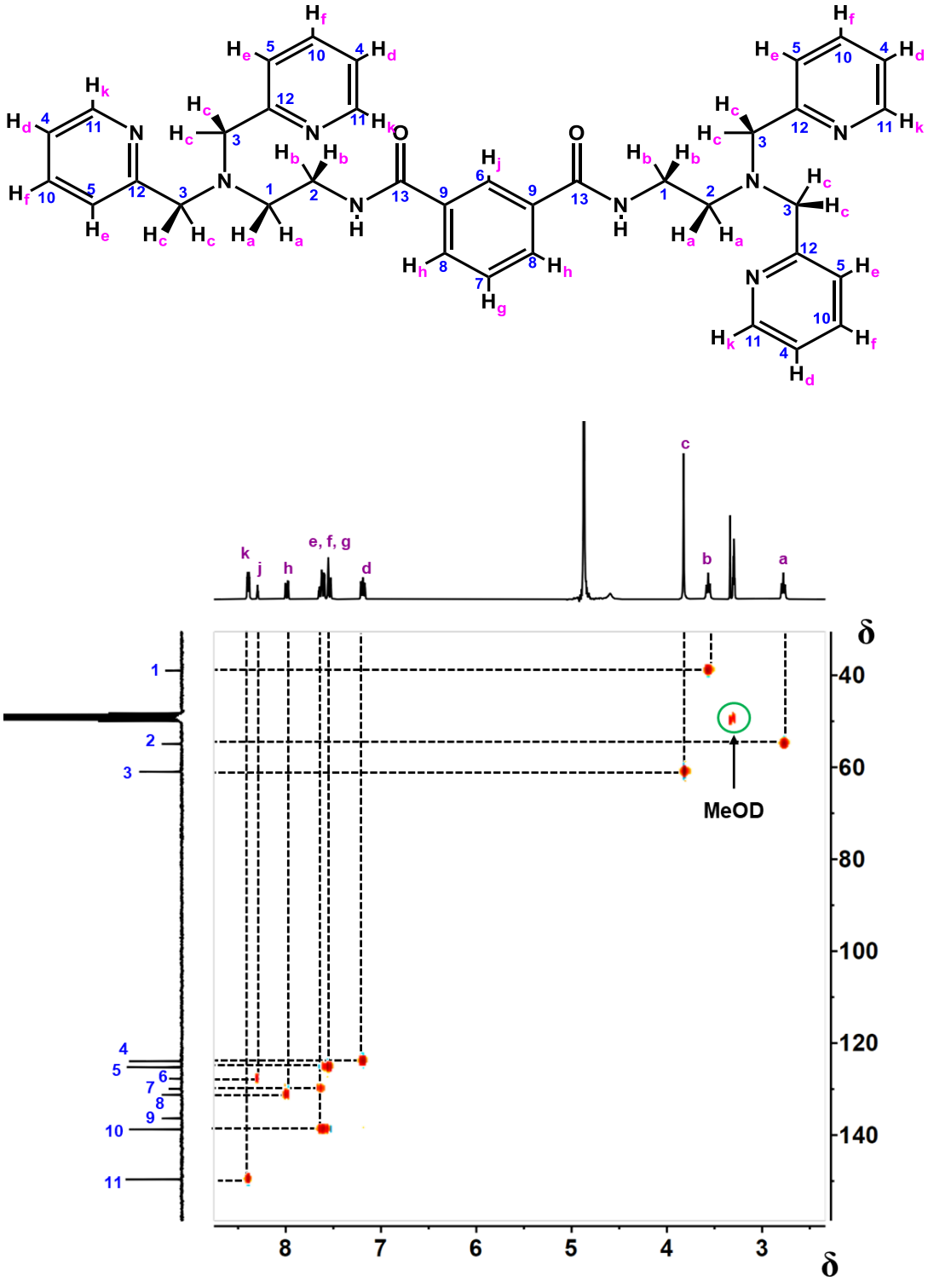

Figure 21. ^{1}H-^{13}C HSQC NMR spectrum of ligand L1 (MeOD, 25°C). C12 and C13 did not show up in the spectrum as they had no correlation with any protons.

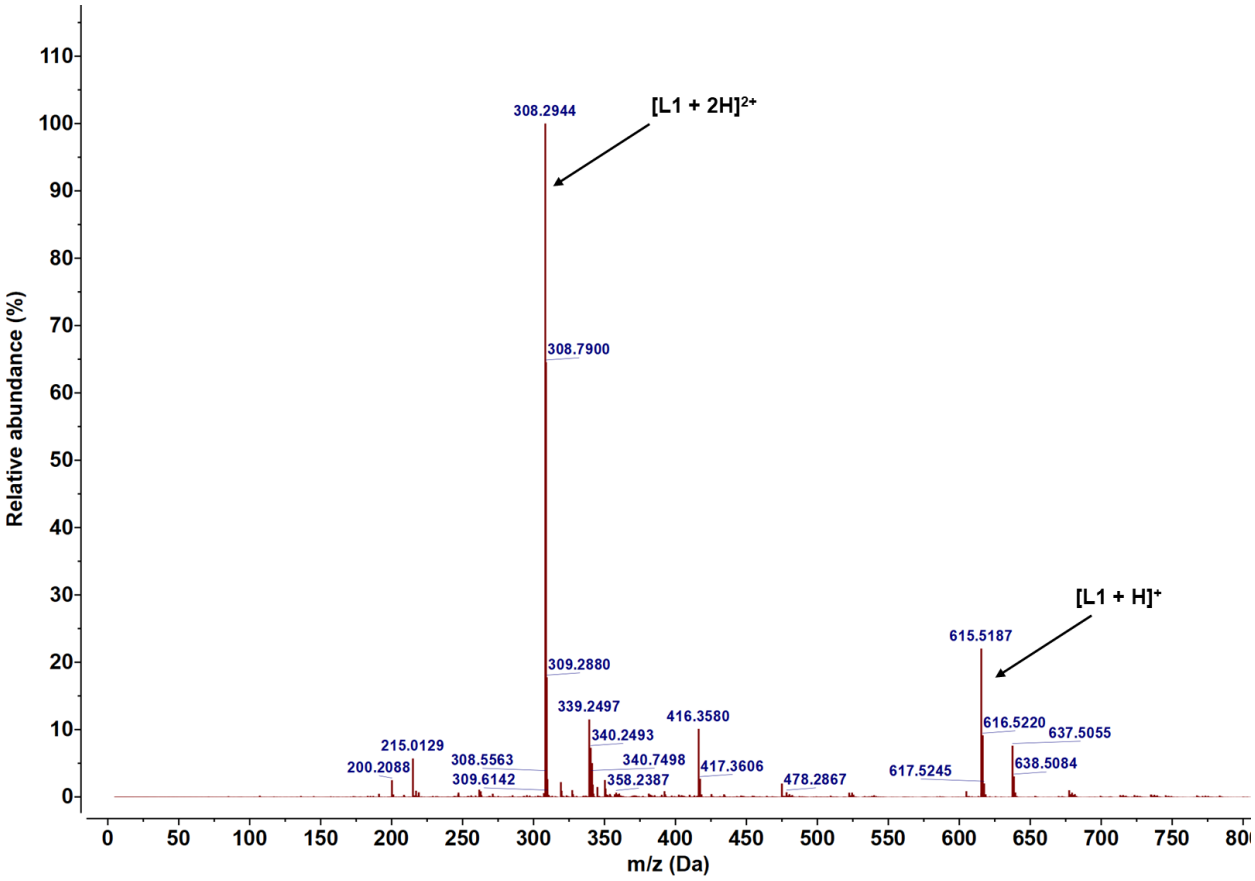

Figure 22. Mass spectrum of the ligand L1 (m/z expected = 614.31) (MeOH with 1% formic acid, 25°C).

3.2. Synthesis and Characterization of the Diiron Complexes

Two iron salts: iron(II) chloride and iron(II) triflate were used to form the diiron complexes and the reactions had an average yield 55% and 67% respectively. However, the characterization results of two iron complexes differed. ^{1}H-NMR experiments were conducted for two samples of the iron complexes with the acquisition parameters as following: 512 number of scans, 0.03 number of dummy scans, 0.063 acquisition time, and 200,000 Hz sweep width in ppm so that 1000 ppm could be scanned. The ^{1}H-NMR spectrum for $Fe_2^{II}Cl_n$(L1) (**Figure 23**) revealed two peaks at the far downfield region (51.84 ppm and 54.00 ppm) that was beyond the normal chemical shift region for proton NMR (δ0-12ppm). This pattern indicated that the compound was paramagnetic[58], a sign of coordination bonding between ligand L1 and the

paramagnetic iron(II) ions. Moreover, the m/z peak of the $Fe_2^{II}Cl_n(L1)$ complexes were detected in the mass spectrum (**Figure 24**) for the sample and confirmed the presence of the diiron complexes. M/z values for $[Fe^{II}_2Cl_2(L1)]^{2+}$: 398.1971 (calc m/z: 398.0597), $[Fe^{II}_2Cl_3(L1)]^{+}$: 831.3140, 833.3115 (calc m/z: 831.0882, 833.1121), $[Fe^{II}Fe^{III}Cl_2(L1)]^{+}$: 796.3277 (calc m/z: 796.1193), and $[Fe^{II}Fe^{III}Cl_4(L1)]^{+}$: 866.2841, 868.2814 (calc m/z: 866.0571, 868.0698) were detected. Mixed-valent diiron complexes were detected, suggesting that the sample might have come into contact with atmospheric oxygen when the sample was taken out of the glove box for the characterization. On the other, the proton resonances of $Fe_2^{II}(OTf)_4(L1)$ still fell in the typical chemical shift region of its ^{1}H-NMR spectrum (**Figure S2** in Appendix A), implying that the $Fe_2^{II}(OTf)_4(L1)$ complex was diamagnetic or that ligand L1 failed to bind with iron ions in iron(II) triflate salt. In the mass spectrum of $Fe_2^{II}(OTf)_n(L1)$ (**Figure S3** in Appendix A), no m/z peak could be found to be related to a diiron complex, suggesting that no diiron complexes had been formed during the reaction.

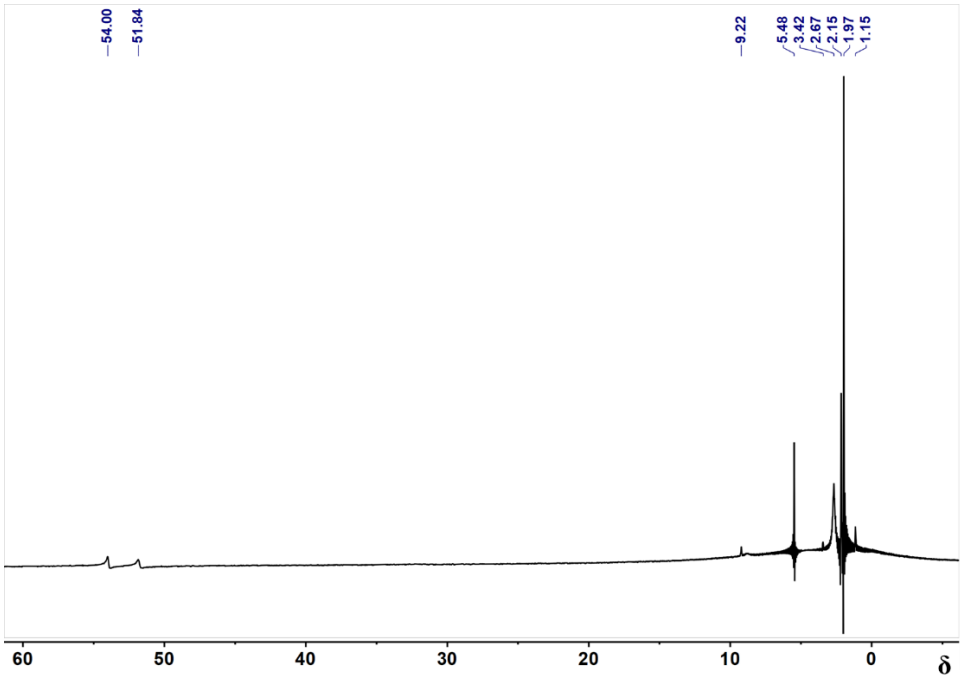

Figure 23. ^{1}H-NMR spectrum of iron complexes made from iron chloride salt (CD_3CN, 25°C).

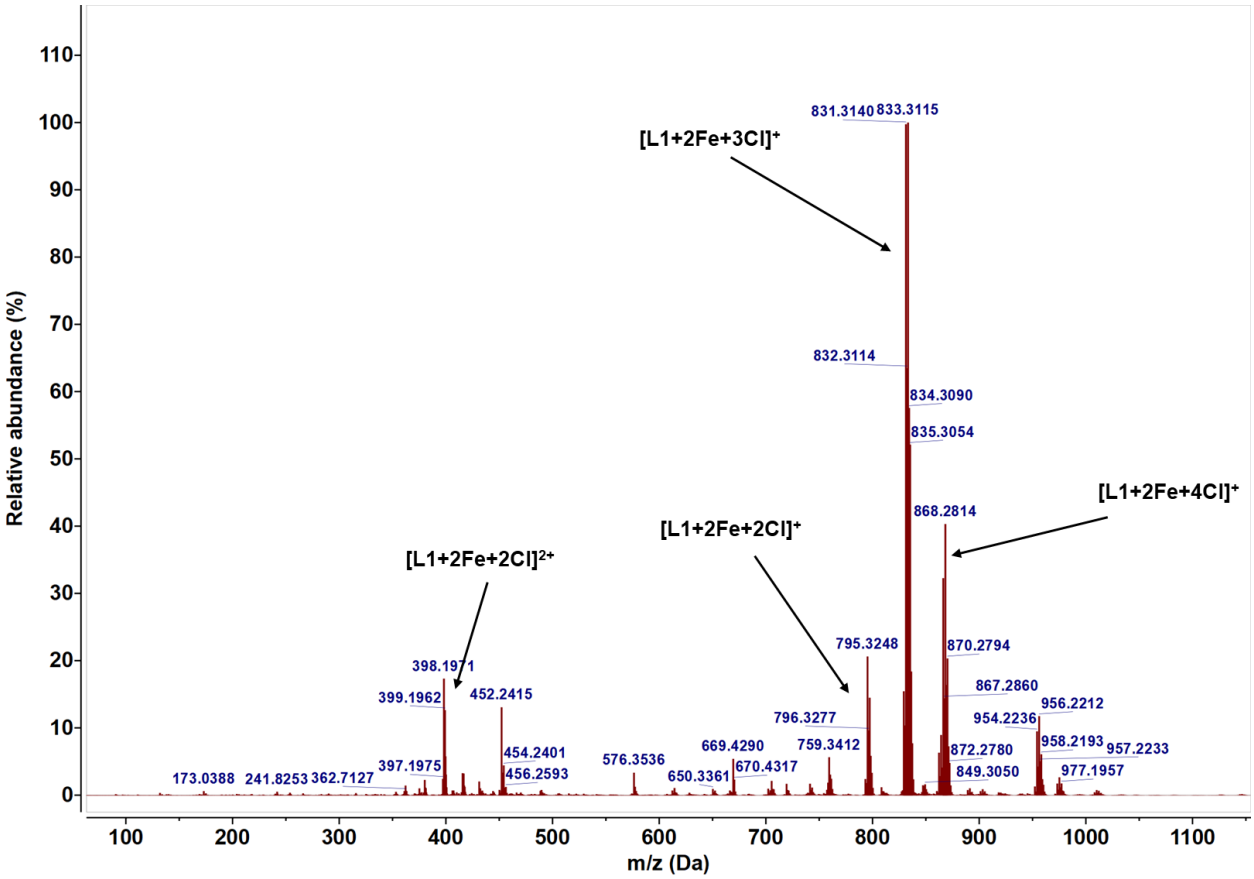

Figure 24. Mass spectrum of the iron complex formed by mixing iron(II) chloride with the ligand L1 in MeCN medium. Various mass peaks of diiron complexes with different number of chlorine atoms were recognized.

4. Conclusions and Future Directions

A two-step synthetic route for obtaining a coordination ligand capable of forming diiron complexes with iron salts was designed and carried out. This synthetic route proved facile and advantageous as it only contained two steps and by adjusting the length of the diamine in step 1 and the metal-binding units in step 2, a series of different ligands can be obtained. The route indeed afforded pure samples of the ligand L1. However, there will still be a need for other synthetic trials to improve the percent yield of the synthesis. ^{1}H-NMR and TOF-MS provided evidence that the ligand L1 had the ability to form diiron complexes when combined with iron(II) chloride but not with iron(II) triflate salt. Further attempts need to be carried out in order to increase the yield of

the diiron complexes, and form crystals suitable for X-ray crystallography which can provide 3D-structures of the complexes. There are numerous experiments that can be carried out with the ligand L1. For example, binding it with other iron salts to acquire a variety of other diiron complexes. With multiple diiron complexes in hand, their ability to catalyze water oxidation can be carried out electrochemically. Cyclic voltammetry (CV) will be conducted in order to determine all the possible redox states that can be accessible under electrochemical conditions. Then the efficiency of the iron complexes as catalysts for water oxidation can be evaluated using CV and gas chromatography. Their redox properties as well as their efficiency as water oxidation catalysts (WOCs) can also be evaluated. Overall, this work brings us closer to designing inexpensive and efficient water oxidation catalysts.

CHAPTER III

REVIEW OF THE DEVELOPMENT OF BIS-BIPYRIDINIUM-BASED GEMINI SURFACTANTS FOR TEMPLATE-DIRECTED SELF-ASSEMBLY

1. Introduction

Surfactants are molecules that can be found in regular products like soaps and detergents. They are comprised of amphiphilic structures containing both hydrophobic and hydrophilic regions. This amphiphilic nature endows surfactants with the ability to self-organize and assemble into various supramolecular superstructures ranging from simple geometrics to very hierarchical and complex shapes, the latter of which are beneficial for more advanced applied areas of sciences such as drug delivery or molecular nanotechnology. The fundamental understandings of surfactants and the factors that control their self-assembly are important for designing smart systems that can be tuned or modulated in a prescribed manner. One strategy to regulate and promote the self-assembly process is incorporating functional units into the surfactants' structure that are capable of forming non-covalent interactions with guest/template molecules that serve to minimize repulsion among the charged head groups of surfactants. The process can be called template-directed self-assembly. This chapter aims to provide general knowledge of surfactants and their self-assembly process, as well as significant findings of the self-assembly of gemini surfactants, a special type of surfactants. Gemini surfactants typically perform better in terms of their surface activities such as the ability to reduce water surface tension of water or increase water wetting ability. Their self-assembly often produces superstructures with a unique variety of morphologies as compared to conventional surfactants. The chapter also presents up-to-date developments in the area of gemini surfactants constructed with bis-bipyridinium units as head groups for template-directed self-assembly, which the research reported in Chapter 4 is based on.

2. Literature Review

2.1. Surfactants and their Self-Assembly Processes

Amphiphiles are composed of both a hydrophilic (water-loving) "head" group and a hydrophobic (water-hating) tail. To clarify, the hydrophilic "head" groups of amphiphiles attract water molecules as their structures may contain ionic, or non-ionic groups. The tails contain either saturated or unsaturated long hydrocarbon chains giving them water-repelling and water-insoluble properties. Amphiphiles can be divided into several subclasses based on their structure: linear amphiphiles, bolaamphiphiles, dimeric amphiphiles, and dendritic amphiphiles[59] (**Figure 25**). The conventional amphiphiles are known as linear amphiphiles because they only contain one hydrophilic head group and one hydrophobic tail connected in a linear fashion. In bolaamphiphiles' structure, two polar head groups are attached to both ends of a long hydrophobic chain. Dimeric amphiphiles are amphiphiles which contain two head groups, two tails, and a spacer/bridging unit. When the spacer unit helps to link a hydrophilic group to a hydrophobic group in of dimeric amphiphiles, they are called twinned amphiphiles. The type of dimeric amphiphiles that have a spacer unit connected to two hydrophilic heads (or two hydrophobic tails) are called gemini amphiphiles. Among all these subclasses, the structure of dendritic amphiphiles possesses a higher degree of branching with multiple head groups and tails.

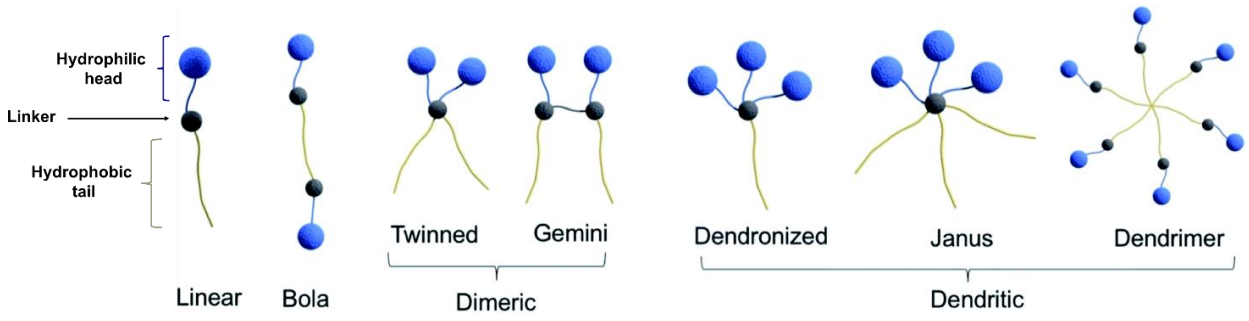

Figure 25. Classification of amphiphiles based on their structure. Reproduced with permission from reference 59. Copyright 2020, CC BY 3.0.

Surfactants are amphiphiles which can lower the surface tension of water or the interfacial tension between hydrocarbons and water. Surfactants have a wide range of applications from daily products,[60] for example soaps, shower gels, shampoos, and cosmetics to more advanced uses in bioremediation[61], gene delivery,[62] drug delivery[63], or bioconversion of biomass to biofuels.[64,65] When surfactants are present in water, their polar head groups remain solvated while the hydrophobic tails migrate above the interface forming an insoluble layer at the air-water interface known as a Langmuir film. This insoluble layer exerts a certain amount of force, disrupting the cohesive energy at the interface, and thus lowering the surface tension of water. When the concentration of surfactant increases, they undergo a concentration dependent self-assembly process which leads to the formation of larger molecular ensembles such as micelles, vesicles, or bilayer structures.[59] In these superstructures, their hydrophobic tails bury themselves inside the structure away from water. The utilization of this self-assembly process of surfactants is one of the main strategies to construct hierarchical complex supramolecular architectures, including biomolecular and nanoparticle systems with applications in diverse areas of chemistry[66], material science[67], and nanotechnology[68]. The self-assembly process first starts when the surfactant concentration reaches a certain value, the critical micelle concentration (CMC) ***(*Figure 26**). The surfactants can form into higher ordered structures when the concentration continues increase to a second level of assembly called the critical aggregation concentration (CAC) (**Figure 26**). The main driving force for the formation of the surfactant self-assemblies is a solvophobic mechanism, also known as the hydrophobic effect. This non-covalent interaction increases entropy by releasing highly ordered water molecules from the surfactant's hydrophobic tails, an increase that is larger than the decrease of entropy due to surfactant assembly. However, when more amphiphiles are

present in the solvent, negative cooperativity can limit the aggregates' size due to Coulombic and steric repulsion between the amphiphilic head groups.

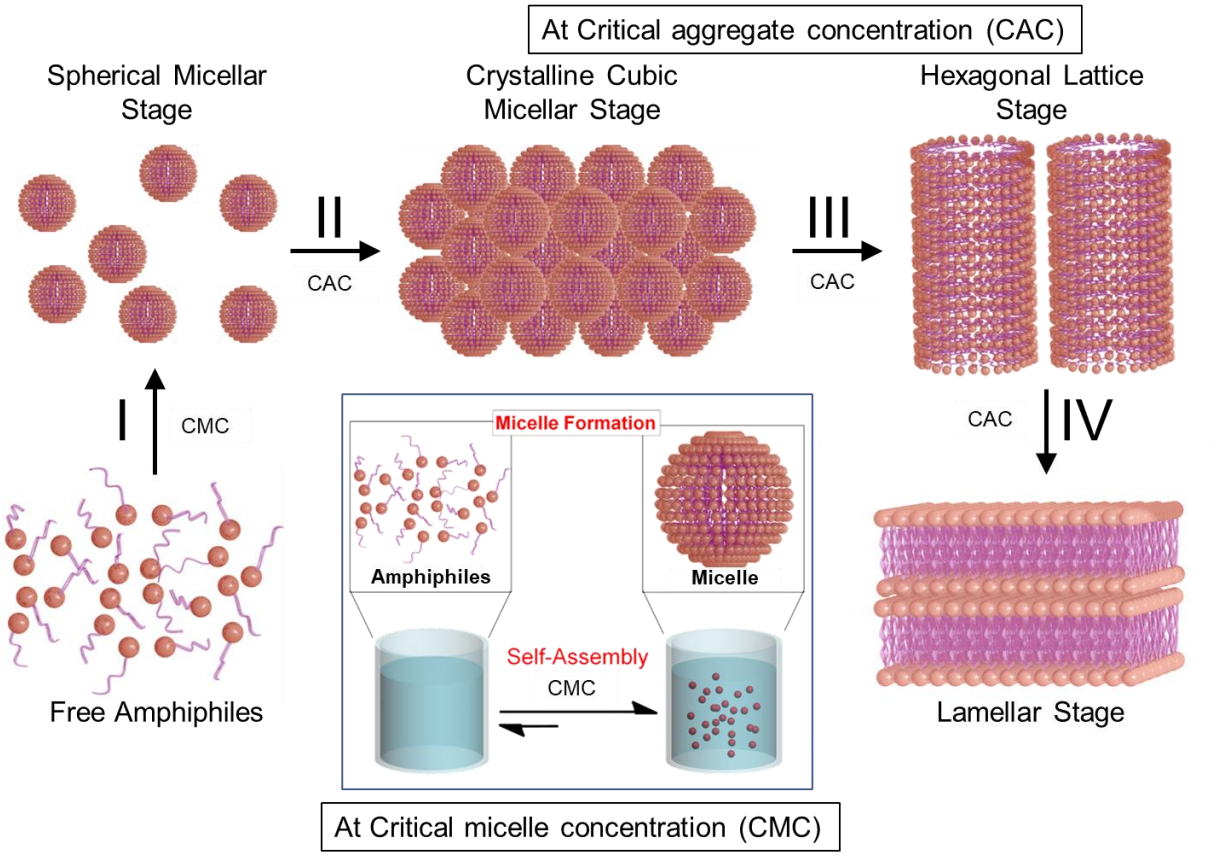

Figure 26. Graphical representation of the self-assembly of surfactant amphiphiles.

2.2. Thermodynamics of the Self-Assembly of Surfactants

The self-assembly of surfactants occurs spontaneously when the concentration of surfactants reaches its critical concentrations. How favorable this process can be depends on various factors including the structure of the surfactant and the solution conditions. Traditional models of the free energy of aggregation accounts for at least six free energy contributions: 1) transfer free energy of the surfactant tail, 2) the aggregate core-water interfacial free energy, 3) deformation free energy of the surfactant tail, 4) head group steric interactions, 5) head group dipole interactions, and 6) head group ionic interactions.[69,70] The transfer free energy contribution

stems from the process in which the hydrophobic tails of the surfactants are transferred from water to the hydrophobic core of the aggregate. This process provides a large negative contribution to the free energy of micellization. The interfacial free energy is the energy needed for the formation of an interface separating the hydrophobic core from the water medium. When the aggregation number increases, the interfacial free energy will decrease favoring the generation of larger aggregates. Contradistinctively, the deformation free energy (the constraint of one end of the hydrophobic tail at the aggregate-water interface), head group steric interactions (steric repulsions caused by the crowded head groups), head group dipole interactions (repulsion among head groups caused by dipole-dipole moment), and the head group ionic interactions (electrostatic repulsion between ionic surfactants) all contribute positively to the free energy of micellization. These free-energy contributions increase as more aggregates assemble essentially disfavoring the self-assembly process with regards to its spontaneity and ultimately limits the size of the micellar aggregates. Understanding how to regulate these free-energy contributions is the key to controlling and directing the self-assembly process.

2.3. Enhanced Performance of Gemini Surfactants

Gemini amphiphiles are more efficient than their linear counterparts and their self-assembly is more favorable for constructing highly complex architectures. Gemini surfactants generally have lower CMC values, higher solubility thanks to two hydrophilic head groups, better surface activity, lower Kraff temperature (the lowest temperature at which micelles start to form), and more diverse aggregate morphologies than their analogous linear derivatives [71,72]. The variety of more complex morphologies makes gemini amphiphiles a better selection to construct highly-ordered systems like polymers or nanoparticles. Camesano and Nagarajan explained why gemini surfactants tend to have lower CMC values and generate larger micelles using a thermodynamic

model[73]. As gemini surfactants contain two hydrophobic tails, their transfer free energy contributions have larger negative values than monomeric surfactants leading to much lower CMC values. The spacer that covalently linked two head groups in a gemini surfactant exerts a critical influence on the free energy contributions of the self-assembly process allowing the formation of aggregates to occur at lower concentrations and with larger sized morphologies, for example threadlike micelles, vesicles, and lamella. Another free energy contribution needs to be added into the thermodynamic model of self-assembly to account for the presence of the spacer that shields the hydrophobic core from coming into contact with water molecules. This term introduces another negative contribution to the overall free energy of micellization and thus the spacer itself is a factor in lowering the CMC. In the case of charged gemini surfactants, a sufficiently short spacer can pull two head groups close to one another, creating a nonuniform distribution of charge. This in effect, reduces the electrostatic repulsion between head groups. A short spacer can also lessen the distance between the two tails, which generates an extra packing contribution to the overall free energy of micellization. This contribution drops with micellar growth, thus favoring larger micelles.

Several general structure-property relationships of gemini surfactants have been elucidated. The CMC values of charged gemini surfactants are determined by the length of their hydrophobic tails, the structure of their spacers, and the type of counterion. More precisely, CMC values drop when the hydrocarbon tails of the gemini surfactants become longer due to the increase of hydrophobicity.[74-76] Meanwhile, CMC values slowly increase with increases in spacer length; however, CMC values start to decline once the length of the spacer reaches to certain limit.[77,78] This phenomenon is related to the change in distance between head groups when the spacer's length increases.[79] Two head groups become further apart when the length of the spacer grows

making the CMC values larger. When the spacer is too long, its high hydrophobicity and flexibility triggers its folding, thus shortening the distance between the head groups. Not only does altering the spacer's length affect the CMC values but polar groups or aromatic rings can also be incorporated into the spacer. The addition of polar groups raises the hydrophilicity of the spacer, and the introduction of an aromatic ring enhances rigidity in the bridge, both of which lead to an increase in CMC.[80,81] Furthermore, the CMC values can be further perturbed depending on the type of counterion.[82] The gemini surfactants with bromide counterions have lower CMC values than those with chloride counterions; the chlorides bring much more soluble. Moreover, gemini surfactants with organic anions instead of halides self-assemble at much lower concentrations. These structure-property relationship findings of gemini surfactants provide an important foundation on which many research projects related to applications of surfactants can be explored.

2.4. Template-Directed Self-Assembly of Bis-Bipyridinium-Based Gemini Surfactants by Molecular Recognition.

Template-directed self-assembly by molecular recognition is an important strategy for exerting control over the aggregation process of amphiphiles by reducing the Coulombic repulsion between charged head groups. In this approach, amphiphiles are designed with functional molecular units that can recognize and interact noncovalently with specific molecular targets that serve as templates. The interaction between the amphiphiles and these molecular templates leads to the formation of "supramolecular amphiphiles" complexes that effectively direct and promote the self-assembly of the amphiphiles (**Figure 27**).[82-84] There are numerous non-covalent bonding interactions that can be incorporated into the process to trigger the assembly of aggregates such as hydrogen bonding,[85] metal-ligand coordination,[86] and π-π stacking donor-acceptor charge transfer (CT) interactions.[87] Among molecular recognition units, 4,4'-Bipyridinium units have been widely

incorporated in organic self-assembly systems[88,89] due to their π-electron deficiency, rendering them capable of forming donor-acceptor CT complexes with π-electron-rich aromatic compounds. When charged bipyridinium units serve as hydrophilic head-groups in amphiphilic structures[90-92], electrostatic repulsion among contiguously assembled molecules gradually builds up with increasing aggregation numbers. This ultimately limits the size of the micellar aggregates. Olson et al. reported[93] that the efficiency and effectiveness of paraxylene-bridged bipyridinium-based gemini surfactants (**I**.4X) were enhanced significantly with the introduction of π-electron rich di(ethylene glycol)-disubstituted 1,5-dihydroxynapthalene (**DNP-DEG**). The π-π stacking and CT interactions between the surfactants and the π-electron rich template had minimized repulsions among the head groups. As a result, the CAC was decreased by 39%, along with concomitant increases in hydrodynamic diameter, and ζ-potential.[93] In addition, the structures of surfactants and templates can be designed to modulate other aggregate properties, including controlling the micellar self-assembly process in a switchable manner. These template-directed systems are much more amenable to structure-property tuning, as both the amphiphile and the template can be structurally modified to suit a particular application.

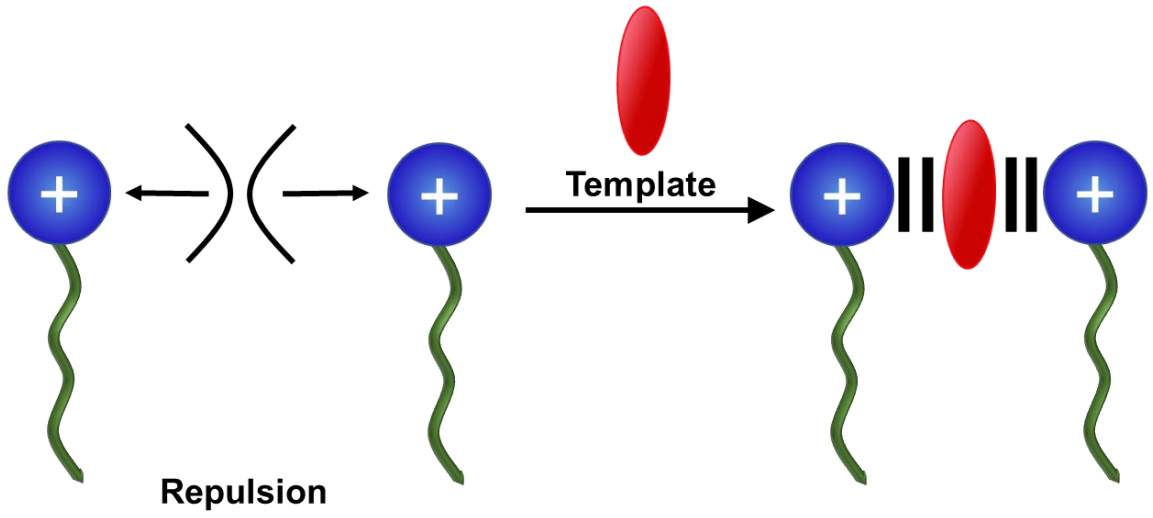

Figure 27. Graphical representation of the template effect on charged surfactants.

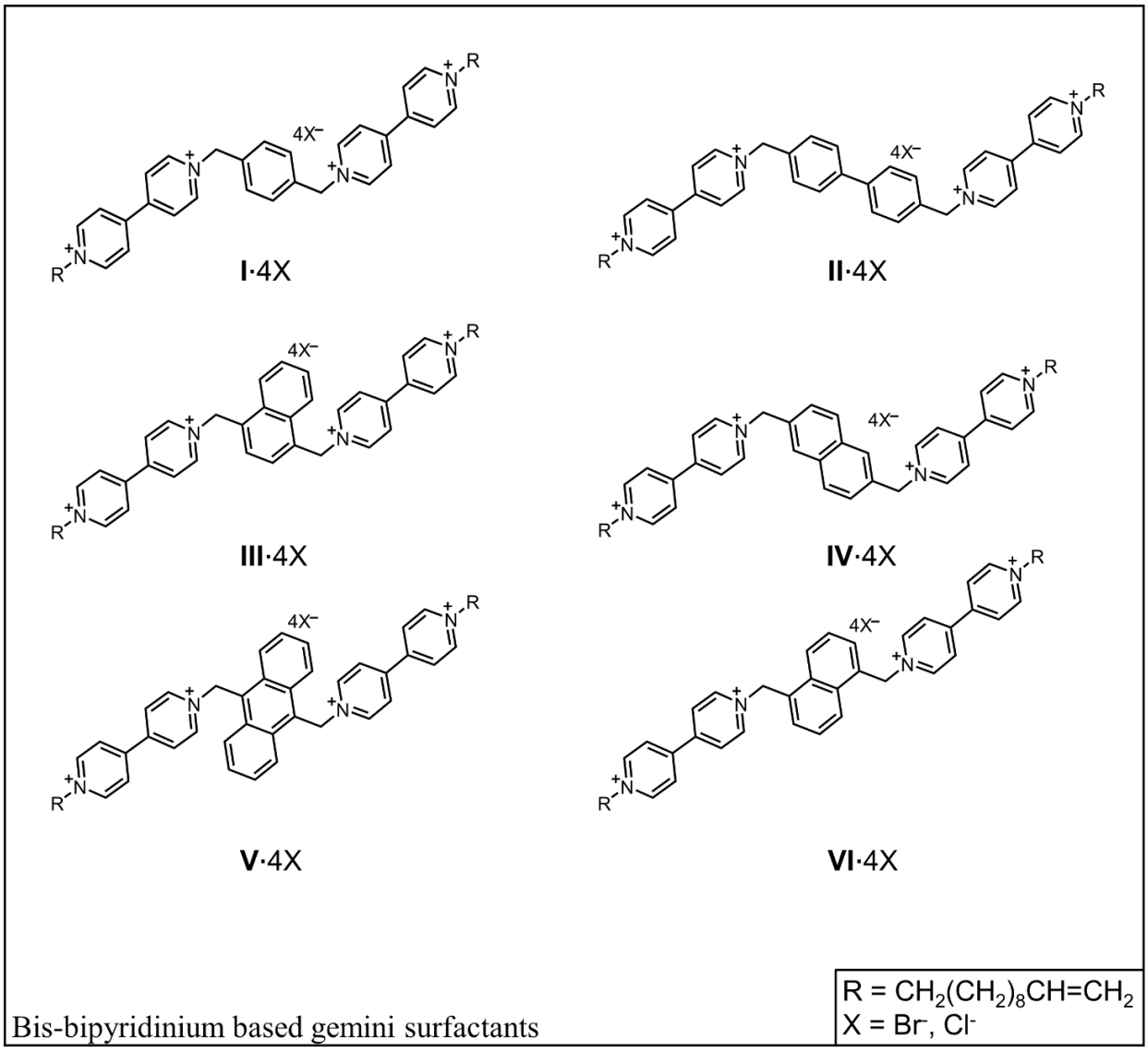

Figure 28. Bis-bipyridinium based gemini surfactants were investigated.

Different π-electron rich molecules have been investigated as potential templates for the self-assembly of paraxylene-bridged bipyridinium-based gemini surfactants. Olson et al. investigated the self-assembly of **I**.4X (**Figure 28**) with the template tri(ethylene glycol)-disubstituted 1,5-diaminonaphthalene (**DAN-TEG**, see **Figure 29**) containing secondary amine groups in its structure.[94] They demonstrated the reversible change in morphology of micellar aggregates from oblate ellipsoid to lamellar with the addition of the template.[94] The assembly and

disassembly of the aggregate with and without templates could be reversibly controlled under acid-base control, with the secondary amine groups of the template being protonated and charged with the addition of acid.[94] The neurotransmitter melatonin (**Mel**) was another excellent template for the self-assembly of gemini surfactants discovered by Olson's research group in 2018[95] (**Figure 29**). The CMC of the reported gemini surfactant decreased by about 52% and the surface pressure increased by 8.5% with the addition of two equivalents of melatonin.[95] Meanwhile, L-tryptophan (**L-Tryp**) was found to be an ineffective template for this process because its structure did not allow for strong π-π stacking interactions (**Figure 29**).[95] Several biologically-derived melatonin isosteres including agomelatine (**AM**), methoxytryptophol (**MT**), *N*-acetylserotonin (***N*-AS**), and *N*-acetyltryptamine (***N*-AT**) (**Figure 29**) were also investigated for their template activity in water with paraxylene-bridged bipyridinium-based gemini surfactants.[96] Compared to melatonin, the incorporation of these isosteres into solutions of the bipyridinium-based gemini surfactants led to a greater decrease in CMC (up to 70%), accompanied with a 28% increase in surface pressure and a 20% decrease in contact angle.[96] Of all the templates examined, the four melatonin isosteres could direct the self-assembly of paraxylene-bridged bipyridinium-based gemini surfactants the most efficiently and effectively, whereas L-tryptophan had poorest activity. Thus, a small variation in chemical structure of the template lead to an enormous difference in its effects on the surface activity of the surfactant.

A family of bis-bipyridinium-based gemini surfactants have been expanded and studied from which structure-property relationships that govern the aggregate morphology could be revealed. Olson, Fang, et al. reported a novel bis-bipyridinium based-gemini surfactant with a biphenyl bridge that underwent template-direct self-assembly with π-electron rich **DNP-DEG** and formed helical-fiber-based hydrogels that were processed into stimuli-responsive soft materials

that displayed changes in physical states (gel-sol and sol-gel) and color in response to changes in temperature.[97] Olson, Fang, et al. studied six different bis-bipyridinium based-gemini surfactants with various phenyl bridging units (**Figure 28**) and confirmed that the length of the spacing unit regulated the formation of hydrogel and its strength.[98] When the length of the bridge was equal to or larger than 6.3Å (**II**.4X, **IV**.4X, and **VI**.4X), hydrogelation occurred.[98] Spacer units have been proven to strongly effect the construction of hierarchical superstructures of template-directed self-assembled bis-bipyridinium based-gemini surfactants.

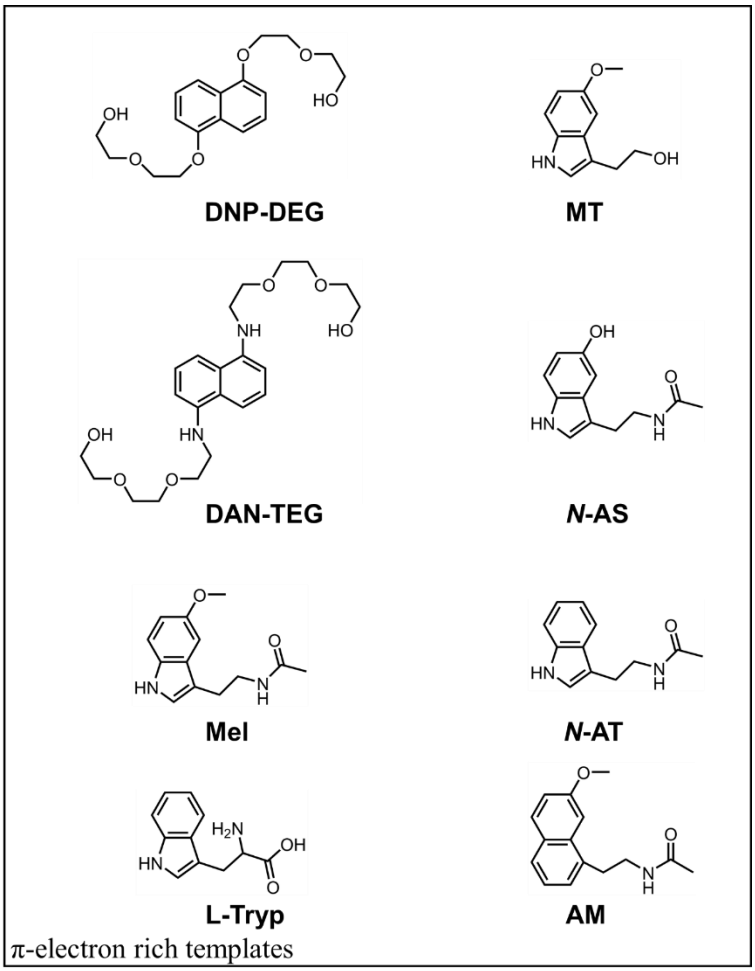

Figure 29. π-electron rich templates were investigated.

3. Conclusions

A fundamental understanding about surfactants including their structures, classifications, applications, and their self-assembly process has been introduced in this chapter. Surfactants are amphiphilic molecules containing both hydrophilic and hydrophobic regions that can undergo a concentration-dependent self-assembly process when dispersed in water which leads to the formation of different supra-architectures and lowers the surface tension of water. Surfactants and their self-assembly are being employed for numerous applications such as in soaps, detergents, or in bioremediation, gene delivery, drug delivery, bioconversion of biomass to biofuels, material sciences, and nanotechnology. Based on their molecular structure, surfactants can be categorized into four main classes: linear amphiphiles, bolaamphiphiles, dimeric amphiphiles, and dendritic amphiphiles. Gemini amphiphilic molecules which contain two hydrophilic head groups, two hydrophobic tails, and a spacer typically perform better than conventional linear amphiphiles with only one hydrophilic head group and one hydrophobic tail due to their lower CMC, higher solubility, better surface activities, and lower Kraff temperature. Their self-assembly process is more favorable in terms of free energy of micellization, and they can assemble into larger supramolecules with diverse morphologies. The general better performance of gemini amphiphiles can be understood from its thermodynamic model with at least six different free-energy contributions: transfer free energy of surfactant tail, aggregate core-water interfacial free energy, deformation free energy of the surfactant tail, head group steric interactions, head group dipole interactions, and head group ionic interactions. Their self-assembly of gemini surfactants can be further promoted by using molecular recognition strategies in which the gemini surfactants are designed to possess functional units that can non-covalently bind to specific molecules in an effort to reduce Coulombic repulsion between charged head groups. A family of bis-bipyridinium based

gemini surfactants have been developed which contain π-electron deficient bipyridinium units that are capable of forming π-π stacking and donor-acceptor CT complexes with π-electron rich molecules. The template-directed self-assembly was found to increase the efficiency and effectiveness of the surfactants in regard to their critical concentrations, aggregate size, and ζ-potential. The bridging unit of gemini surfactants were proved to have significant impacts on the aggregate's morphology.

CHAPTER IV

THE DEVELOPMENT OF ALKYL-BRIDGED BIS-BIPYRIDINIUM-BASED AMPHIPHILES FOR TEMPLATE-DIRECTED SELF-ASSEMBLY

1. Introduction

With an aim of expanding the structure-property relationships of the bis-bipyridinium-based gemini surfactants, three novel bis-bipyridinium-based gemini surfactants with alkyl bridges of differing length (**Figure 30**) were designed and synthesized. Their non-templated and templated self-assembly processes were also investigated. In the template-directed self-assembly, the π-electron rich donor molecular template, melatonin, served as "molecular glue" that decreased the electrostatic repulsion among the charged assembled gemini amphiphiles (**Figure 31**). The addition of the melatonin molecular template to solutions of the bipyridinium-based amphiphiles resulted in the formation of larger aggregates and a more thermodynamically favorable self-assembly process. The formation of CT complexes was confirmed by UV-Vis, ^{1}H NMR, 2D DOSY, and 2D ROESY NMR. The effects of melatonin on the self-assembly processes of the gemini amphiphiles was revealed with variable concentration conductivity measurements. This study lays a groundwork for further investigation into soft matter capable of undergoing template-directed self-assembly.

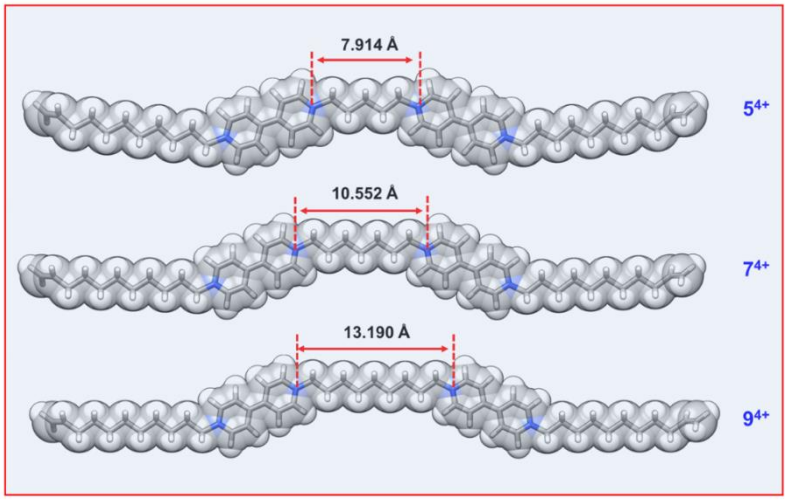

Figure 30. MM2 force field energy-minimized molecular models. The figure depicts the structures of three alkyl-bridge bis-bipyridinium-based gemini amphiphiles that developed in this research: $\mathbf{5}^{4+}$ (top), $\mathbf{7}^{4+}$ (middle), and $\mathbf{9}^{4+}$ (bottom).

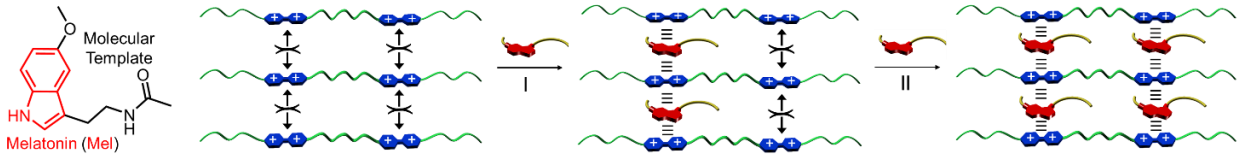

Figure 31. Graphical representation illustrating the template-directed self-assembly of $\mathbf{5}^{4+}$ and 1 eq. Mel (process I) and $\mathbf{5}^{4+}$ and 2 eq. Mel (process II). There is repulsion between two positively charged bipyridinium units. When melatonin molecules are introduced, the formation of donor acceptor charge transfer complexes mitigates the electrostatic repulsions between the charged bipyridinium species. This triggers the template directed self-assembly of larger superstructures in solution.

2. Materials and Methods

2.1. General Methodology

Chemicals used for the experiments including 4, 4' dipyridyl, 11-bromo-1-undecene, 1,5-dibromopentane, 1,7-dibromoheptane, 1,9-dibromononne, and melatonin were purchased from Sigma Aldrich and used as received. All solvents used in the experiments were reagent grade unless otherwise noted. For all the reactions, the vacuum and backfill cycle were performed to replace the reactive atmosphere with argon. Nuclear Magnetic Resonance experiments (^{1}H NMR, ^{1}H-^{1}H COSY NMR, ^{1}H-^{13}C HSQC NMR, ^{13}C NMR, ROSEY NMR, DOSY NMR) were performed on a Bruker Avance 300 MHz spectrophotometer using deuterated solvents purchased from Cambridge Isotope Laboratories, Inc. Conductivity was measured by Thermo Orion 550 equipped with a conductivity cell.

2.2. Design and Synthesis of Alkyl-Bridged Bis-Bipyridinium-Based Amphiphiles

The gemini amphiphiles were designed to possess two units of bipyridinium so that up to two molecules of π-electron rich melatonin can be bound to one molecule of the amphiphile. The ends of the hydrophobic alkyl tails contain a terminal double bond to promote polymerization and/or oligomerization in future research. Three gemini amphiphiles investigated in this study contain the same head groups and hydrophobic tail structures. They differ only in the length of the

alkyl-chain spacers which are 5 , 7, and 9 carbons long corresponding to the gemini amphiphile $\mathbf{5}^{4+}$, $\mathbf{7}^{4+}$, and $\mathbf{9}^{4+}$. The amphiphiles were successfully obtained through a reproducible synthetic route comprised of two subsequent S_N2 reactions: 1) the alkylation of 4,4'-Dipyridyl with 11-bromoundecene, and 2) a final alkylation with the appropriate dibromoalkane (**Scheme 3**).

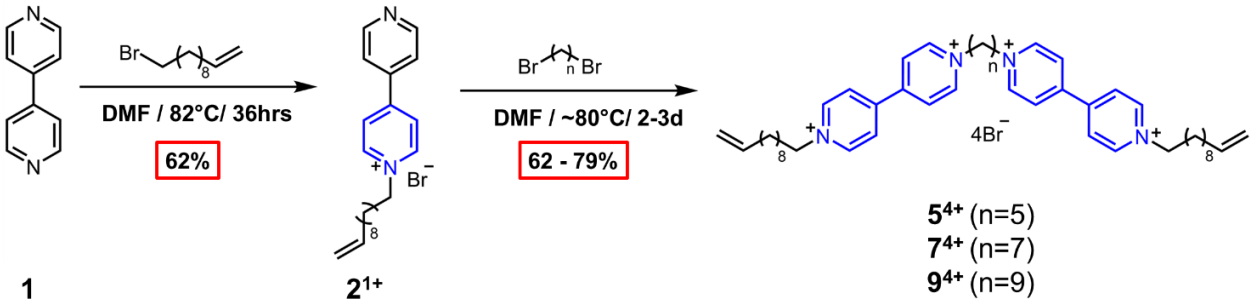

Scheme 3. The synthesis of bis-bipyridinium-based amphiphiles with different alkyl-chain-length-bridges ($\mathbf{5}^{4+}$, $\mathbf{7}^{4+}$, and $\mathbf{9}^{4+}$).

2.2.1. Synthesis of mono-undecylated bipyridine $\mathbf{2}^{1+}$ ($C_{21}H_{29}N_2^+.Br^-$, Mw = 389.38 g/mol): 4,4'-Dipyridyl (20.0 g, 128 mmol) was dissolved in 80 mL dry degassed DMF (DMF was degassed by argon purging for 1 hour). 11-bromo-1-undecene (28 mL, 128 mmol) was dissolved in 40 mL dry degassed DMF and then was added dropwise into the reaction. The reaction was refluxed for 36 hours at 82˚C. The reaction mixture was let cool to room temperature and a yellow-precipitate-side product was removed by filtration. The DMF filtrate was evaporated at 65˚C under reduced pressure and a brown oil was collected. The brown oil was then mixed with about 200 mL acetonitrile. Additional yellow precipitate was removed by filtration. The brown oil was acquired again by evaporating acetonitrile filtrate at 55°C under reduced pressure. Approximately, 200 mL ethyl acetate was added and mixed with the brown oil to precipitate the compound. The mixture was sonicated until the solid turned into fine powder. After filtering the ethyl acetate/solid mixture and washing it 3 times with 100 mL ethyl acetate and 3 times with 100 mL ethyl ether, the precipitate was dried under high vacuum. Finally, the light-brown-powdered product $\mathbf{2}^{1+}$ was

afforded (30.77g, 62%). ^{1}H NMR (CD_3CN, 300 MHz, 25 °C): δ = 1.32 (d, J = 20.6 Hz, 12H), 1.96 – 2.10 (m, 4H), 4.67 – 4.78 (m, 2H), 4.87 – 5.06 (m, 4H), 5.83 (ddt, J = 17.0, 10.2, 6.7 Hz, 1H), 7.85 – 7.93 (m, 2H), 8.46 (d, J = 7.1 Hz, 2H), 8.78 – 8.88 (m, 2H), 9.17 (d, J = 7.1 Hz, 2H); ^{13}C NMR (CD_3CN, 75 MHz, 25 °C): δ = 26.03, 29.13, 29.26, 29.48, 31.54, 33.91, 61.62, 114.25, 122.39, 126.38, 139.69, 141.73, 145.71, 151.55, 153.96.

2.2.2. Synthesis of 5-carbon-akyl-bridged bis-bipyridinium-based gemini amphiphiles 5^{4+} ($C_{47}H_{68}N_4^{4+}\cdot 4Br^-$, Mw = 1008.71 g/mol): Mono-undecylated bipyridine (3g, 7.70 mmol) and 1,5-dibromopentane (0.15 mL, 1.10 mmol) were dissolved into 15 mL anhydrous DMF. The reaction solution was degassed by purging it with argon gas for 1 hour. The flask system was then refluxed at 75°C for 48 hours under the presence of argon gas. After the reaction mixture was cooled, filtration was performed to collect a yellow precipitate. The precipitate was washed thoroughly with acetonitrile and ethyl ether three times each. The remaining solvent in the precipitate was further removed under high vacuum system. The 5-carbon-alkyl-bridged bis-bipyridinium-based gemini amphiphile $\mathbf{5^{4+}}$ was obtained as a yellow solid (0.79 g, yield 71%). ^{1}H NMR (D_2O, 300 MHz, 25°C): δ = 1.28 (d, J = 27.3 Hz, 24H), 1.46 – 1.63 (m, 2H), 1.91 – 2.09 (m, 12H), 4.64 – 4.78 (m, 8H), 4.85 – 5.05 (m, 4H), 5.86 (ddt, J = 16.9, 10.2, 6.6 Hz, 2H). 8.52 (dd, J = 7.2, 4.3 Hz, 8H), 9.09 (dd, J = 7.2, 5.3 Hz, 8H); ^{13}C NMR (D_2O, 75 MHz, 25°C): δ = 22.25, 25.06, 27.87, 28.05, 28.13, 28.22, 28.25, 30.09, 30.48, 33.04, 61.60, 62.24, 113.87, 126.90, 127.03, 140.36, 145.42, 149.86, 150.11.

2.2.3. Synthesis of 7-carbon-akyl-bridged bis-bipyridinium-based gemini amphiphiles 7^{4+} ($C_{49}H_{72}N_4^{4+}\cdot 4Br^-$, Mw = 1036.76 g/mol): Anhydrous DMF (15 mL), mono-undecylated bipyridine (3g, 7.70 mmol) and 1,7-dibromoheptane (0.16 mL, 0.94 mmol) were mixed then the reaction solution was degassed with argon purging for 1 hour. The reaction was heated at 80 °C

and refluxed under argon condition. After 67 hours, the reaction was stopped and cooled to room temperature. A yellow precipitate was collected by filtration and washed with acetonitrile (3 times) and ethyl ether (3 times). The precipitate was dried under high vacuum and a yellow powder was obtained as the product $\mathbf{7^{4+}}$ (0.77 g, 79% yield). ^{1}H NMR (D_2O, 300 MHz, 25°C): δ = 1.18 – 1.50 (m, 30H), 1.91 – 2.17 (m, 12H), 4.70 (t, J = 7.3 Hz, 8H), 4.86 – 5.05 (m, 4H), 5.78 – 5.95 (m, 2H), 8.53 (d, J = 7.0 Hz, 8H), 9.10 (d, J = 6.1 Hz, 8H); ^{13}C NMR (D_2O, 75 MHz, 25°C): δ = 25.09, 27.59, 27.90, 28.10, 28.18, 28.26, 28.29, 30.48, 33.07, 62.09, 62.24, 113.91, 126.91, 126.95, 140.28, 145.40, 149.91.

2.2.4. Synthesis of 9-carbon-akyl-bridged bis-bipyridinium gemini amphiphile $\mathbf{9^{4+}}$ ($\mathbf{C_{51}H_{76}N_4^{4+}\cdot 4Br^-}$, Mw = 1064.81 g/mol): Mono-undecylated bipyridine (2.68 g, 6.88 mmol) and 1,9-dibromononane (0.2 mL, 0.98 mmol) were dissolved in anhydrous DMF (15 mL). The reaction system was degassed with one-hour-argon purging. The reaction system was then refluxed at 80 °C under Ar gas for 64 hours. After the reaction completed, it was stopped and cooled to room temperature. Using filtration technique, a yellow precipitate was acquired. The precipitate was washed briefly with 10 mL DMF and thoroughly with acetonitrile and ethyl ether three times each. The precipitate was dried by putting it under high vacuum. The 9-carbon-alkyl-bridged bis-bipyridinium-based gemini amphiphile $\mathbf{9^{4+}}$ was obtained as a yellow solid (0.65 g, yield 62%). ^{1}H NMR (D_2O, 300 MHz, 25°C): δ = 1.15 – 1.46 (m, 34H), 1.92 – 2.14 (m, 12H), 4.69 (td, J = 7.3, 2.2 Hz, 8H), 4.86 – 5.06 (m, 4H), 5.86 (ddt, J = 17.0, 10.2, 6.7 Hz, 2H), 8.52 (d, J = 6.3 Hz, 8H), 9.09 (dd, J = 7.0, 2.3 Hz, 8H); ^{13}C NMR (D_2O, 75 MHz, 25°C): δ = 25.03, 25.22, 27.85, 27.97, 28.05, 28.12, 28.20, 28.23, 30.45, 30.60, 33.03, 62.18, 113.87, 126.87, 140.33, 145.37, 149.91.

2.3. Synthesis of π-π Donor-Acceptor CT Complexes

π-π donor-acceptor CT complexes are assembled when a π-electron deficient molecule is associated with a π-electron rich molecules through electrostatic and π-π stacking interactions (**Figure 32**). In the experiment, π-π donor-acceptor CT complexes were formed when the π-electron deficient bis-bipyridinium-based gemini amphiphiles were mixed with the π-electron rich compound, melatonin. For each gemini amphiphile, a set of three 5 mM solutions were prepared in Milli-Q water. One 5 mM solution served as a control sample with no melatonin added. One equivalent and two equivalents of melatonin were introduced into the other two 5 mM solutions of the amphiphile. Heat was applied to completely dissolve the melatonin. The solutions were then allowed to cool to room temperature before being analyzed.

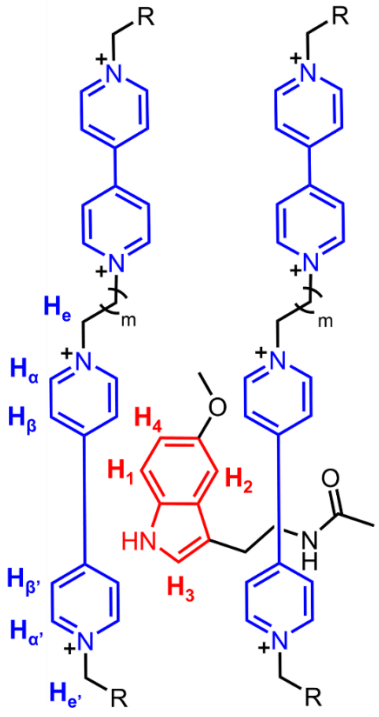

Figure 32. The interactions between a melatonin molecule (red) with two bipyridinium units (blue) of the gemini amphiphiles.

2.4. Bayesian DOSY Transformation and Determination of the Aggregates' Size

2D DOSY ^{1}H-NMR were performed for 5 mM solutions of gemini amphiphiles containing 2 equivalents of melatonin to investigate the assembly of micellar superstructures driven by CT complex formation. In 2D DOSY ^{1}H-NMR, the diffusion time Δ and the diffusion gradient length δ were optimized so that a 95% of the signal attenuation could be achieved. The typical range for the diffusion time Δ is from 0.02 to 0.5 s, and for the diffusion gradient length δ is from 0.5 to 3 ms. The raw data were resolved in Mestrelab Research S.L. by Bayesian DOSY transformation. The resolution, repetition, and diffusion points were selected so that the spectra displayed good signal-to-noise ratio, sufficient separation, and resolution in the vertical dimension. The diffusion coefficients obtained from the DOSY spectra were used to estimate the hydrodynamic radius of the aggregates formed when melatonin interacted with gemini amphiphiles. The hydrodynamic radius were calculated from the Stokes-Einstein equation: $R_h = k_B T/6\pi\eta D$ in which R_h is the hydrodynamic radius in meters; k_B (= 1.38065E-23 $m^2.kg.s^{-2}.K^{-1}$) is Boltzmann's constant; T (= 298 K for the experiment) is the temperature in Kelvin; η is the solvent viscosity (η of water at 298 K= 0.001002 $kg.m^{-1}.s^{-1}$; and D is the diffusion coefficient in m^2/s. From the hydrodynamic radius, the hydrodynamic diameter can be easily calculated. These calculations assume that the templated superstructure is spherical or that the superstructure is diffusing at the same rate as a spherical particle of a given size.

2.5. Determination of Critical Concentration Values

Conductivity measurements were performed to determine the critical concentrations of the gemini amphiphiles (**5**$^{4+}$, **7**$^{4+}$, and **9**$^{4+}$) with and without the templating influence of melatonin. Conductivity values were recorded for a range of concentrations from a saturated concentration to a very dilute solution. The critical concentrations were determined from the graph of conductivity

(μs/cm) as a function of the concentration (mM) due to an abrupt change in the slope values (**Figure 33**). In aqueous solutions of linear surfactants, when micelles begin to form, the conductivity of the solution begins to drop since micellar solutions contain fewer charged species diffusing in solution than solutions of free surfactant monomers.[99, 100] The intersection point of two linear lines before and after the micellization process is called the break point which corresponds to the CMC of the surfactant. In the case of cationic gemini surfactants, it is reported that they can have two critical concentration values[101]: the first one is the CMC where spherical micelles begin to form and a second one, the CAC, occurring after the CMC with the formation of larger most likely cylindrical-type superstructures.

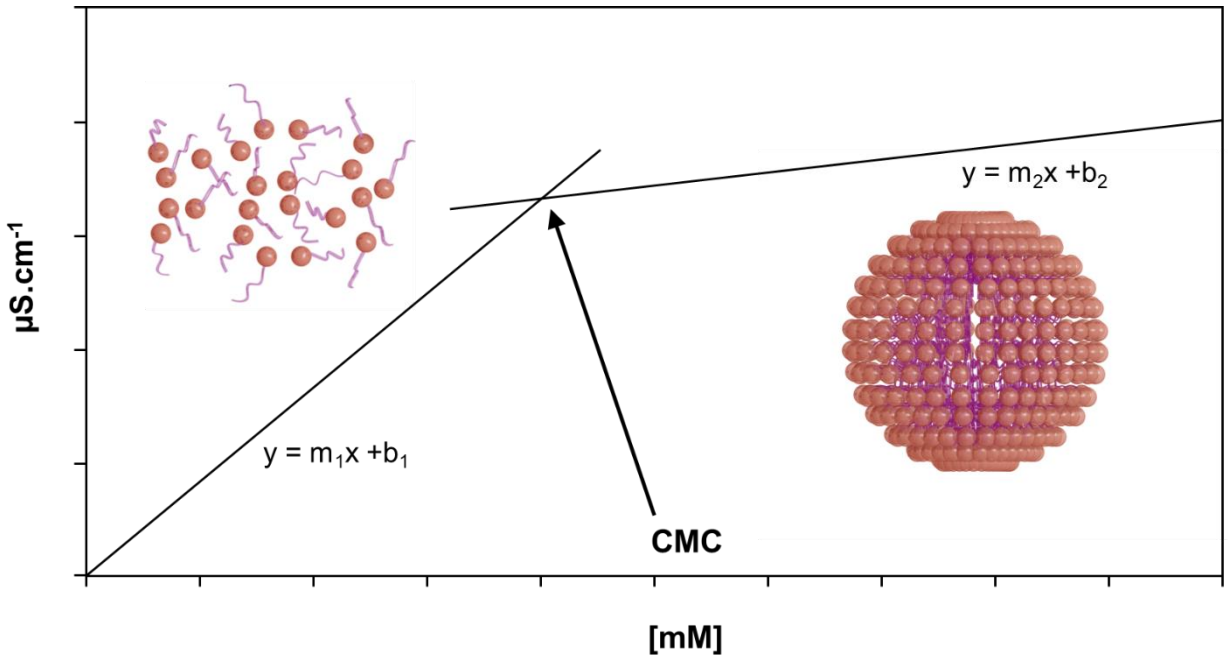

Figure 33. Typical conductivity vs. concentration plot of a linear amphiphile.

2.6. Determination of the Free Energies of Micellization ($\Delta G°_M$)

The plots of conductivity vs. concentration are also useful in calculating the Gibbs free energies of micellization ($\Delta G°_M$). The slopes of the plots can be plugged in the equation proposed by Zana [102] to find the free energy values.

$$\Delta G_M^{\circ} = RT\left(\frac{1}{j} + \beta\frac{i}{j}\left|\frac{Z_S}{Z_C}\right|\right)\ln cmc + RT\left(\frac{i}{j}\left|\frac{Z_S}{Z_C}\right|\beta\ln\frac{i}{j}\left|\frac{Z_S}{Z_C}\right| - \frac{\ln j}{j}\right)$$

Where *R* is the gas constant, *T* is the temperature of the solution in Kelvin, *i* and *j* is the number of charged head groups and hydrophobic tails of the surfactant respectively, Z_s is the valency of a charged group, Z_c is the valency of a counterion, $\beta = (m_1 - m_2) / m_1$ where m_1 is the slope of conductivity versus concentration of the pre-micellization region, m_2 is the slope of conductivity versus concentration of the post-micellization region, and cmc is the critical micelle concentration.

3. Results and Discussion

3.1. Synthesis and Characterization of Gemini Amphiphiles

The synthesized gemini amphiphiles are tetracationic halide salts that precipitated as yellow solids upon their formation in polar aprotic solvents. This allowed the target products to be recovered and purified easily by vacuum filtration and subsequent triturated with organic solvents. The title compounds were obtained in good yield without further purification required. The first step of the gemini amphiphiles' synthetic routes: the mono-alkylation of 4,4'-Dipyridyl by 11-bromo-1-undecene has a yield of 62%. The second alkylation in the synthetic routes has a yield of 71% for the $\mathbf{5}^{4+}$, 79% for the $\mathbf{7}^{4+}$, and 62% for the $\mathbf{9}^{4+}$.

The structures of mono-undecylated bipyridine and three synthetic gemini amphiphiles were characterized and confirmed by multiple experiments including ^{1}H NMR, ^{13}C NMR, 2D ^{1}H-^{1}H COSY NMR, and 2D ^{1}H-^{13}C HSQC NMR.

3.1.1. Characterization of mono-undecylated bipyridine $\mathbf{2}^{1+}$: The integration, pattern, and position of the peaks in the ^{1}H-NMR spectrum of the $\mathbf{2}^{1+}$ (**Figure 34**) helped to elucidate the structure of the compound. Four distinct peaks in the region of 7.89 – 9.17 ppm matched with four groups of protons on the aromatic rings of the compounds. The signals for protons of -CH=CH$_2$-

and (-CH_2-N^+-) were found between 4.73 to 5.83 ppm. The signals for protons of the methylene groups (-CH_2-) in the tail also appeared in the upfield region 1.32 – 2.02 ppm. The correlation between neighboring protons in the COSY NMR spectrum (**Figure S4**), the number of carbon signals in ^{13}C-NMR (**Figure S5**), as well as the correlation between proton-carbon in HSQC NMR (**Figure S6**) supported the validity of the compound.

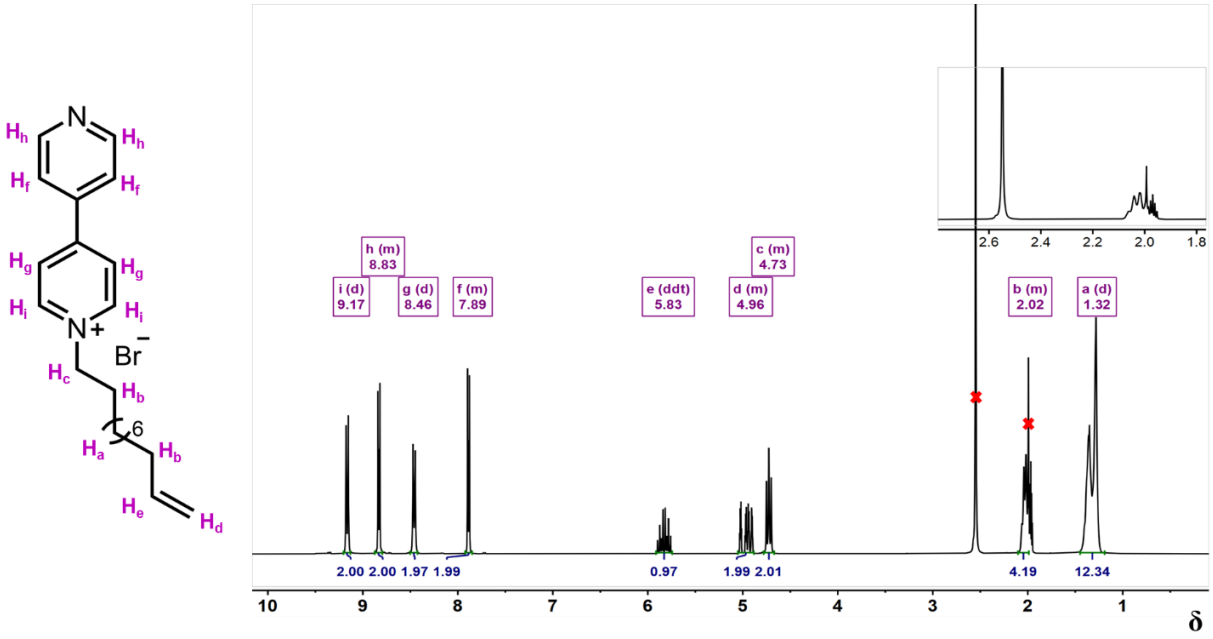

Figure 34. ^{1}H-NMR of mono-undecylated bipyridine $\mathbf{2^{1+}}$ prepared in CD_3CN solvent at 25°C.

3.1.2. Characterization of 5-carbon-akyl-bridged bis-bipyridinium-based gemini amphiphile $\mathbf{5^{4+}}$: NMR spectra including ^{1}H-NMR, 2D COSY NMR, ^{13}C NMR, and 2D HSQC NMR all displayed clean and sharp signals belonging only to the desired compound. In ^{1}H-NMR spectrum (**Figure 35**), signals for the aromatic protons appeared as two peaks very downfield from 8.4 – 9.2 ppm. Protons attached to carbons in the double bond (-CH_2=CH-) and protons on carbons directly bonded with nitrogen atoms have peaks showed in the region 4.5 – 6 ppm. Protons on carbons in single C-C bonds have upfield signals in 1 – 2.4 ppm. The sum of all integrated values was equal to 68 which is the number of protons of the compound, further confirming its structure.

In the COSY NMR spectrum (**Figure 36**), the correlation of proton-proton matched with what expected for the structure of the desired compound. It was observed that $H_{\alpha,\ \alpha'}$ correlated with $H_{\beta,\ \beta'}$, H_c correlated with H_d and H_f, $H_{g,\ g'}$ correlated with $H_{e,\ e'}$, H_i, and H_h. ^{13}C NMR spectrum (**Figure S7**) and 2D HSQC NMR spectrum (**Figure S8**) are another evidence supporting the achievement of the target compound.

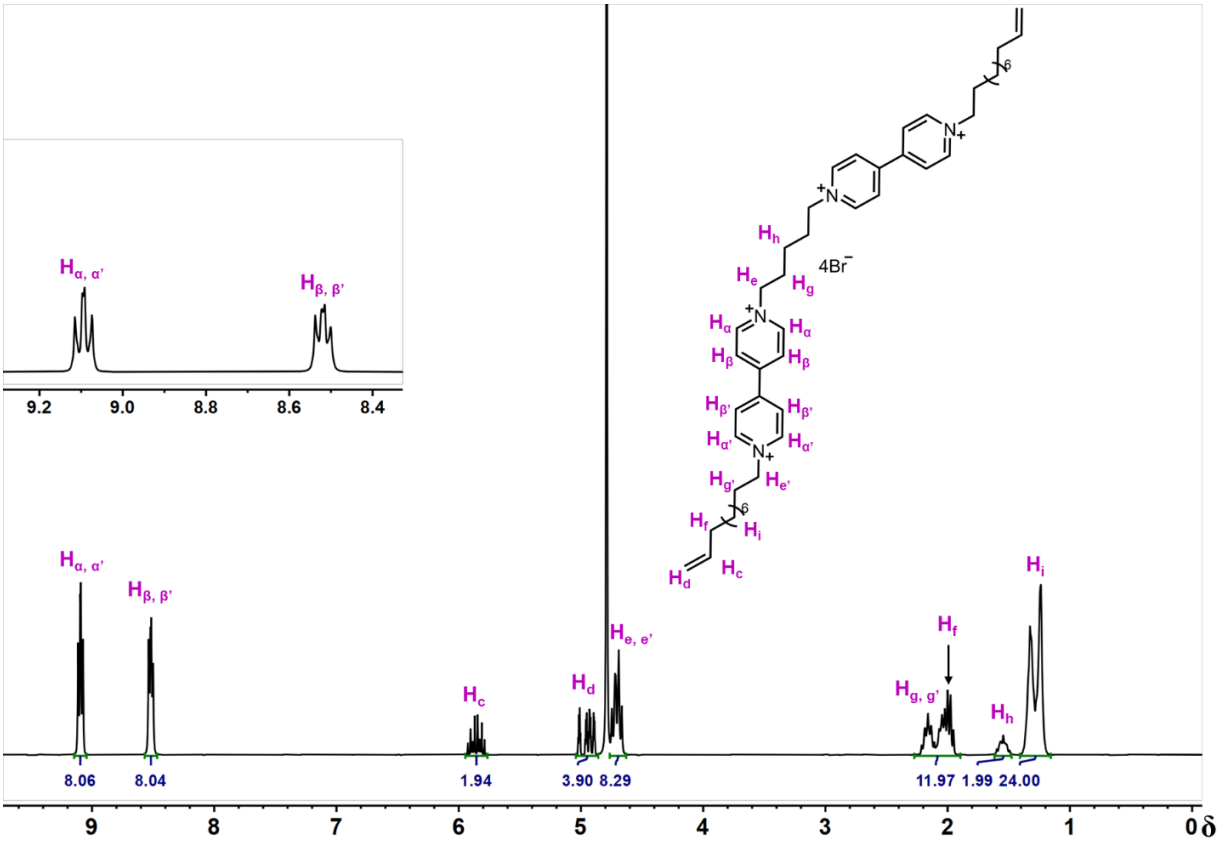

Figure 35. ^{1}H-NMR spectrum of the 5-carbon-akyl-bridged bis-bipyridinium-based gemini amphiphile $\mathbf{5}^{4+}$ (D_2O, 25°C).

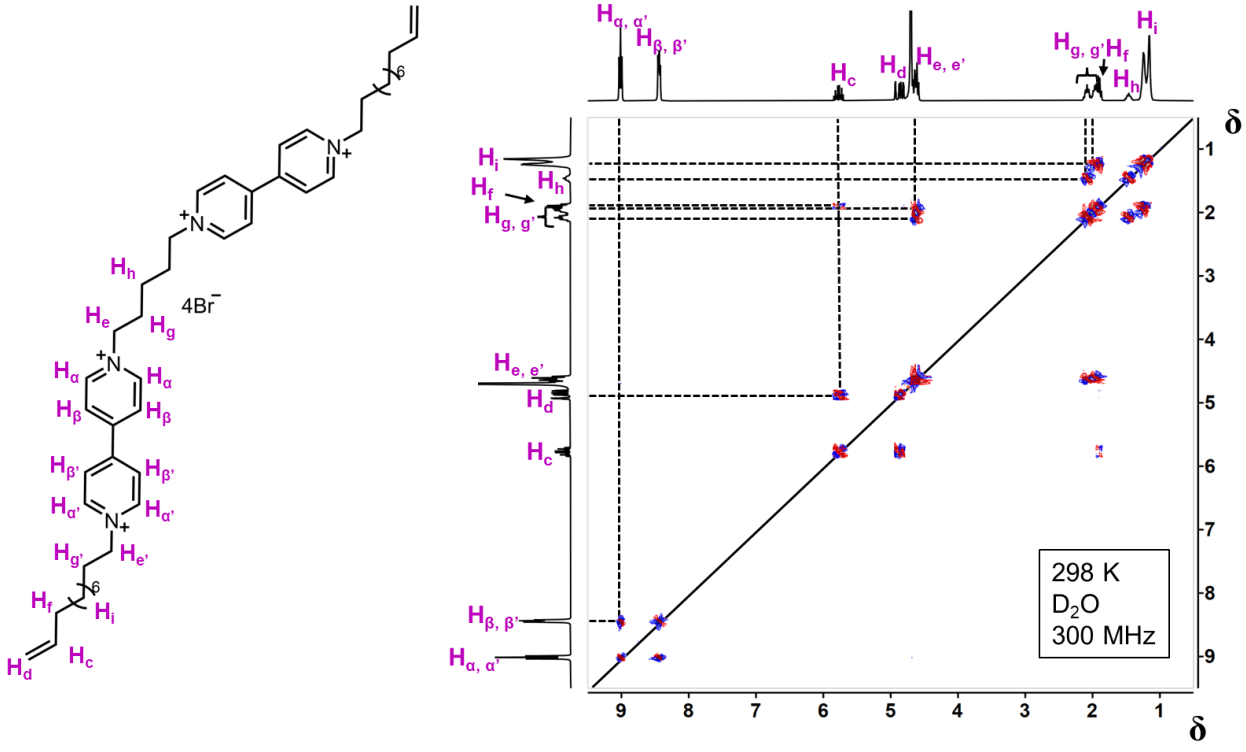

Figure 36. 2D COSY NMR of the 5-carbon-akyl-bridged bis-bipyridinium-based gemini amphiphile $\mathbf{5}^{4+}$ (D_2O, 25°C).

3.1.3. Characterization of 7-carbon-akyl-bridged bis-bipyridinium-based gemini amphiphile $\mathbf{7}^{4+}$: The structure of $\mathbf{7}^{4+}$ was also verified to be correct by NMR experiments. As structure of $\mathbf{7}^{4+}$ and $\mathbf{5}^{4+}$ only differ in the number of carbons of the alkyl bridges, their NMR spectra are very similar. Thus, protons signals were observed in the ^{1}H-NMR spectrum of the $\mathbf{7}^{4+}$ compound (**Figure 37**): aromatic protons ($H_{\alpha,\alpha'}$, $H_{\beta,\beta'}$) in downfield region 8.4 – 9.2 ppm; vinylic protons (H_c, H_d) and protons on carbons attached directly to the nitrogen atoms ($H_{e,e'}$) in middle region 4.6 – 5.2 ppm; and the protons of methylene groups (H_g, H_f, H_h, H_i) in the upfield region of 1 – 2.2 ppm. However, the total of integrated values was 72 which suggested that the structure has 4 more hydrogens from its two extra methylene groups in the spacer. The structure of $\mathbf{7}^{4+}$ were further elucidated with 2D COSY NMR (**Figure S9**), ^{13}C NMR (**Figure S10**), and 2D HSQC NMR (**Figure S11**).

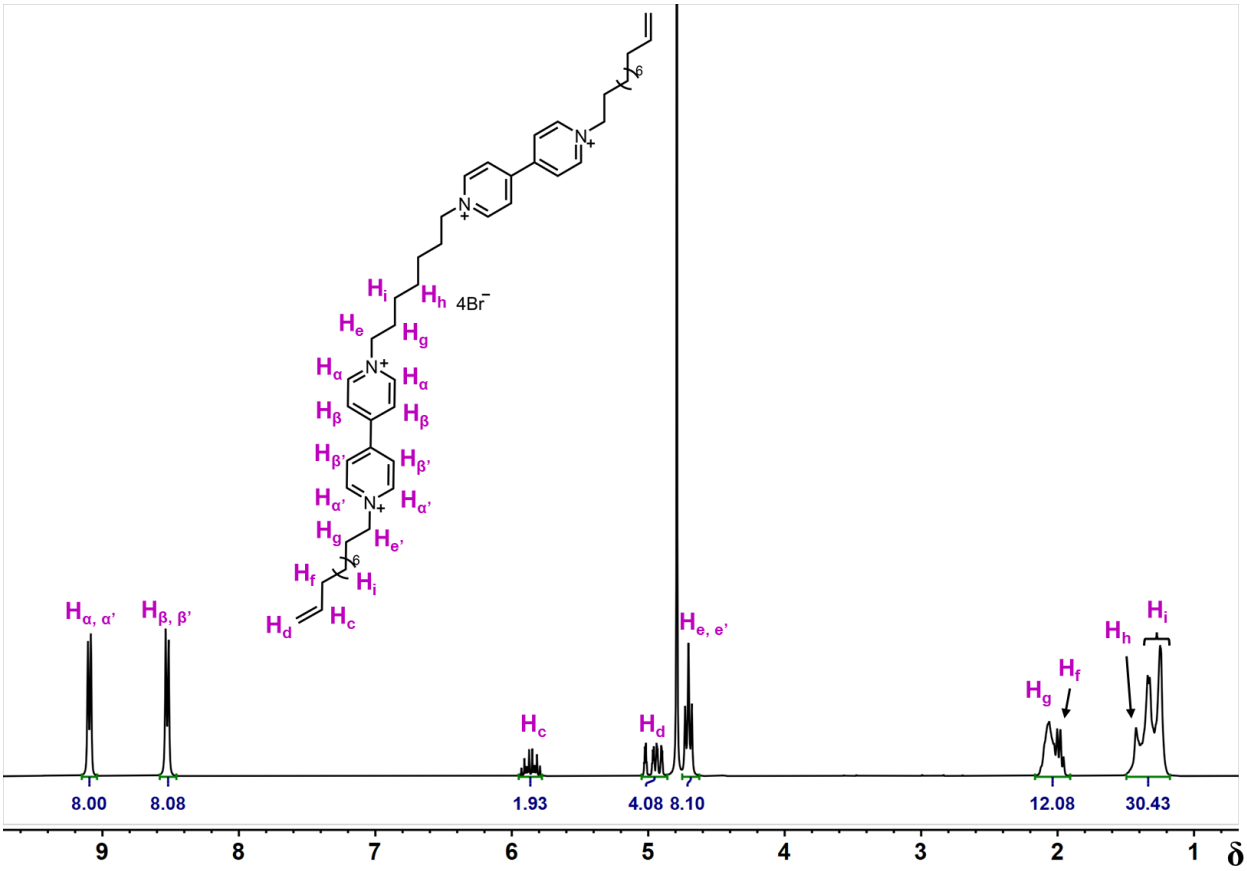

Figure 37. ^{1}H-NMR spectrum of the 7-carbon-akyl-bridged bis-bipyridinium-based gemini amphiphile $\mathbf{7}^{4+}$ (D_2O, 25°C).

3.1.4. Characterization of 9-carbon-akyl-bridged bis-bipyridinium-based gemini amphiphile $\mathbf{9}^{4+}$: Similar proton signals were observed in the ^{1}H NMR spectrum (**Figure 38**) for $\mathbf{9}^{4+}$ like the other two gemini amphiphiles. The total integrated value of 76 suggested that the synthesis of the $\mathbf{9}^{4+}$ was succesfull. Additionally, the results of 2D COSY NMR (**Figure S12**), ^{13}C NMR (**Figure S13**), and 2D HSQC NMR (**Figure S14**) helped to validate the structure of the $\mathbf{9}^{4+}$ amphiphiles.

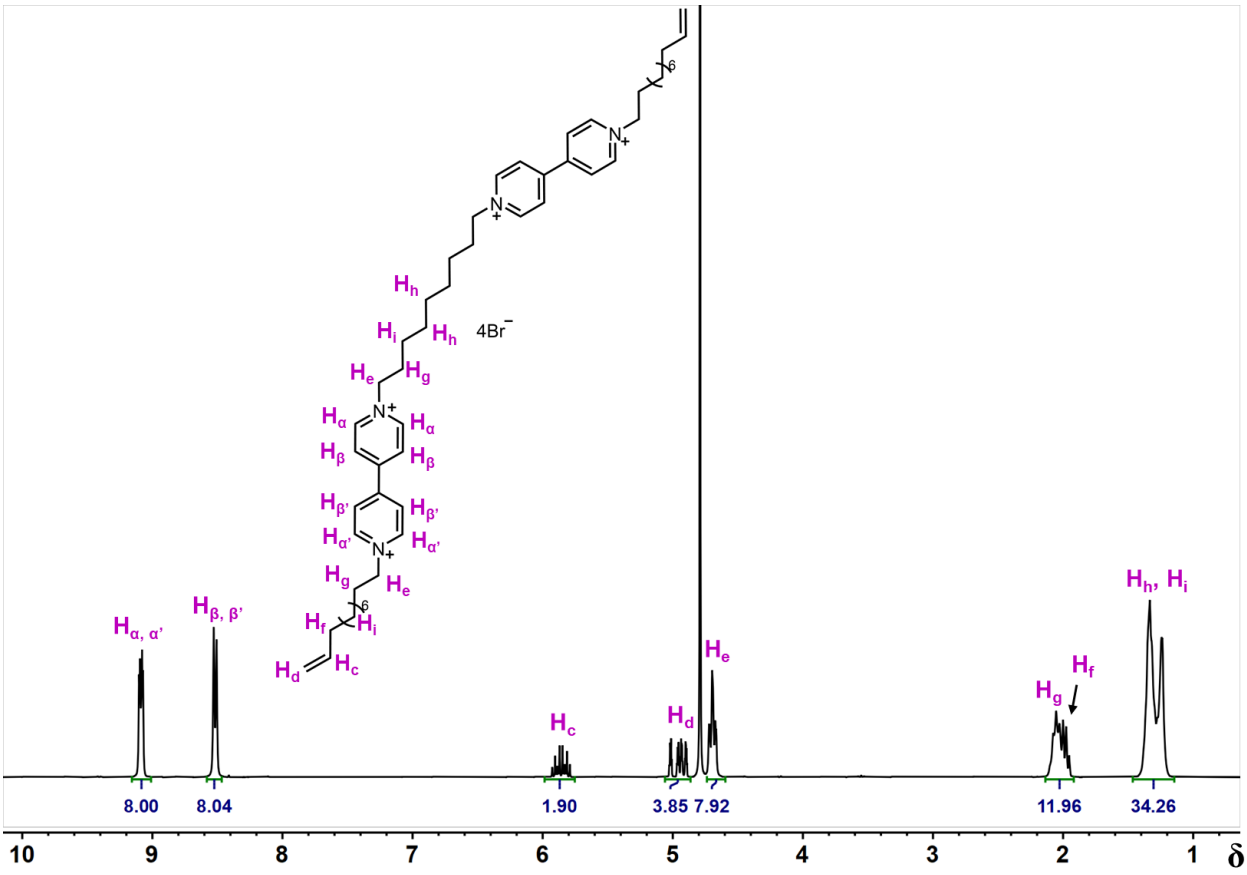

Figure 38. ^{1}H-NMR spectrum of the 9-carbon-akyl-bridged bis-bipyridinium-based gemini amphiphile $\mathbf{9}^{4+}$ (D_2O, 25°C).

3.2. Formation of π-π Donor-Acceptor Charge-Transfer Complexes

When 1 equivalent and 2 equivalents of melatonin was mixed with aqueous solutions of the alkyl-bridged bis-bipyridinium gemini amphiphiles, the color of the solution changed from clear to orange, and dark orange respectively (**Figure 39**). The change in color was the first sign that the CT interaction between the π-electron deficient bipyridinium units and the π-electron rich melatonin had occurred. As explained by molecular orbital theory, when a CT complex begins to form, it absorbs energy in the visible region and undergoes an electronic transition. The electrons, in this case, are transferred from the highest occupied molecular orbital (HOMO) of the electron-donor to the lowest unoccupied molecular orbital (LUMO) of the electron acceptor which

generates a new absorption band.[103] The absorbance of the complexes were probed by UV-Vis spectrophotometry as showed in **Figure 40**. UV-Vis absorption measurements revealed the presence of CT absorption bands (λ_{max} = 447 - 457 nm) in 5mM mixed solutions of amphiphiles and melatonin, an indicator that face-to-face donor acceptor π-stacking has occurred. The CT absorbances with 2 equivalents of melatonin were approximately double the absorbances of the samples with 1 equivalent of melatonin, supporting the two distinct processes of template binding.

Figure 39. The visible color change is due to charge-transfer interactions. Vials containing 5 mM $\mathbf{5}^{4+}$ (A), 5mM $\mathbf{5}^{4+}$ + 1eq Mel (B), 5 mM $\mathbf{5}^{4+}$ + 2eq Mel (C), 5 mM $\mathbf{7}^{4+}$ (D), 5mM $\mathbf{7}^{4+}$ + 1eq Mel (E), and 5 mM $\mathbf{7}^{4+}$ + 2eq Mel (F), 5 mM $\mathbf{9}^{4+}$ (G), 5 mM $\mathbf{9}^{4+}$ + 1eq Mel (H), and 5 mM $\mathbf{9}^{4+}$ + 2eq Mel (I).

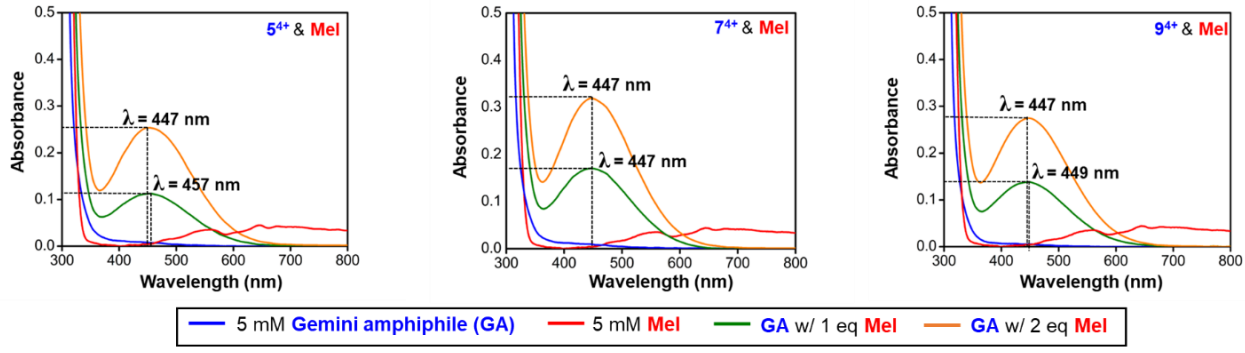

Figure 40. UV-Vis spectra of 5 mM aqueous solution of alkyl-bridged bis-bipyridinium-based gemini amphiphiles with 0, 1, and 2 equivalents of melatonin A) the $\mathbf{5}^{4+}$ amphiphile B) the $\mathbf{7}^{4+}$ amphiphile and C) the $\mathbf{9}^{4+}$ amphiphile.

^{1}H NMR spectra revealed shifts in the resonance signals for the aromatic protons and α-protons adjacent to the nitrogen atoms of the alkyl-bridged gemini amphiphiles, as well as the aromatic protons of melatonin when the two compounds were combined in 1:1 (process I) and 2:1 (process II) molar ratios of donor to acceptor in D_2O at 298 K. When 1 equivalent of melatonin was introduced into the aqueous solution of the gemini amphiphiles, the protons' signals in and near the aromatic region of both the amphiphiles and melatonin shifted upfield caused by mutual shielding when the bipyridinium units interacted with melatonin through π-π stacking, [C – H ⋯ π], and [C – H ⋯ O] interactions and by symmetry breaking. For all three gemini amphiphiles, the Δδ changes in the proton signals of the bipyridinium units in process I and II have a small difference (**Table 1**), revealing that the gemini amphiphiles adopt a linear conformation while under the hydrophobic effect. Previous literature reported that if the surfactants adopt a horseshoe-shaped conformation, the Δδ of proton signals in 1:1 solutions are more larger and negative than that in the 1:2 solutions.[93, 104] The stacked NMR spectra of the $\mathbf{5^{4+}}$ and $\mathbf{7^{4+}}$ (**Figure 41**, and **Figure 42**) showed that when 1 and 2 equivalents of melatonin was added, the peaks for $H_{\alpha,\,\alpha'}$, $H_{\beta,\,\beta'}$, and $H_{e,\,e'}$ split into two distinct peaks in which the change in chemical shifts for $H_{\alpha'}$, $H_{\beta'}$, and $H_{e'}$ are much larger than those of H_{α}, H_{β}, and H_{e} (**Table 1**) implying that when the melatonin molecules were bound between two bipyridinium units, they sat nearer to the hydrophobic tails of the amphiphiles. Meanwhile, in the stacked NMR spectra of the $\mathbf{9^{4+}}$ amphiphile (**Figure 43**), the signals of $H_{\alpha,\,\alpha'}$, $H_{\beta,\,\beta'}$, and $H_{e,\,e'}$ were not split which meant the melatonin might reside perfectly in the center of two bipyridinium units.

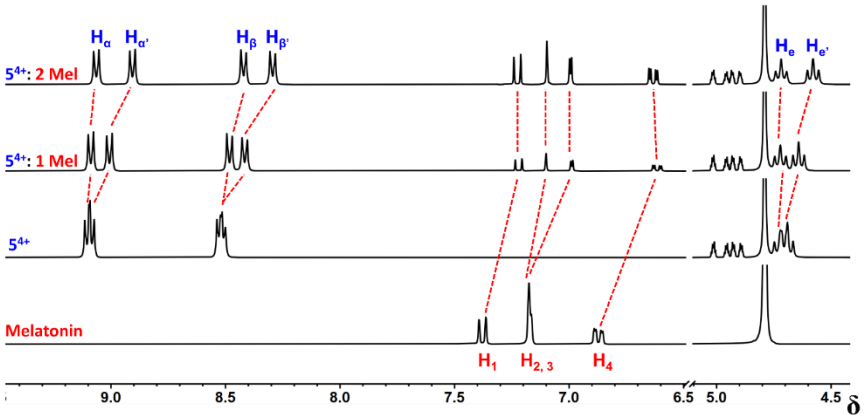

Figure 41. Stacked NMR spectra of $\mathbf{5}^{4+}$. Four different ^{1}H-NMR spectra (D_2O, 25°C) including the spectrum of melatonin solution, 5 mM $\mathbf{5}^{4+}$, 5 mM $\mathbf{5}^{4+}$ with 1 equivalent of melatonin, and 5 mM $\mathbf{5}^{4+}$ with 2 equivalents of melatonin were stacked together.

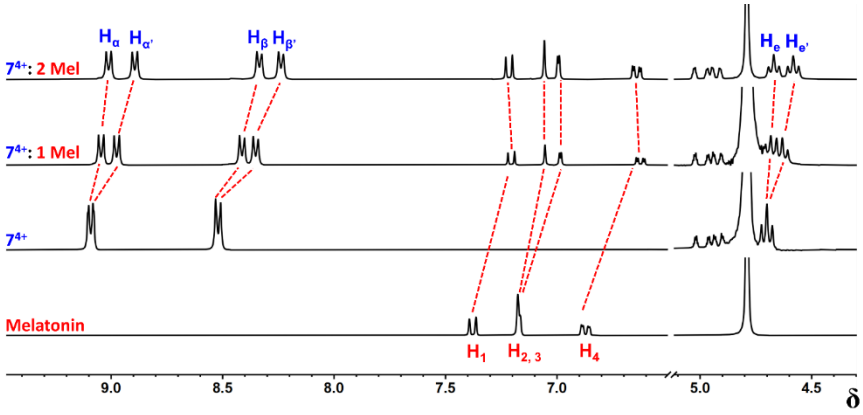

Figure 42. Stacked NMR spectra of $\mathbf{7}^{4+}$. Four different ^{1}H-NMR spectra (D_2O, 25°C) including the spectrum of melatonin solution, 5 mM $\mathbf{7}^{4+}$, 5 mM $\mathbf{7}^{4+}$ with 1 equivalent of melatonin, and 5 mM $\mathbf{7}^{4+}$ with 2 equivalents of melatonin were stacked together.

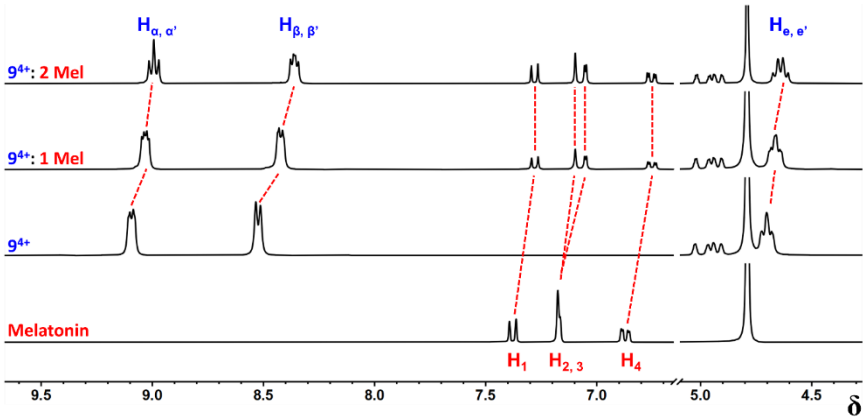

Figure 43. Stacked NMR spectra of $\mathbf{9}^{4+}$. Four different ^{1}H-NMR spectra (D_2O, 25°C) including the spectrum of melatonin solution, 5 mM $\mathbf{9}^{4+}$, 5 mM $\mathbf{9}^{4+}$ with 1 equivalent of melatonin, and 5 mM $\mathbf{9}^{4+}$ with 2 equivalents of melatonin were stacked together.

Table 1. Changes in chemical shift of proton signals of the $\mathbf{5^{4+}}$, $\mathbf{7^{4+}}$, and $\mathbf{9^{4+}}$.

	5 mM $\mathbf{5^{4+}}$ + 1eq Mel	5 mM $\mathbf{5^{4+}}$ + 2eq Mel	5 mM $\mathbf{7^{4+}}$ + 1eq Mel	5 mM $\mathbf{7^{4+}}$ + 2eq Mel	5 mM $\mathbf{9^{4+}}$ + 1eq Mel	5 mM $\mathbf{9^{4+}}$ + 2eq Mel
$\mathbf{\Delta\delta\ H_{\alpha}}^{a}$	−0.017	−0.024	−0.035	−0.045	−0.065	−0.037
$\mathbf{\Delta\delta\ H_{\alpha'}}^{a}$	−0.076	−0.101	−0.114	−0.081	−0.065	−0.037
$\mathbf{\Delta\delta\ H_{\beta}}^{a}$	−0.046	−0.061	−0.107	−0.078	−0.100	−0.061
$\mathbf{\Delta\delta\ H_{\beta'}}^{a}$	−0.094	−0.122	−0.170	−0.110	−0.100	−0.061
$\mathbf{\Delta\delta\ H_{e}}^{a}$	−0.001	−0.004	−0.024	−0.011	−0.042	−0.022
$\mathbf{\Delta\delta\ H_{e'}}^{a}$	−0.049	−0.063	−0.075	−0.050	−0.042	−0.022
$\mathbf{\Delta\delta\ H_{1}}^{b}$	−0.161	0.007	−0.175	0.009	−0.097	0
$\mathbf{\Delta\delta\ H_{2}}^{b}$	−0.074	−0.004	−0.121	0.004	−0.078	0
$\mathbf{\Delta\delta\ H_{3}}^{b}$	−0.178	0.007	−0.180	0.009	−0.116	0
$\mathbf{\Delta\delta\ H_{4}}^{b}$	−0.256	0.017	−0.248	0.019	−0.121	0.002

[a]Obtained by calculating the change of chemical shifts of proton signals in ^{1}H-NMR spectra of the gemini amphiphiles after each equivalent of melatonin added.
[b]Obtained by calculating the change of chemical shifts of the proton signals in ^{1}H-NMR spectra of melatonin after each equivalent of melatonin added.

The binding of melatonin to the bis-bipyridinium units of the gemini amphiphiles were also attested by NMR spectra collected from Rotating Frame Overhauser Enhancement Spectroscopy (ROESY) and Diffusion-Order Spectroscopy (DOSY). ROESY spectra of the mixed solution of the gemini amphiphiles and 2 equivalents of melatonin **(Figure 44)** revealed the presence of through-space correlation among aromatic protons of the bis-bipyridinium head groups of the amphiphiles and the melatonin. Furthermore, DOSY displayed the proton signals for the melatonin co-diffused at the same translational self-diffusion coefficient (D_0) with those of the surfactant

hosts (**Figure S15**, **S16**, and **S17**). The values of the self-diffusion coefficients for Mel-5^{4+}, Mel-7^{4+}, and Mel-9^{4+} complexes are 2.30E-10 m^2/s, 2.16E-10 m^2/s, and 2.24E-10 m^2/s respectfully. The hydrodynamic diameter values of the donor-acceptor CT complexes calculated with Stokes-Einstein equation were displayed in **Table 2**.

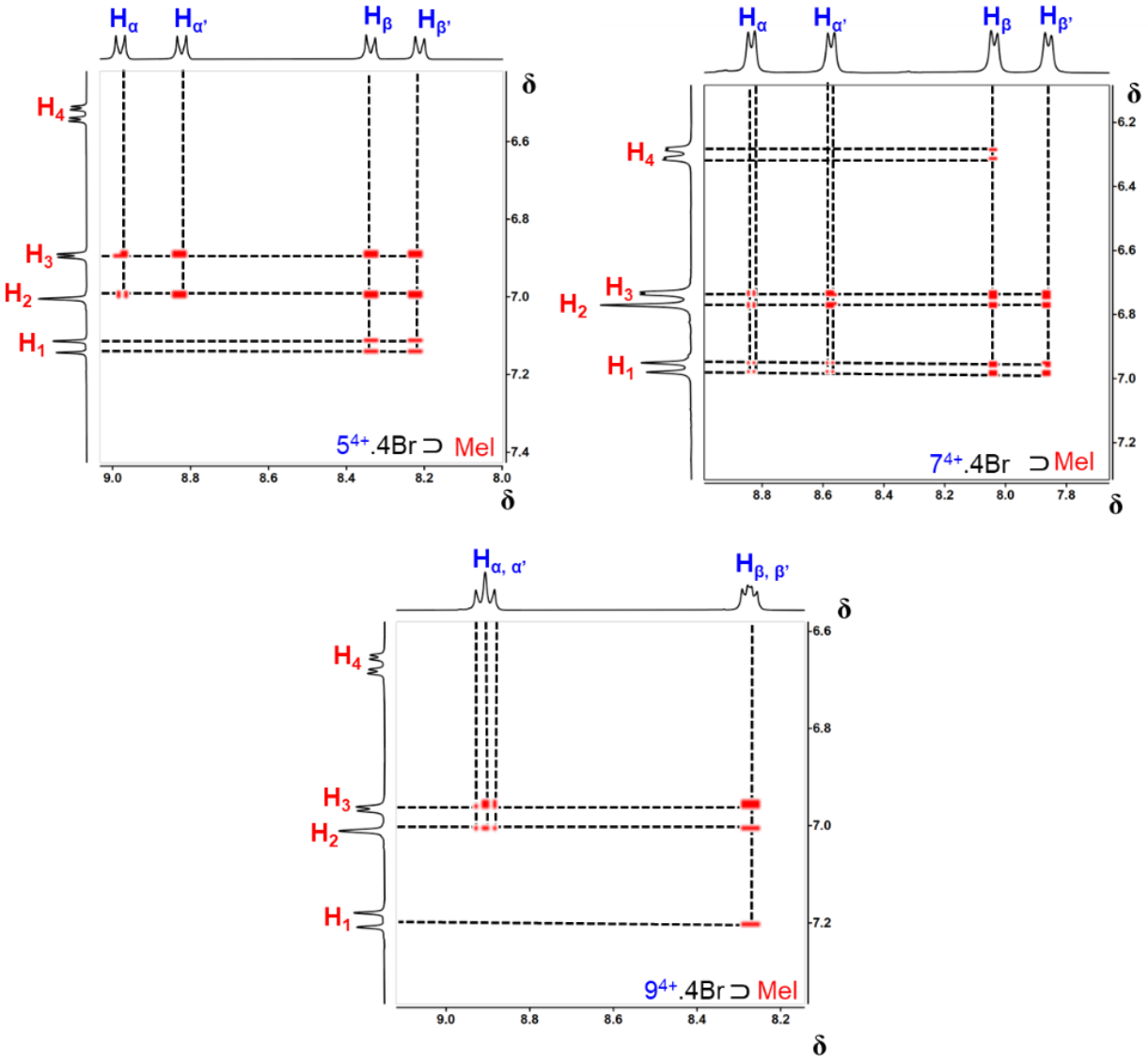

Figure 44. ROESY spectra of a mixed solution of $\mathbf{5^{4+}}$ and melatonin, mixed solution of $\mathbf{7^{4+}}$ and melatonin, and mixed solution of $\mathbf{9^{4+}}$ and melatonin.

Table 2. Diffusion coefficients and hydrodynamic diameters of the gemini amphiphiles and the Mel-Gemini amphiphiles complexes.

Solution	Diffusion coefficient D_0 (m^2/ cm)	Hydrodynamic diameter D_H (nm)
5 mM 5^{4+}	2.44E-10	1.79
5 mM 5^{4+} + 2eq. Mel	2.30E-10	1.89
5 mM 7^{4+}	2.33E-10	1.87
5 mM 7^{4+} + 2eq. Mel	2.16E-10	2.02
5 mM 9^{4+}	2.44E-10	1.79
5 mM 9^{4+} + 2eq. Mel	2.24E-10	1.94

3.3. Template effect by Melatonin and Free Energies of Micellization revealed by Conductivity Measurements.

In addition to the CMC values, conductivity versus concentration plots also revealed the existence of premicellar aggregation for the three alkyl-bridge bis-bipyridinium-based gemini amphiphiles in both untemplated and templated micellar assemblies (**Figure 45**, **Figure 46**, & **Figure 47**). The pre-CMC is the concentration where pre-micellular aggregates begin to form. The plots also revealed the effect of melatonin on the self-assembly process of the alkyl-bridged amphiphiles. As a result of the addition of melatonin, which reduced the repulsion between positively charged bis-bipyridinium groups, the assembly of the aggregates and micelles occurred at lower amphiphile concentrations as indicated in **Table 3**.

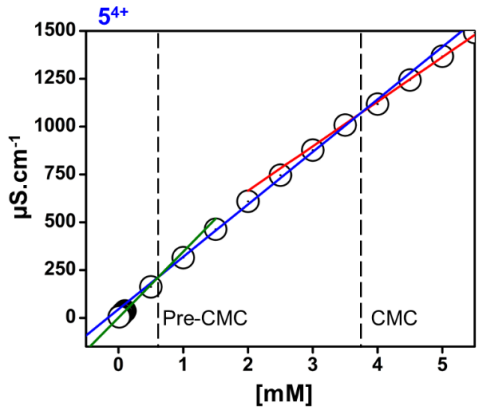

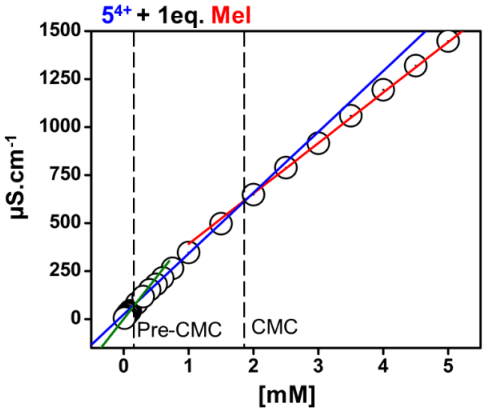

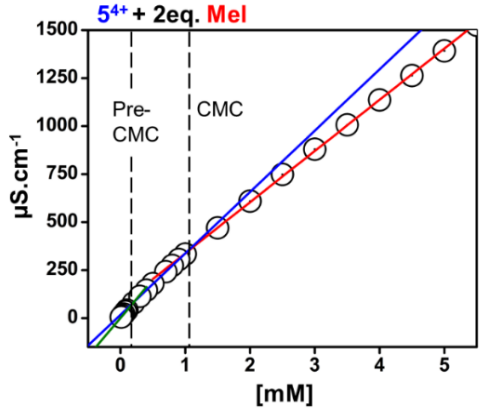

Figure 45. Conductivity vs. concentration of aqueous solution of $\mathbf{5}^{4+}$ with and without the addition of melatonin

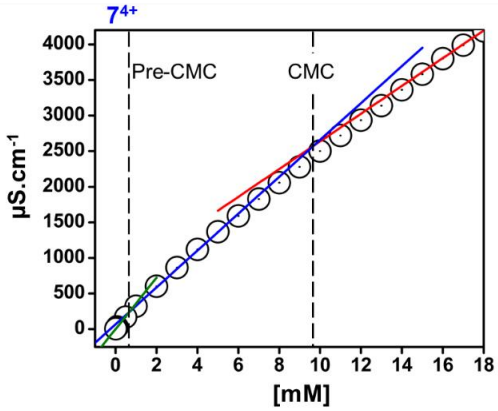

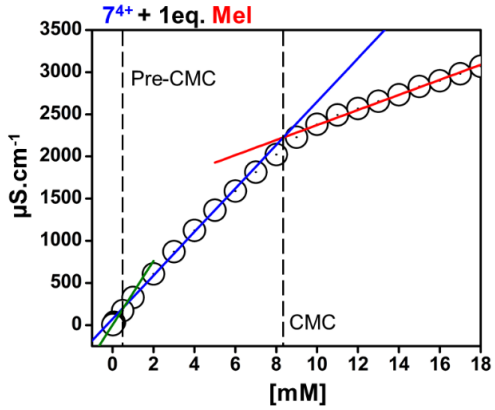

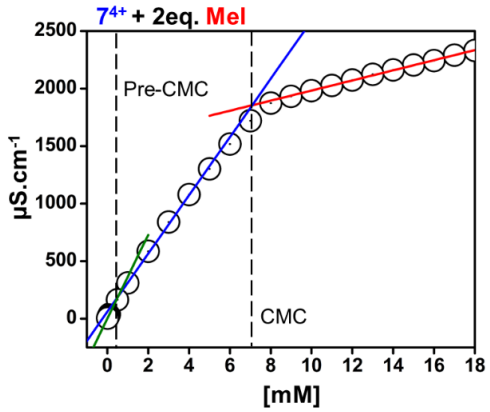

Figure 46. Conductivity vs. concentration of aqueous solution of $\mathbf{7}^{4+}$ with and without the addition of melatonin

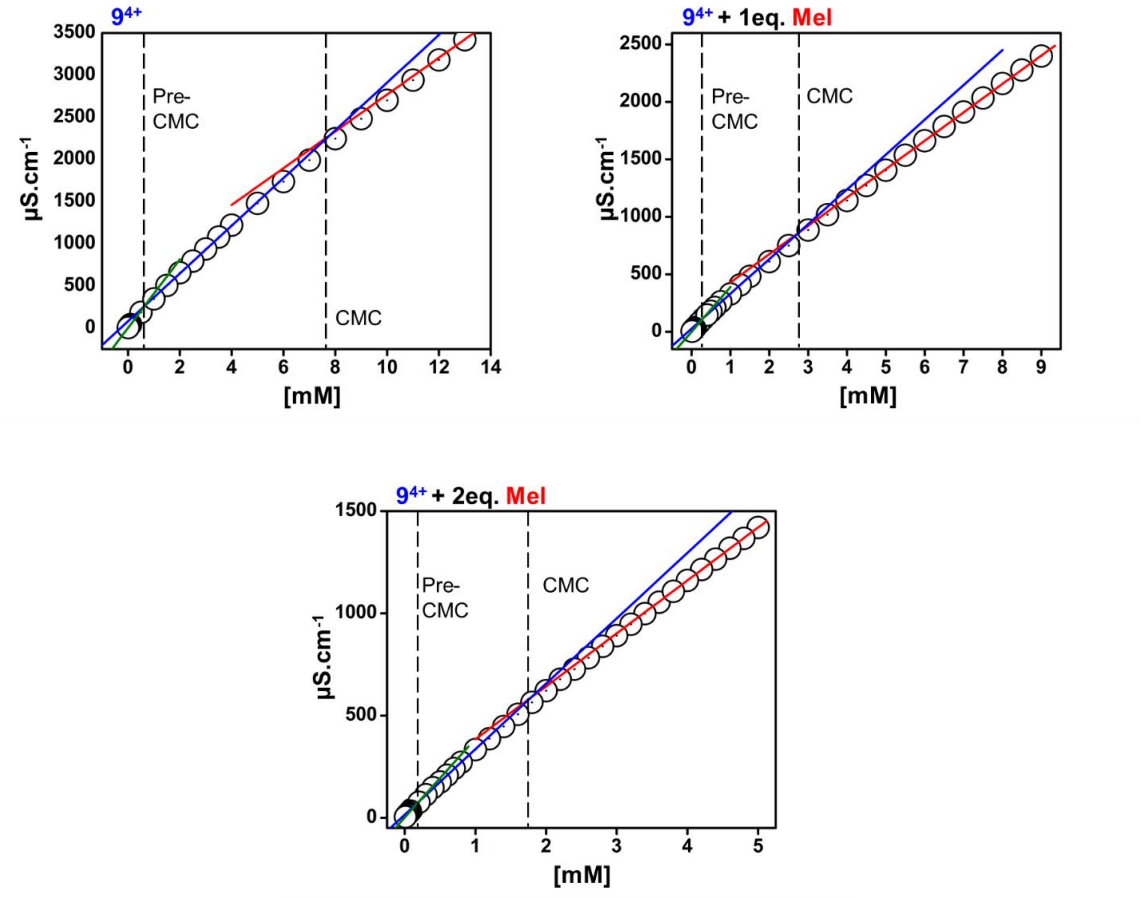

Figure 47. Conductivity vs. concentration of aqueous solution of $\mathbf{9}^{4+}$ with and without the addition of melatonin.

The pre-CMC and CMC values dropped dramatically with the addition of 1 equivalents of melatonin, and they further decreased when another equivalent of melatonin was added (**Figure 48**). With 2 equivalents of melatonin, pre-CMC decreased about 66% for the $\mathbf{5}^{4+}$, 16% for the $\mathbf{7}^{4+}$, and 67% for the $\mathbf{9}^{4+}$. Similarly, CMC dropped about 71% for $\mathbf{5}^{4+}$, 28% for $\mathbf{7}^{4+}$, and 77% for $\mathbf{9}^{4+}$. In most scenarios investigated, the decrease in slope values at the inflection points are small suggesting a gradual increase in micellar size. However, in the presence of template, the slope of conductivity vs. concentration of $\mathbf{7}^{+}$ dropped abruptly when the concentration reached the CMC. This is an indication that much larger aggregates are being templated by the addition of melatonin. The conductivity method also demonstrated a declining trend in the $\Delta G°_{M}$ of the pre-micellular

aggregation and micellization processes with the addition of melatonin (**Table 3**). However, 2 equivalents of melatonin showed little to no effect on the $\Delta G°_{M}$ for the assembly that occurred at pre-CMC concentrations, while a profound effect was observed for process at the CMC (**Figure 49**). This phenomenon was evidence that the lower critical concentration was in fact a pre-CMC process since the pre-micellular aggregates were too small to benefit from templating by melatonin, while the larger micellar aggregates can take up two equivalents of the template per surfactant molecule.

Table 3. Pre-CMC and CMC values of the $\mathbf{5}^{4+}$, $\mathbf{7}^{4+}$, and $\mathbf{9}^{4+}$ with and without the effect of melatonin and their corresponding free energies of pre-micellular aggegration ($\Delta G_{M}^{\circ}{}_{\text{Pre-CMC}}$) and micellization ($\Delta G_{M}^{\circ}{}_{\text{CMC}}$)

Solution	Pre-CMC (mM)	$\Delta G_{M}^{\circ}{}_{\text{Pre-CMC}}$ (kcal.mol^{-1})	CMC (mM)	$\Delta G_{M}^{\circ}{}_{\text{CMC}}$ (kcal.mol^{-1})
$\mathbf{5}^{4+}$	0.61 ± 0.01	−4.02 ± 0.21	3.64 ± 0.22	−2.74 ± 0.13
$\mathbf{5}^{4+}$ + 1 eq. **Mel**	0.21 ± 0.01	−5.14 ± 0.13	1.83 ± 0.06	−3.18 ± 0.08
$\mathbf{5}^{4+}$ + 2 eq. **Mel**	0.21 ± 0.01	−4.60 ± 0.09	1.05 ± 0.05	−3.47 ± 0.17
$\mathbf{7}^{4+}$	0.64 ± 0.01	−4.58 ± 0.21	9.85 ± 0.17	−2.74 ± 0.10
$\mathbf{7}^{4+}$+ 1 eq. **Mel**	0.59 ± 0.01	−4.96 ± 0.20	8.34 ± 0.03	−4.79 ± 0.08
$\mathbf{7}^{4+}$+ 2 eq. **Mel**	0.54 ± 0.01	−4.90 ± 0.24	7.12 ± 0.02	−5.83 ± 0.05
$\mathbf{9}^{4+}$	0.64 ± 0.01	−4.77 ± 0.12	7.75 ± 0.06	−2.77 ± 0.09
$\mathbf{9}^{4+}$+ 1 eq. **Mel**	0.32 ± 0.01	−4.55 ± 0.11	2.80 ± 0.06	−3.09 ± 0.07
$\mathbf{9}^{4+}$+ 2 eq. **Mel**	0.21 ± 0.01	−4.28 ± 0.14	1.76 ± 0.04	−3.35 ± 0.07

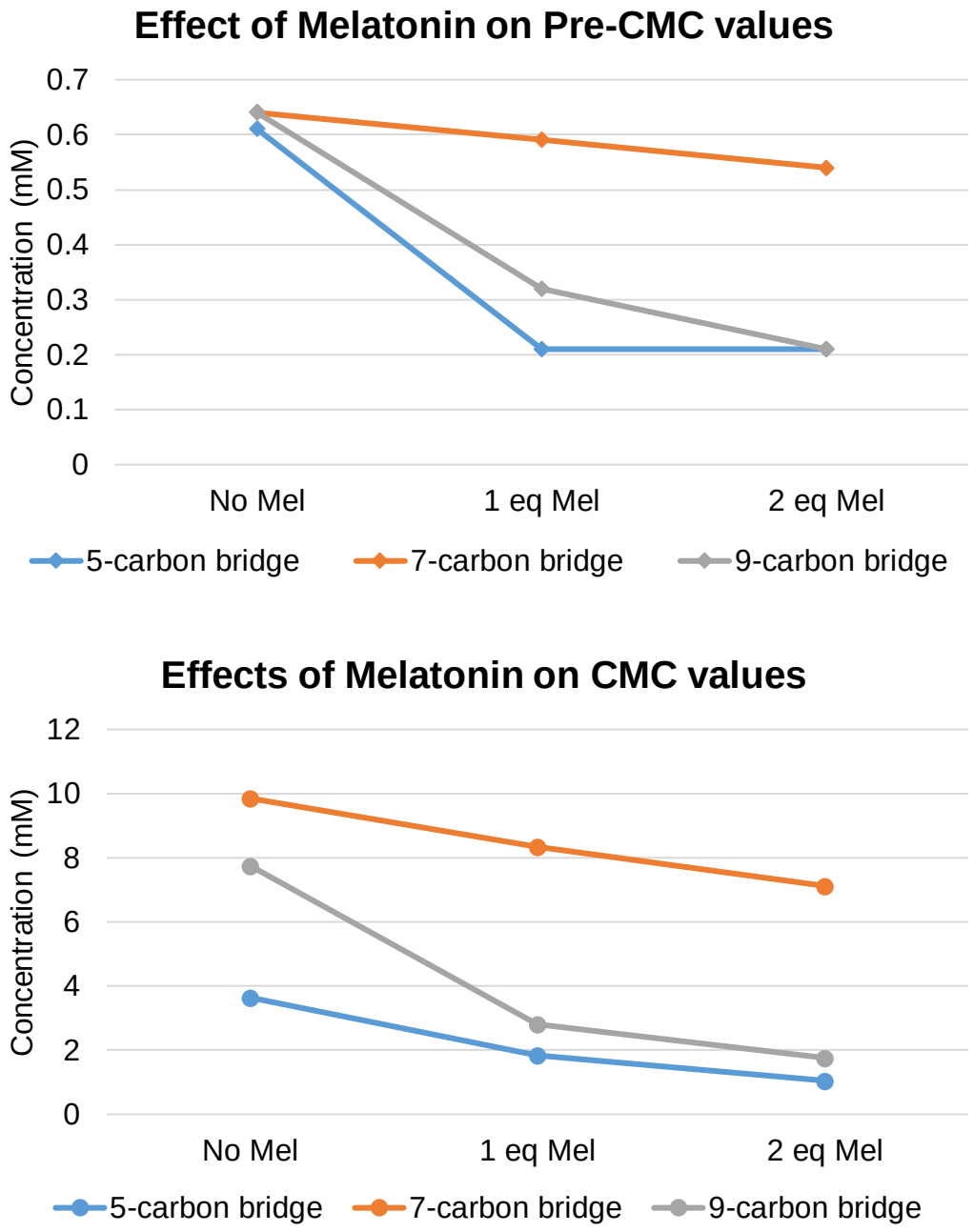

Figure 48. Effects of melatonin on pre-CMC (top) and CMC (bottom) values.

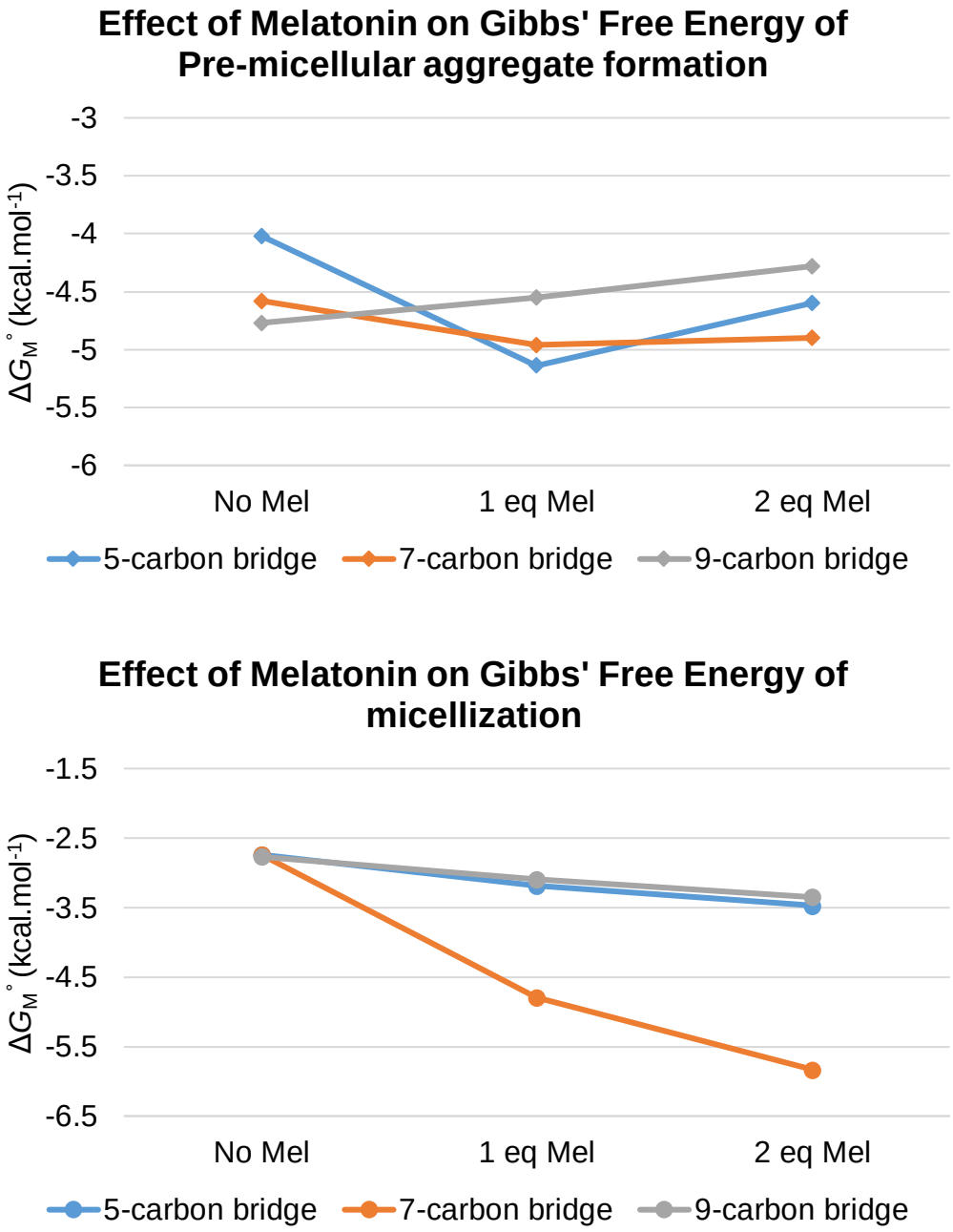

Figure 49. Effects of melatonin on free energies of pre-micellular aggregation (top) and micellization (bottom).

4. Conclusions

Three alkyl-bridged bis-bipyrdinium gemini surfactants $\mathbf{5}^{4+}$, $\mathbf{7}^{4+}$, and $\mathbf{9}^{4+}$ were synthesized through a two-step synthesis comprised of S_N2 reactions in which the first step, the alkylation of 4,4'-dipyridyl with 11-bromoundecene, had a yield of 62% and the second step, the formation of gemini surfactants by joining two linear surfactants with a dibromoalkene, achieving yields of 62-79%. The structures of the synthetic amphiphiles were characterized and confirmed by a variety of NMR experiments including ^{1}H NMR, ^{13} C NMR, 2D-COSY NMR, and 2D-HSQC NMR. The template-directed self-assembly of three alkyl-bridge bis-bipyridinium-based gemini amphiphiles with the π-electron rich neurotransmitter, melatonin were studied by UV-Vis, ^{1}H NMR, 2D DOSY NMR, 2D ROESY NMR, and variable-concentration conductivity. The formation of π-π donor acceptor CT complexes when melatonin was introduced to 5 mM aqueous solution of the gemini amphiphiles were first realized by a color change of the solution from clear to orange to dark orange. This was verified by UV-Vis, stacked ^{1}H NMR spectra, 2D DOSY NMR, and 2D ROESY NMR. A CT absorption band arose in the visible region of the UV-Vis absorption spectra when melatonin was mixed with the amphiphile, confirming the presence of CT interactions between the bipyridinium units and melatonin. 2D ROESY demonstrated the correlation of signals between aromatic protons of both species. Stacked ^{1}H NMR spectra displayed noticeable shifts of signals of the amphiphiles and melatonin, indicating the change in electronic environment caused by the mutual shielding arising from their interactions. Moreover, 2D DOSY NMR confirmed the formation of a Mel-Amphiphile complex as both compounds had signals co-diffusing at the same rate. Lastly, the conductivity vs. concentration plots showed traces of pre-micellar aggregation and demonstrated the effect of the melatonin template towards the self-assembly of these gemini amphiphiles. The addition of melatonin assisted in lowering both the pre-CMC and CMC about

60-70% for the $\mathbf{5}^{4+}$ and the $\mathbf{9}^{+}$ and about 15-30% for the $\mathbf{7}^{4+}$. The effect of melatonin in increasing the size of aggregates is most obvious in the self-assembly of the $\mathbf{7}^{4+}$ as compared to the other gemini amphiphiles. Furthermore, melatonin helped to decrease the free energies of the micellization processes making them more favorable. By examining the self-assembly of three gemini amphiphiles with different spacer' lengths, some structure-property relationships were revealed. The short and long bridges seemed to have much lower critical concentrations and the effect of melatonin in reducing these parameters was more profound but that in increasing the size of aggregates was weak. Meanwhile, the medium bridges tended to have higher critical concentrations and the template had moderate effect on decreasing pre-CMC and CMC, but great impacts on increasing the aggregates' size. More experiments can be performed for these gemini amphiphiles including CV, surface tensiometer, DLS, and Zeta potential measurements to get deeper insights of the structure-property relationships. The knowledge obtained from this work augers well for the future design of gemini amphiphiles for target applications in indole-based molecular detection, for which numerous biological active compounds are potential targets.

REFERENCES

(1) Satinder, A. *Food, Energy, and Water: The Chemistry Connection*, 1st ed.; Elsevier, 2015.

(2) Cecere, D.; Giacomazzi, E.; Ingenito, A. A review on hydrogen industrial aerospace applications. *International Journal of Hydrogen Energy* **2014**, *39*, 10731–10747.

(3) Bahman, Z. *Hydrogen energy challenges and solutions for a cleaner future*, 1st ed.; Springer International Publishing, 2019.

(4) Choubey, G.; Devarajan, Y.; Huang, W.; Yan, L.; Babazadeh, H.; Pandey, K. M. Hydrogen fuel in scramjet engines-A brief review. *International Journal of Hydrogen Energy* **2020**, *45*, 16799–16815.

(5) Bahman, Z. *Physics of cryogenics: an ultra-low temperature phenomena*, 1st ed.; Elsevier, 2017.

(6) Muradov, N. Low to near-zero CO2 production of hydrogen from fossil fuels: Status and perspectives. *International Journal of Hydrogen Energy* **2017**, *42*, 14058–14088.

(7) Zhang, B.; Zhang, S. -X.; Yao, R.; Wu, Y. -H.; Qiu, J. -S. Progress and prospects of hydrogen production: Opportunities and challenges. *Journal of Electronic Science and Technology* **2021**, *19*, 100080.

(8) Fillol, J. L.; Codolà, Z.; Garcia-Bosch, I.; Gómez, L.; Pla, J. J.; Costas, M. Efficient water oxidation catalysts based on readily available iron coordination complexes. *Nat. Chem.* **2011**, *3*, 807–813.

(9) Kondo, M.; Tatewaki, H.; Masaoka, S. Design of molecular water oxidation catalysts with earth-abundant metal ions. *Chem. Soc. Rev.* **2021**, *50*, 6790.

(10) Tsui, E. Y.; Kanady, J. S.; Agapie, T. Synthetic cluster models of biological and heterogenous manganese catalysts for O_2 evolution. *Inorg. Chem.* **2013**, *52*, 13833–13848.

(11) Najafpour, M. M.; Govindjee, G. Oxygen evolving complex in photosystem II: better than excellent. *Dalton Trans*. **2011**, *40*, 9076.

(12) Fillol, J. L.; Costas, M. Water oxidation at base metal molecular catalysts. *Advances in Organometallic Chemistry*. **2019**, *71*, 1–52.

(13) Umena, Y.; Kawakami, K; Shen, J. R.; Kamiya, N. Crystal structure of oxygen-evolving photosystem II at a resolution of 1.9 Å. *Nature* **2011**, *473*, 55–60.

(14) Suga, M.; Akita, F.; Hirata, K.; Ueno, G.; Murakami, H.; Nakajima, Y.; Shimizu, T.; Yamashita, K.; Yamamota, M.; Ago, H.; Shen, J. R. Native structure of photosystem II at 1.95 Å resolution viewed by femtosecond X-ray pulses. *Nature* **2015**, *517*, 99–103.

(15) Xiao, D.; Gregg, J.; Lakshmi, K. V.; Bonitatibus, P. J. Bio-inspired molecular catalysts for water oxidation. *Catalyst* **2021**, *11*, 1068.

(16) Duan, L.; Wang, L.; Li, F.; Li, F.; Sun, L. Highly efficient bioinspired molecular Ru water oxidation catalysts with negatively charged backbone ligands. *Acc. Chem. Res.* **2015**, *48*, 2084–2096.

(17) Kärkäs, M. D.; Verho, O.; Johnston, E. V.; Åkermark, B. Artificial photosynthesis: molecular systems for catalytic water oxidation. *Chem. Rev.* **2014**, *114*, 11863–12001.

(18) Cao, R.; Lai, W.; Du, P. Catalytic Water Oxidation at Single Metal Sites. *Energy Environ. Sci.* **2012**, *5*, 8134–8157.

(19) Duan, L.; Fischer, A.; Xu, Y.; Sun, L., Isolated Seven-Coordinate Ru(IV) Dimer Complex with $[HOHOH]^-$ Bridging Ligand as an Intermediate for Catalytic Water Oxidation. *J. Am. Chem. Soc*. **2009**, *131*, 10397–10399.

(20) Duan, L.; Bozoglian, F.; Mandal, S.; Stewart, B.; Privalov, T.; Llobet, A.; Sun, L, A molecular ruthenium catalyst with water-oxidation activity comparable to that of photosystem II. *Nat. Chem*. **2012**, *4*, 418–423.

(21) Duan, L.; Araujo, C. M.; Ahlquist, M. S. G.; Sun, L., Highly efficient and robust molecular ruthenium catalysts for water oxidation. *Proc. Natl. Acad. Sci. USA*. **2012**, *109*, 15584–15588.

(22) Wang, L.; Duan, L.; Wang, Y.; Ahlquist, M. S. G.; Sun, L., Highly efficient and robust molecular water oxidation catalysts based on ruthenium complexes. *Chem. Commun*. **2014**, *50*, 12947–12950.

(23) Roger, I.; Symes, M. D., First row transition metal catalysts for solar-driven water oxidation produced by electrodeposition. *J. Mater. Chem. A*. **2016**, *4*, 6724–6741.

(24) Casadevall, C.; Bucci, A.; Costas, M.; Fillol, J. L. Water oxidation catalysis with well-defined molecular iron complexes. *Advances in Inorganic Chemistry* **2019**, *74*, 151–196.

(25) Ellis, W. C.; McDaniel, N. D.; Bernhard, S.; Collins, T. J. Fast water oxidation using iron. *J. Am. Chem. Soc.* **2010**, *132*, 10990–10991.

(26) Codola, Z.; Gamba, I.; Acuna-Pares, F.; Casadevall, C.; Clemancey, M.; Latour, J. -M.; Luis, J. M.; Lloret-Fillol, J.; Costas, M. Design of iron coordination complexes as highly active homogenous water oxidation catalysts by deuteration of oxidation-sensitive sites. *J. Am. Chem. Soc.* **2019**, *141*, 323–333.

(27) Liu, Y.; Xiang, R.; Du, X.; Ding, Y.; Ma, B. An efficient oxygen evolving catalyst based on a μ-O diiron coordination complex. *Chem. Commun.* **2014**, *50*, 12779.

(28) Das, B.; Lee, B. -L; Karlsson, E. A.; Akermark, T.; Shatskiy, A.; Demeshko, S.; Liao, R. -Z.; Laine, T. M.; Haukka, M.; Zeglio, E.; Abdel-Magied, A. F.; Siegbahn, P. E. M.; Meyer, F.; Karkas, M. D.; Johnston, E. V.; Nordlander, E.; Akermark, B. Water oxidation catalyzed by

molecular di- and nonanuclear Fe complexes: importance of a proper ligand framework. *Dalton Trans*. **2016**, *45*, 13289.

(29) Okamura, M.; Kondo, M.; Kuga, R.; Kurashige, Y.; Yanai, T.; Hayami, S.; Praneeth, V. K.; Yoshida, M.; Yoneda, K.; Kawata, S.; Masaoka, S. A pentanuclear iron catalyst designed for water oxidation. *Nature* **2016**, *530*, 465–468.

(30) Black, D. St. C.; Hartshorn, A. J. Ligand design and synthesis. *Coordination Chemistry Reviews*, **1973**, *9*, 219–274.

(31) Najafpour, M. M.; Moghaddam, A. N.; Sedigh, D. J.; Holynska, M. A dinuclear iron complex with a single oxo bridge as an efficient water-oxidizing catalyst in the presence of cerium(iv) ammonium nitrate: new findings and current controversies. *Catal. Sci. Technol.* **2014**, *4*, 30.

(32) Wichkramasinghe, L. D.; Zhou, R.; Zong, R.; Vo, P.; Gagnon, K. J.; Thummel, R. P. Iron Complexes of Square Planar Tetradendate Polypyridyl-Type Ligands as Catalysts for Water Oxiation. *J. Am. Chem. Soc.* **2015**, *137*, 13260–13263.

(33) Wang, J. -W.; Zhong, D. -C.; Lu, T. -B. Artificial photosynthesis: Catalytic water oxidation and CO2 reduction by dinuclear non-noble-metal molecular catalysts. *Coordination Chemistry Reviews* **2018**, *377*, 225–236.

(34) Yang, B.; Yang, Q. Q.; Jiang, X.; Chen, B.; Tung, C. H.; Wu, L. Z. Tracking the FeIV(O) intermediate and O-O bond formation of a nonheme iron catalyst for water oxidation. *Chem. Commun.* **2017**, *53*, 9063–9066.

(35) Das, B.; Lee, B. -L.; Karlsson, E. A.; Akermark, T.; Shatskiy, A.; Demeshko, S.; Liao, R. -Z.; Laine, T. M.; Haukka, M.; Zeglio, E.; Abdel-Magied, A. F.; Siegbahn, P. E. M.; Meyer, F.; Karkas, M. D.; Johnston, E. V.; Nordlander, E.; Akermark, B. Water oxidation catalyzed by

molecular di- and nonanuclear Fe complexes: importance of a proper ligand framework. *Dalton Trans* **2016**, *45*, 13289.

(36) Parent, A. R.; Nakazono, T.; Lin, S.; Utsunomiya, S.; Sakai, K. Mechanism of water oxidation by non-heme iron catalysts when driven with sodium periodate. *Dalton Trans.* **2014**, *43*, 12501.

(37) Rohner, S. S.; Kinzel, N. W.; Werle, C.; Leitner, W. Systematic ligand variation to modulate the electrochemical properties of iron and manganese complexes. *Dalton Trans.* **2019**, *48*, 13205.

(38) Parent, A. R.; Crabtree, R. H.; Brudvig, G. W. Comparison of primary oxidants for water-oxidation catalysis. *Chem. Soc. Rev.* **2013**, *42*, 2247.

(39) Codola, Z.; Gomez, L.; Kleespies, S. T.; Jr, L. Q.; Costas, M.; Lloret-Fillol, J. Evidence for an oxygen evolving iron-oxo-cerium intermediate in iron-catalysed water oxidation. *Nature communications* **2015**, *6*, 5865.

(40) Hong, D.; Mandal, S.; Yamada, Y.; Lee, Y.; Nam, W.; Llobet, A.; Fukuzumi, S. Water oxidation catalysis with nonheme iron complexes under acidic and basic conditions: homogeneous or heterogeneous? *Inorg. Chem.* **2013**, *52*, 9522–9531.

(41) Chen, G.; Chen, L.; Ng, S. -M.; Man, W. -L.; Lau, T. -C. Chemical and visible-light-driven water oxidation by iron complexes at pH 7–9: evidence for dual-active intermediates in iron-catalyzed water oxidation. *Angew. Chem. Int. Ed.* **2013**, *52*, 1789–1791.

(42) Mehrabani, S.; Bikas, R.; Zand, Z.; Mousazade, Y.; Allakhverdiev, S. I.; Najafpour, M. M. Water splitting by a pentanuclear iron complex. *International Journal of Hydrogen Energy* **2020**, *45*, 17434–17443.

(43) Hagen, K. S. Iron(II) Triflate Salts as Convenient Substitutes for Perchlorate Salts: Crystal Structures of $[Fe(H_2O)_6](CF_3SO_3)_2$ and $Fe(MeCN)_4(CF_3SO_3)_2$. *Inorg. Chem.* **2000**, *39*, 5867–5869.

(44) Terada, T.; Hirabayashi, K.; Liu, D.; Nakamura, T.; Wakimoto, T.; Matsumoto, T.; Tatsumi, K. [3:1] Site-Differentiated [4Fe-4S] Clusters Having One Carboxylate and Three Thiolates. *Inorg. Chem*. **2013**, *52*, 11997–12004.

(45) Weigel, J. A.; Holm, R. H. Intrinsic binding properties of a differentiated iron subsite in analogs of native [Fe4S4]2+ clusters. *J. Am. Chem. Soc*. **1991**, *113*, 4184–4191.

(46) Johnson, R. W.; Holm, R. H. Reaction chemistry of the iron-sulfur protein site analogs [Fe4S4(SR)4]2-. Sequential thiolate ligand substitution reactions with electrophiles. *J. Am. Chem. Soc*. **1978**, *100*, 5338–5344.

(47) Kanady, J. S.; Tsui, E. Y.; Day, M. W.; Agapie, T. A synthetic model of the Mn3Ca subsite of the oxygen-evolving complex in photosystem II. *Science* **2011**, *333*, 733–736.

(48) Karim, S.; Chakraborty, A.; Samata, D.; Zangrando, E.; Ghosh, T.; Das, D. A dinuclear iron complex as an efficient electrocatalyst for homogeneous water oxidation reaction. *Catal. Sci. Technol*. **2020**, *10*, 2830.

(49) Panchbhai, G.; Singh, W. M.; Das, B.; Jane, R. T.; Thapper, A. Mononuclear Iron Complexes with Tetraazadentate Ligands as Water Oxidation Catalysts. *Eur. J. Inorg. Chem.* **2016**, 3262–3268.

(50) Tognarelli, J. M.; Dawood, M.; Shariff, M. I. F.; Grover, V. P. B.; Crossey, M. M. E.; Cox, I. J., Taylor-Robinson S. D.; McPhail, M. J. W. Magnetic Resonance Spectroscopy: Principles and Techniques: Lessons for Clinicians. *J. Clin. Exp. Hepatol*. **2015**, *5*, 320–328.

(51) Aubin, Y.; Keire, D. A.; Marino, J. P.; Freedberg, D. L. One- and two-dimensional NMR techniques. In *Biophysical Characterization of Proteins in Developing Biopharmaceuticals*, 2nd ed.; Elsevier, 2020; pp 375–430.

(52) Qu, X.; Guo, F.; Cao, X.; Cai, S.; Chen, Z. Reconstruction of Self-Sparse 2D NMR Spectra from Undersampled Data in the Indirect Dimension. *Sensors* **2011**, *11*, 8888–8909.

(53) Lindon, J. C. NMR Spectroscopy Techniques/ Multidimensional Proton. In *Encyclopedia of Analytical Science*, 2nd ed.; Elsevier, 2005; pp 350–357.

(54) Glish, G. L.; Vachet, R. W. The basics of mass spectrometry in the twenty-first century. *Nature Reviews Drug Discovery* **2003**, *2*, 140–150.

(55) Awad, H.; Khamis, M. M.; El-Aneed, A. Mass spectroscopy, Review of the Basics: Ionization. *Applied Spectroscopy Reviews* **2014**, *50*, 158–175.

(56) Velichko, N. V.; Pinevich, A. V. Classification and Identification Tasks in Microbiology: Mass Spectrometric Methods Coming to the Aid. *Microbiology* **2019**, *88*, 534–547.

(57) Balci, M. *Basic 1H- and 13C-NMR Spectroscopy*, 1st ed; Elsevier Science, 2005.

(58) Burns, P. J.; Tsitovich, P. B.; Morrow, J. R. Preparation of a Cobalt(II) Cage: An Undergraduate Laboratory Experiment That Produces a ParaSHIFT Agent for Magnetic Resonance Spectroscopy. *J. Chem. Educ.* **2016**, 1115–1119.

(59) Parshad, B.; Prasad, S.; Bhatia, S.; Mittal, A.; Pan, Y.; Mishra, P. K.; Sharma, S. K.; Fruk, L. Non-ionic small amphiphile based nanostructures for biomedical application. *RSC Adv.* **2020**, *10*, 42098.

(60) Chowdhury, S.; Rakshit, A.; Acharjee, A.; and Saha, B. Novel Amphiphiles and Their Applications for Different Purposes with Special Emphasis on Polymeric Surfactants. *ChemistrySelect* **2019**, *4*, 6978–6995.

(61) Płociniczak, M. P.; Płaza, G. A.; Seget, Z. P.; Cameotra, S. S. Environmental Applications of Biosurfactants: Recent Advances. *Int.J.Mol.Sci.* **2011**, *12*, 633–654.

(62) Al-Dulaymi, M. A.; Chitanda, J. M.; Mohammed-Saeid, W.; Araghi, H. Y.; Verrall, R. E.; Grochulski, P.; Badea, I. Di-Peptide-Modified Gemini Surfactants as Gene Delivery Vectors: Exploring the Role of the Alkyl Tail in Their Physicochemical Behavior and Biological Activity. *The AAPS J*. **2016**, *18*, 1168–1181.

(63) Yang, J.; Yun, L.; Zhao, G.; Zhang, F.; Chen, Y.; Wang, C. Fabrication of pH-responsive system based on cationic gemini surfactant/sodium octanedioate and its application on controlled release of paclitaxel. *Colloids Surf A.* **2018**, *539*, 101–108.

(64) Kristensen, J. B.; Borjesson, J.; Maria, H.; Tjerneld, B. F.; Jorgensen, H. Use of surface active additives in enzymatic hydrolysis of wheat straw lignocellulose. *Enz. Microb. Technol.* **2007**, *40*, 888–895.

(65) Li, Y.; Sun, Z.; Ge, X.; Zhang, J. Effects of lignin and surfactant on adsorption and hydrolysis of cellulases on cellulose. *Biotechnol. Biofuels* **2016**, *9*, 1–10.

(66) Olson, M. A.; Braunschweig, A.; Ikeda, T.; Fang, L.; Trabolsi, A.; Slawin, A. M. Z.; Stoddart, J. F. Thermodynamic Forecasting of Mechanically Interlocked Switches. *Org. Biomol. Chem.* **2009**, ***7***, 4391–4405.

(67) Olson, M. A.; Coskun, A.; Klajn, R.; Fang, L.; Dey, S. K.; Browne, K.; Grzybowski, B. A.; Stoddart, J. F. "Assembly of Polygonal Nanoparticle Clusters Directed By Reversible Noncovalent Bonding Interactions" *Nano Lett.* **2009**, *9*, 3185–3190.

(68) Klajn, R.; Olson, M. A.; Fang, L.; Coskun, A.; Wesson, P. J.; Trabolsi, A.; Stoddart, J. F.; Grzybowski, B. A. On-demand Capture and Release of Metal Nanoparticles Using a Functional Polymer. *Nature Chem.* **2009**, 1, 733–738.

(69) Nagarajan, R.; Ruckenstein, E. Theory of Surfactant Self -Assembly: A Predictive Molecular Thermodynamic Approach. *Langmuir* **1991**, *7*, 2934–2969.

(70) Stephenson, B. C.; Goldsipe, A.; Beers, K. J.; Blankschtein, D. Quantifying the Hydrophobic Effect. 1. A Computer Simulation−Molecular-Thermodynamic Model for the Self-Assembly of Hydrophobic and Amphiphilic Solutes in Aqueous Solution. *J. Phys. Chem. B* **2007**, *111*, 1025–1044.

(71) Zhao, W.; Wang, Y. Coacervation with surfactants: From single-chain surfactants to gemini surfactant. *Adv. Colloid Interface Sci.* **2017**, *239*, 199–212.

(72) Krishnan, R. S. G.; Thennarasu, S.; Mandal, A. B. Self-assembling characteristics of a new nonionic gemini surfactant. *J. Phys. Chem. B* **2004**, *108*, 8806–8816.

(73) Camesano, T. A.; Nagarajan, R. Micelle formation and CMC of gemini surfactants: a thermodynamic model. *Colloid Surface A* **2000**, *167*, 165–177.

(74) Brycki, B.; Szulc, A.; Koenig, H.; Kowalczyk, I.; Pospieszny, T.; Gorka, S. Effect of the alkyl chain length on micelle formation for bis(N-alkyl-N,Ndimethylethylammonium)ether dibromides. *C. R. Chim.* **2019**, *22*, 386–392.

(75) Junior, P. B. S.; Tiera, V. A. O.; Tiera, M. J. A fluorescence probe study of gemini surfactants in aqueous solution: a comparison between n-2-n and n-6-n series of the alkanediyl-α,ω-bis (dimethylalkylammonium bromides). *Eclet. Quím*. **2007**, *32*, 47–54.

(76) Li, Y.; Li, P.; Wang, J.; Wang, Y.; Yan, H.; Thomas, R. K. Odd/even effect in the chain length on the enthalpy of micellization of gemini surfactants in aqueous solution. *Langmuir* **2005**, *21*, 6703–6706.

(77) Zhang, S.; Ding, S.; Yu, J.; Chen, X.; Lei, Q.; Fang, W. Antibacterial activity, in vitro cytotoxicity, and cell cycle arrest of gemini quaternary ammonium surfactants. *Langmuir* **2015**, *31*, 12161–12169.

(78) Grosmaire, L.; Chorro, M.; Chorro, C.; Partyka, S.; Zana, R. Alkanediyl-α,ω-bis(dimethylalkylammonium bromide) surfactants. *Journal of Colloid and Interface Science* **2002**, *246*, 175–181.

(79) Wettig, S. D.; Verrall, R. E. Thermodynamic studies of aqueous m–s–m Gemini surfactant systems. *Journal of Colloid and Interface Science* **2001**, *235*, 310–316.

(80) Garcia, M. T.; Kaczerewska, O.; Ribosa, I.; Brycki, B.; Materna, P.; Drgas, M. Hydrophilicity and flexibility of the spacer as critical parameters on the aggregation behavior of long alkyl chain cationic gemini surfactants in aqueous solution. *J. Mol. Liq.* **2017**, *230*, 453–460.

(81) Brycki, B.; Kozirog, A.; Kowalczyk, I.; Pospieszny, T.; Materna, P.; Marciniak, J. Synthesis, structure, surface and antimicrobial properties of new oligomeric quaternary ammonium salts with aromatic spacers. *Molecules* **2017**, *22*, 1810.

(82) Alvarado, R. J.; Mukherjee, J.; Pacsial, E. J.; Alexander, D.; Raymo, F. M. Self-Assembling Bipyridinium Multilayers. *J. Phys. Chem. B* **2005**, *109*, 6164–6173.

(83) Marotta, E.; Rastrelli, F.; Saielli, F. Aggregation behavior of octyl viologen di[bis(trifluoromethanesulfonyl)amide] in nonpolar solvents. *J. Phys. Chem. B* **2008**, *112*, 16566–16574

(84) Li, L. -L.; Sun, H.; Fang, C. -J.; Yuan, Q.; Sun, L. -D.; Yan, C. -H. Mesostructured Hybrids Containing Potential Donors and Acceptors with Molecular-Scale and Meso-Scale Segregation and Ordering: Toward the Development of Smart Materials through Hierarchical Self-Assembly. *Chem. Mater.* **2009**, *21*, 4589–4597.

(85) Webber, M. J.; Appel, E. A.; Meijer, E. W.; Langer, R. Supramolecular biomaterials. *Nat. Mater*. **2015**, *15*, 13.

(86) Gohy, J. -F.; Lohmeijer, B. G.; Schubert, U. S. Metallo-Supramolecular Block Copolymer Micelles. *Macromolecules* **2002**, *35*, 4560–4563.

(87) Lv, Z. -P.; Chen, B.; Wang, H. -Y.; Wu, Y.; Zuo, J. -L. Charge-Transfer Supra-Amphiphiles Built by Water-Soluble Tetrathiafulvalenes and Viologen-Containing Amphiphiles: Supramolecular Nanoassemblies with Modifiable Dimensions. *Small* **2015**, *11*, 3597–3605.

(88) Zheng, B.; Wang, F.; Dong, S.; Huang, F. Supramolecular polymers constructed by crown ether-based molecular recognition. *Chem. Soc. Rev.* **2012**, *41*, 1621–1636.

(89) Chen, Y.; Huang, F.; Li, Z. T.; Liu, Y. Controllable macrocyclic supramolecular assemblies in aqueous solution. *Sci. China Chem.* **2018**, *61*, 979–992.

(90) Diaz, A.; Quintela, P. A.; Schuette J. M.; Kaifer, A. E. Complexation of redox-active surfactants by cyclodextrins. *J. Phys. Chem.* **1988**, *92*, 3537–3542.

(91) Lee, D. K.; Kim, Y. I.; Kwon, Y. S.; Kang, Y. S.; Kevan, L. Electron Magnetic Resonance Study of the Photoreduction of Alkylviologens in Anionic Sodium Dodecyl Sulfate and Cationic Dodecyltrimethylammonium Bromide Micelles. *J. Phys. Chem. B* **1997**, *101*, 5319–5323.

(92) Li, L. -L.; Sun, H.; Fang, C. -J.; Yuan, Q.; Sun, L. -D.; Yan, C. -H. Mesostructured Hybrids Containing Potential Donors and Acceptors with Molecular-Scale and Meso-Scale Segregation and Ordering: Toward the Development of Smart Materials through Hierarchical Self-Assembly. *Chem. Mater.* **2009**, *21*, 4589–4597.

(93) Olson, M. A.; Thompson, J. R.; Dawson, T. J.; Hernandez, C. M.; Messina, M. S.; O'Neal, T. Template-directed self-assembly by way of molecular recognition at the micellar-solvent

interface: modulation of the critical micelle concentration. *Org. Biomol. Chem.* **2013**, *11*, 6483–6492.

(94) Olson, M. A.; Messina, M. S.; Thompson,m J. R.; Dawson, T. J.; Goldner, A. N.; Gaspar, D. K.; Vazquez, M.; Lehrman, J. A.; Sue, A. C.-H. Reversible Morphological Changes of Assembled Supramolecular Amphiphiles Triggered by pH-Modulated Host-Guest Interactions. *Org. Biomol. Chem.* **2016**, *14*, 5714–5720.

(95) Wang, Z.; Cui, H.; Sun, Z.; Roch, L. M.; Goldner, A. N.; Nour, H. F.; Sue, A. C.-H.; Baldridge, K. K.; Olson, M. A. Melatonin-Directed Micellization: A Case for Tryptophan Metabolites and their Classical Bioisosteres as Templates for the Self-Assembly of Bipyridinium-Based Supramolecular Amphiphiles in Water. *Soft Matter*. **2018**, 14, 2893–2905.

(96) Sun, Z.; Xi, L.; Zheng, K.; Zhang, Z.; Baldridge, K. K.; Olson, M. A. "Classical and Non-Classical Melatonin Receptor Agonist-Directed Micellization of Bipyridinium-Based Supramolecular Amphiphiles in Water" *Soft Matter*. **2020**, *16*, 4788–4799.

(97) Yuan, T; Vazquez, M.; Goldner, A. N.; Xu, Y.; Contrucci, R.; Firestone, M. A.; Olson, M. A. Fang, L. Versatile Thermochromic Supramolecular Materials Based on Competing Charge Transfer Interactions. *Adv. Funct. Mater*. **2016**, *47*, 8604–8612.

(98) Xu, Y.; Yuan, T.; Nour, H. F.; Fang, L.; Olson, M. A. Bis-Bipyridinium Gemini Surfactant-Based Supramolecular Helical Fibers and Solid State Thermochromism. *Chem. Eur. J*. **2018**, *24*, 16553–16557.

(99) Shanks, P. C.; Franses, E. I. Estimation of micellization parameters of aqueous sodium dodecyl sulfate from conductivity data. *J. Phys. Chem.* **1992**, *96*, 1794–1805.

(100) Cornellas, A.; Perez, L.; Comelles, F.; Ribosa, I.; Manresa, A.; Garcia, M. T. Self-aggregation and antimicrobial activity of imidazolium and pyridinium based ionic liquids in aqueous solution. *J. Colloid Interface Sci.* **2011**, *355*, 164–171.

(101) Gonzalez-perez, A.; Czapkiewicz, J.; Ruso, J. M.; Rodriguez, J. R. Temperature Dependence of Second Critical Micelle Concentration of Dodecyldimethylbenzylammonium Bromide in Aqueous Solution. *Colloid and Polymer Science* **2004**, *282*, 1169–1173.

(102) Zana, R. Critical Micellization Concentration of Surfactants in Aqueous Solution and Free Energy of Micellization. *Langmuir* **1996**, *12*, 1208–1211.

(103) Das, A.; Ghosh, S. Supramolecular assemblies by charge-transfer interactions between donor and acceptor chromophores. *Angew. Chem. Int. Ed.* **2014**, *53*, 2038–2054.

(104) Basu, S.; Coskun, A.; Friedman, D. C.; Olson, M. A.; Benitez, D.; Tkachouk, E.; Barin, G.; Young, J.; Fahrenbach, A. C.; Goddard III, W. A.; Stoddart, J. F. Donor–Acceptor Oligorotaxanes Made to Order. *Chem. Eur. J.* **2011**, *17*, 2107–2119.

APPENDIX A

DESIGN AND SYNTHESIS OF DINUCLEATING LIGAND TO CONSTRUCT DIIRON COMPLEXES AS WATER OXIDATION CATALYSTS FOR ENERGY APPLICATIONS

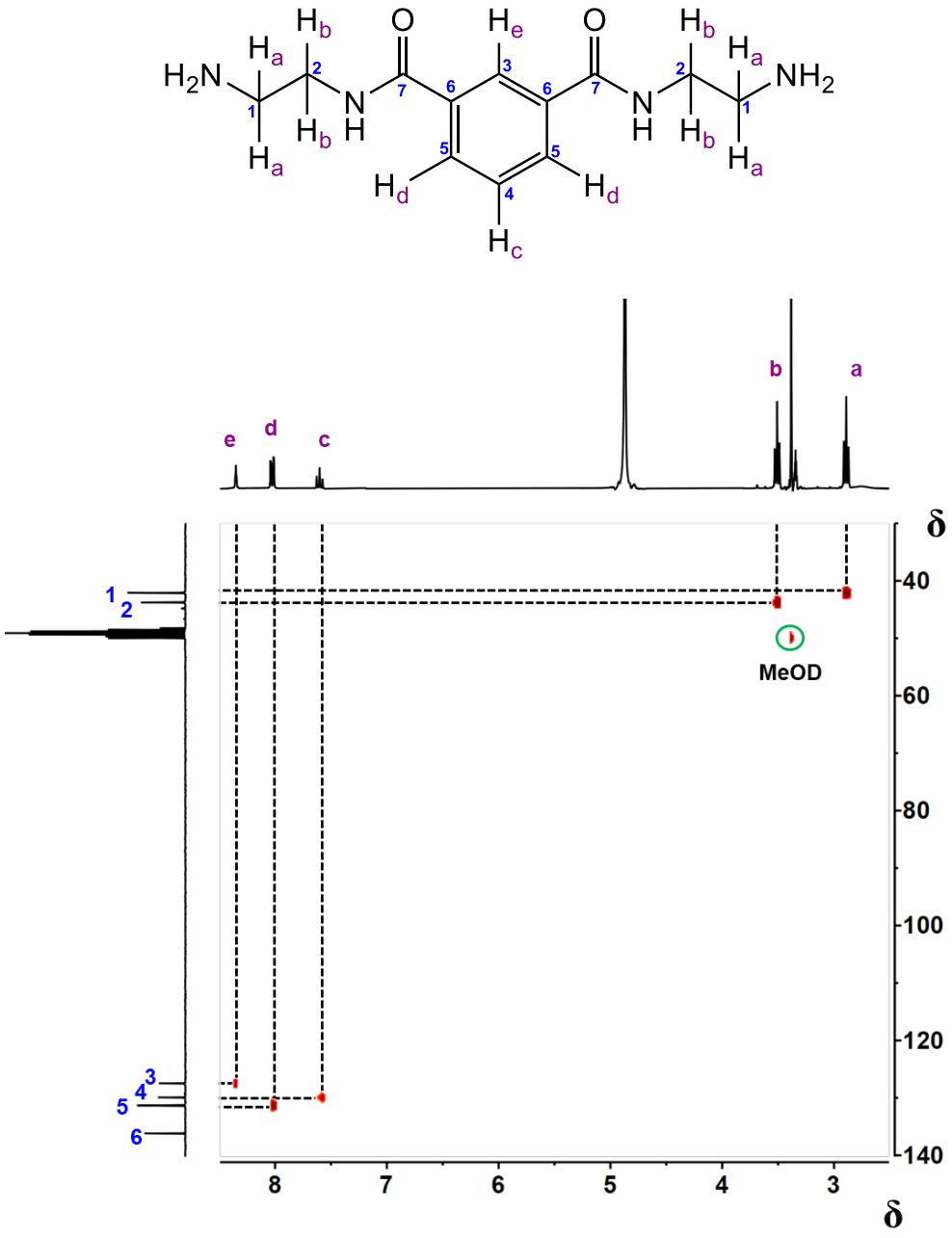

Figure S1. ^{1}H-^{13}C HSQC NMR spectrum (bottom) of *N*^{1}, *N*^{3}-Bis(2-aminoethyl)isophthalamide (top) (MeOD, 25°C). Carbons at position 7 was cut out of the spectrum because it had no correlation with any proton.

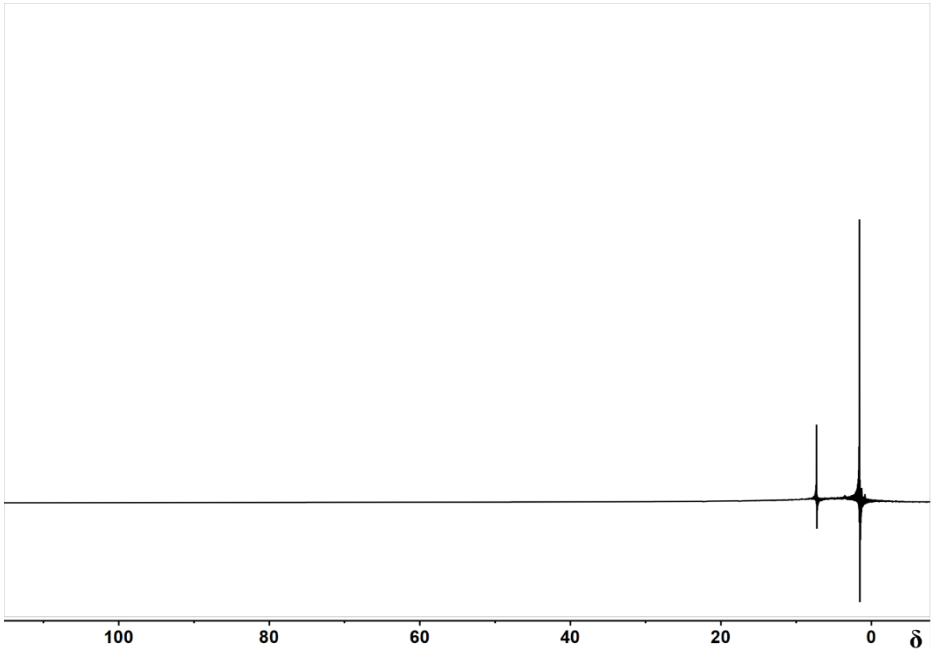

Figure S2. ^{1}H-NMR spectrum of $Fe_2(OTf)_n(L1)$ complex.

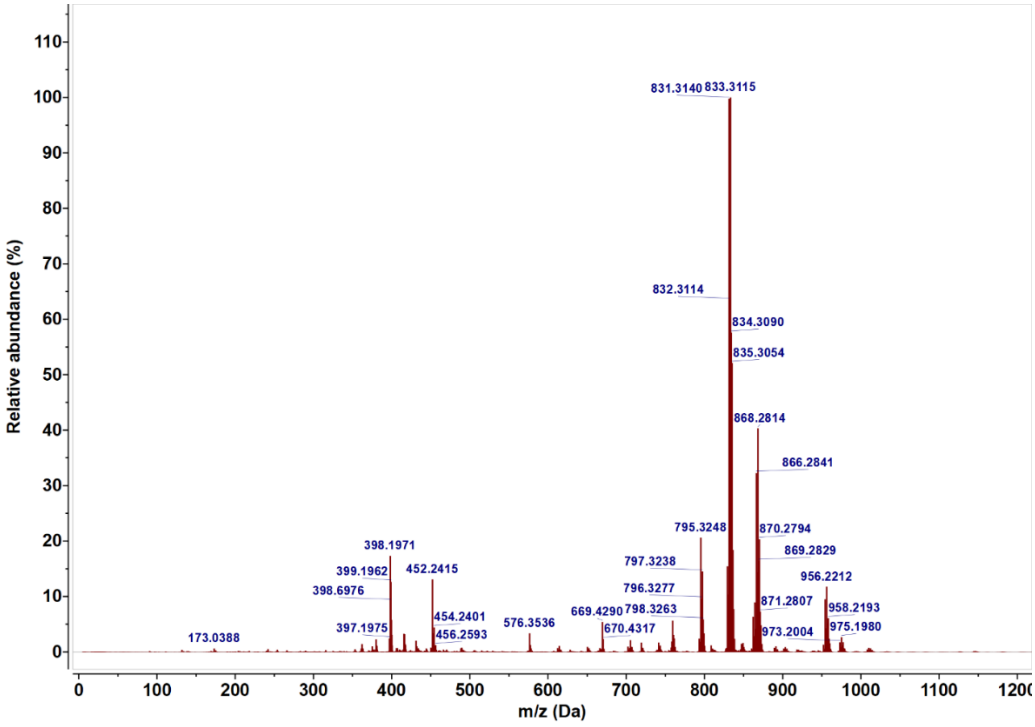

Figure S3. Mass spectrum of the iron complex formed by mixing iron(II) triflate with the ligand. There was no peak that matched to any of the expected m/z values of the expected diiron complexes.

APPENDIX B

THE DEVELOPMENT OF ALKYL-BRIDGED BIS-BIPYRIDINIUM-BASED AMPHIPHILES FOR TEMPLATE-DIRECTED SELF-ASSEMBLY

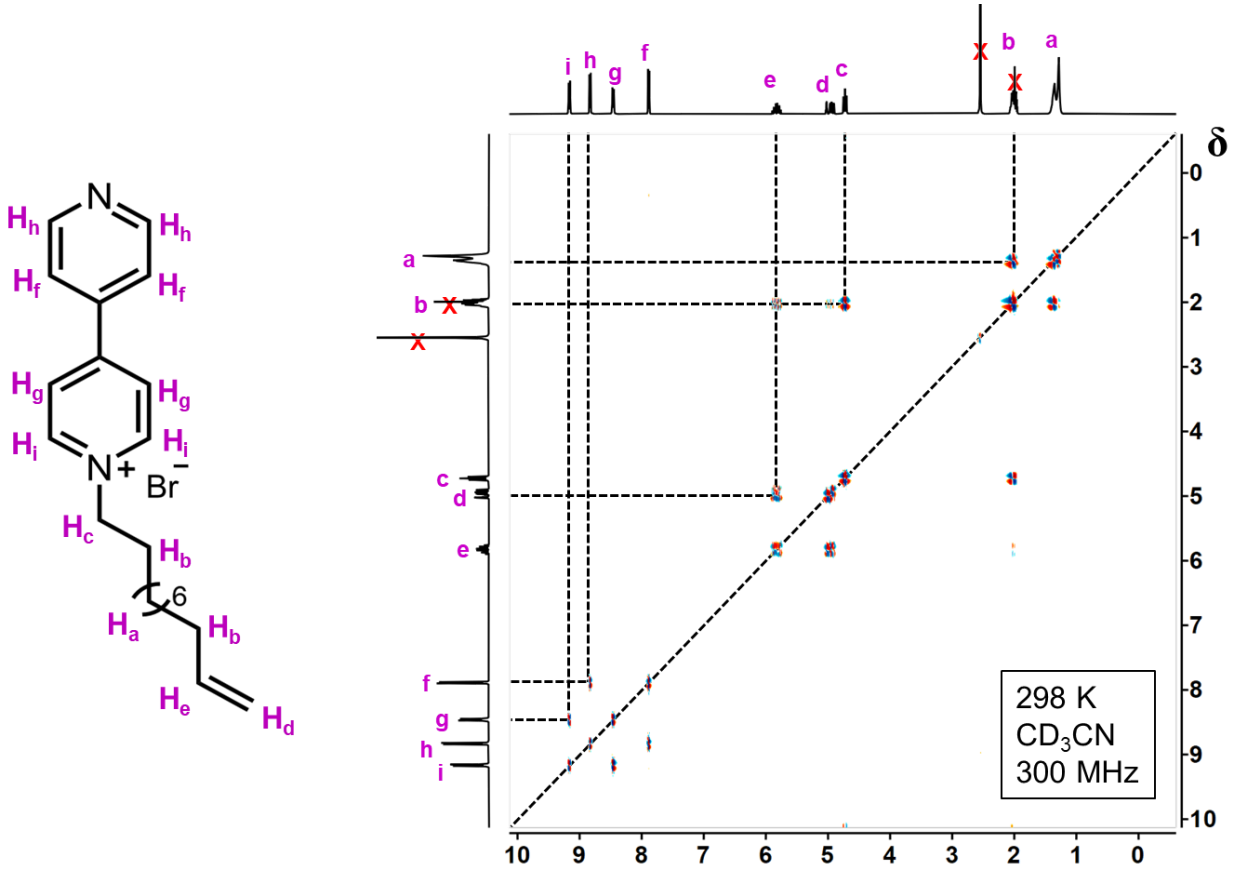

Figure S4. 2D COSY NMR spectrum of the mono-undecylated bipyridine $\mathbf{2}^{1+}$ (CD_3CN, 25°C)

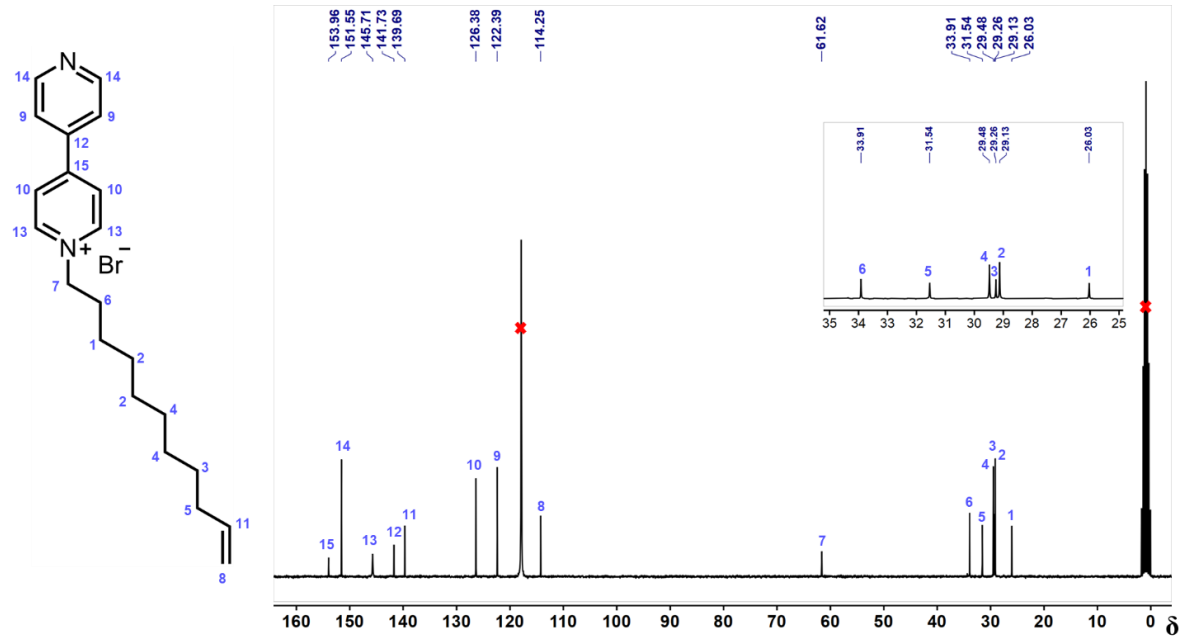

Figure S5. ^{13}C-NMR NMR spectrum of the mono-undecylated bipyridine $\mathbf{2}^{1+}$ (CD_3CN, 25°C)

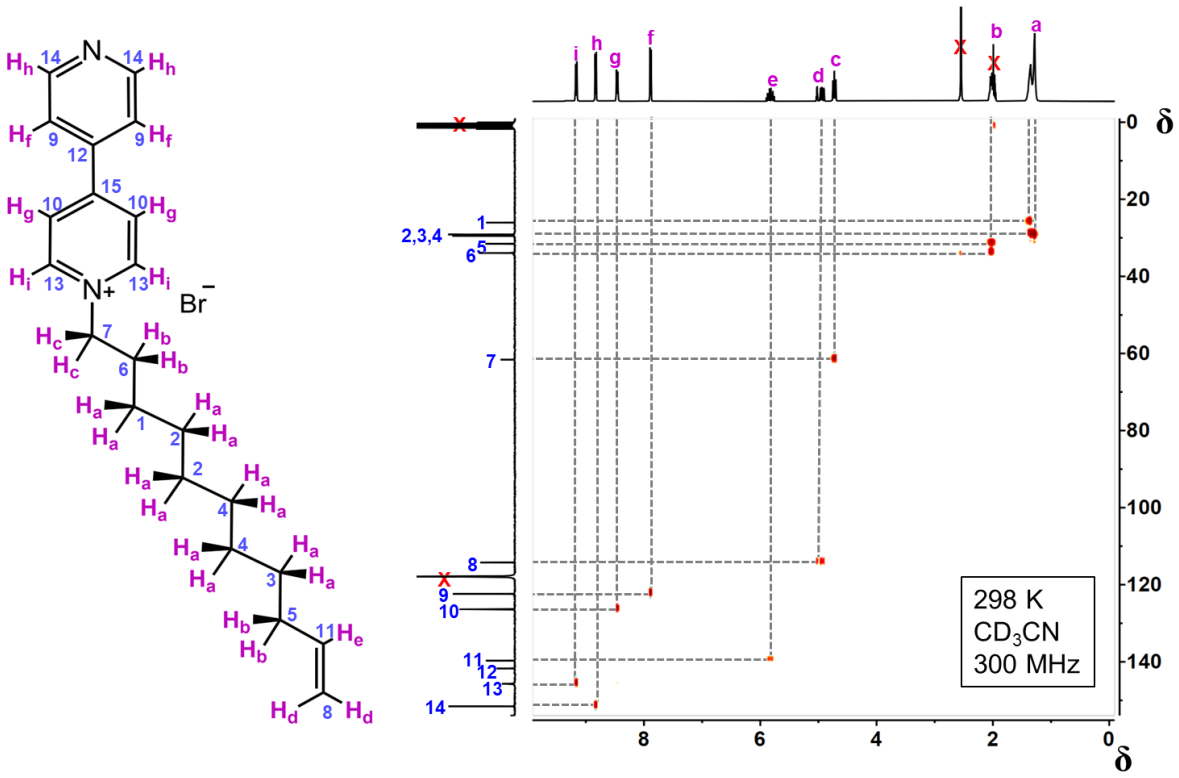

Figure S6. 2D HSQC NMR spectrum of the mono-undecylated bipyridine $\mathbf{2}^{1+}$ (CD_3CN, 25°C)

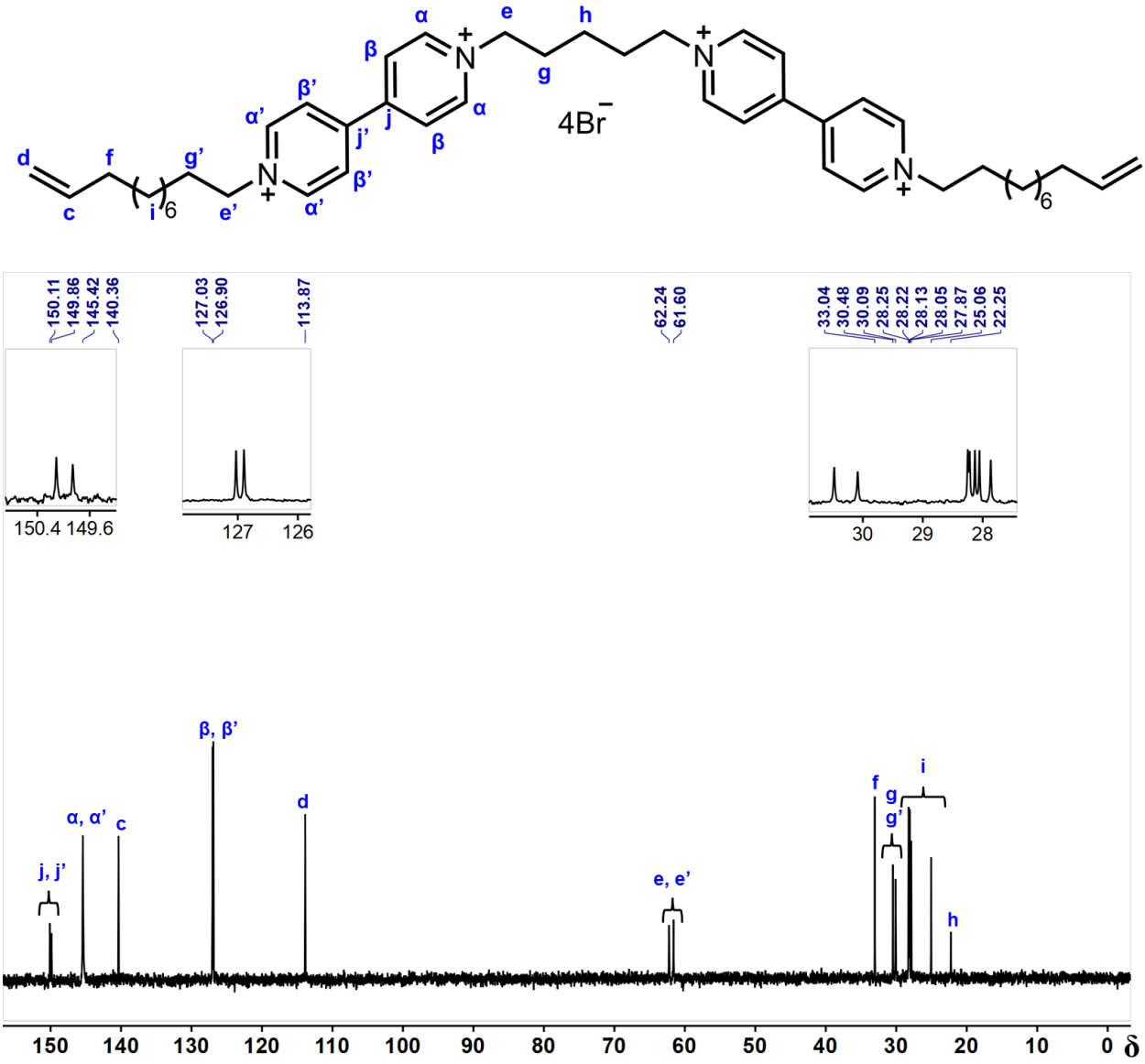

Figure S7. ^{13}C NMR of the 5-carbon-akyl-bridged bis-bipyridinium-based gemini amphiphile $\mathbf{5}^{4+}$ (D_2O, 25°C).

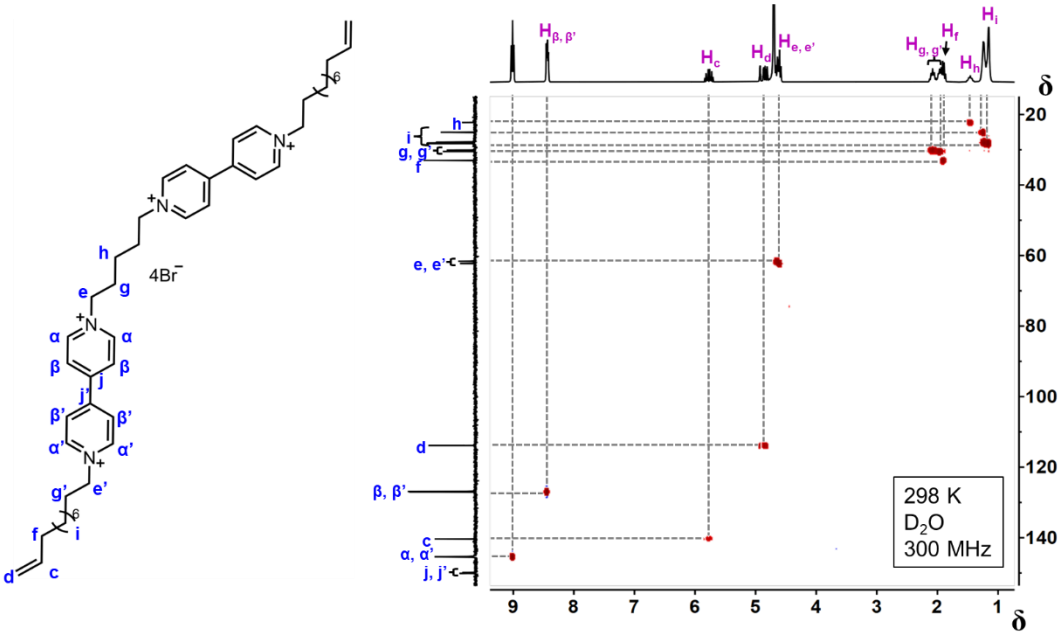

Figure S8. 2D HSQC NMR of the 5-carbon-akyl-bridged bis-bipyridinium-based gemini amphiphile $\mathbf{5}^{4+}$ (D_2O, 25°C).

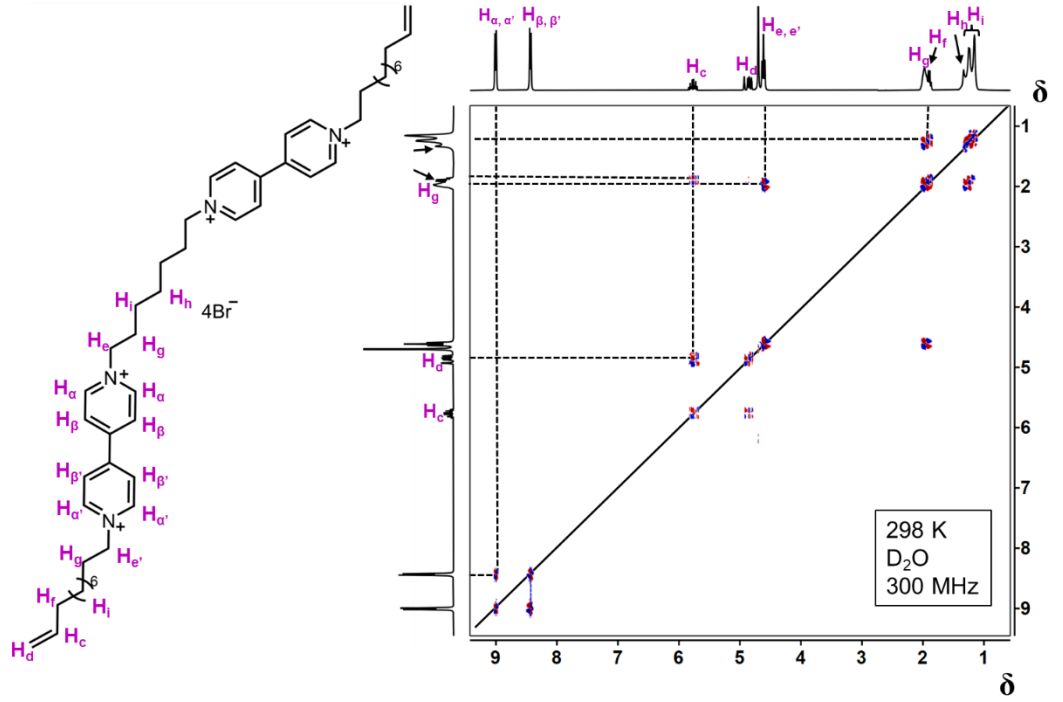

Figure S9. 2D COSY NMR of the 7-carbon-akyl-bridged bis-bipyridinium-based gemini amphiphile $\mathbf{7}^{4+}$ (D_2O, 25°C).

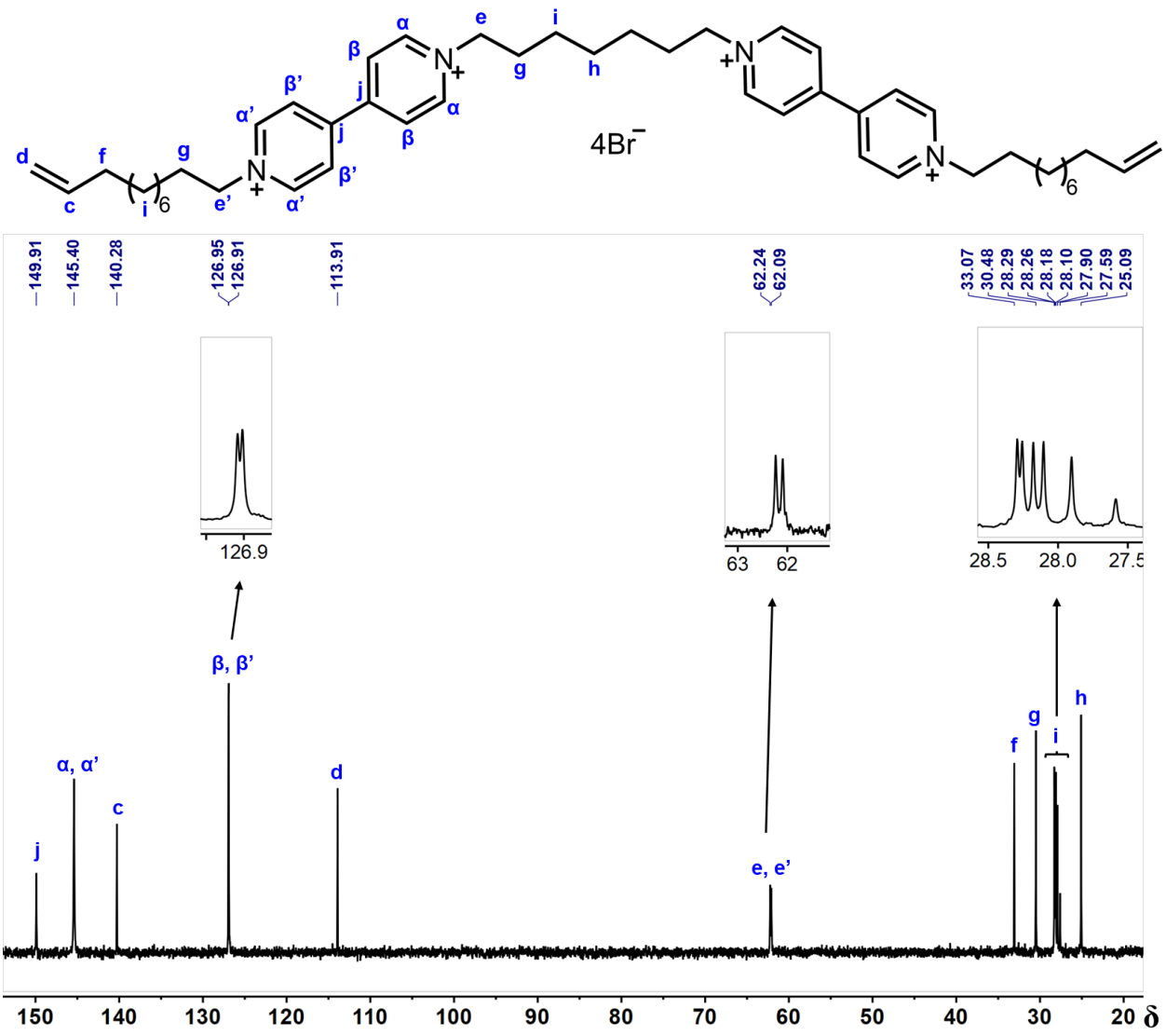

Figure S10. ^{13}C NMR of the 7-carbon-akyl-bridged bis-bipyridinium-based gemini amphiphile $\mathbf{7}^{4+}$ (D_2O, 25°C).

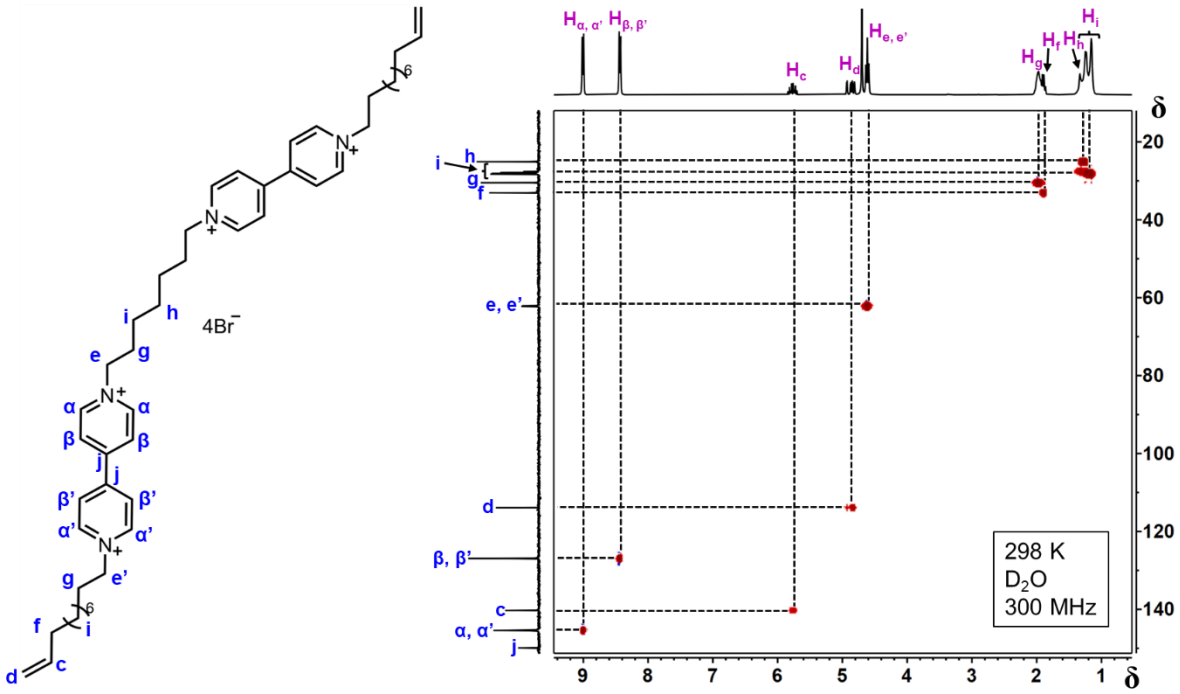

Figure S11. 2D HSQC NMR of the 7-carbon-akyl-bridged bis-bipyridinium-based gemini amphiphile $\mathbf{7}^{4+}$ (D_2O, 25°C).

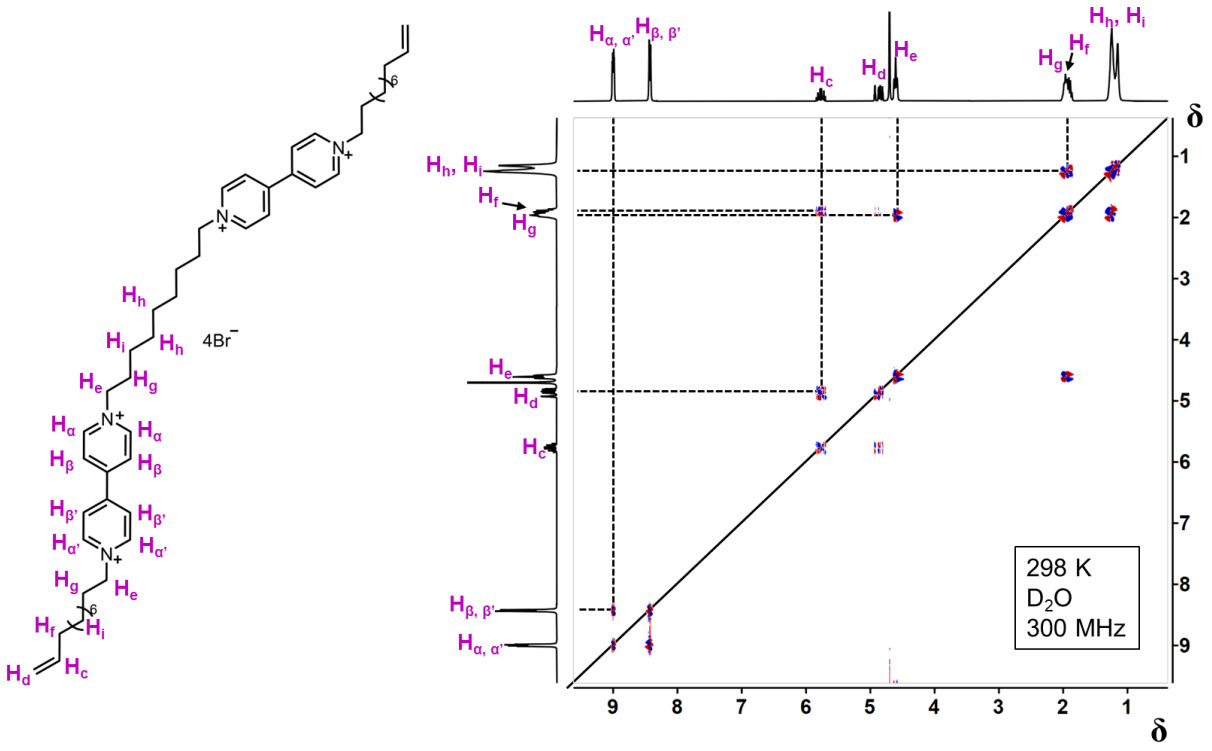

Figure S12. 2D COSY NMR spectrum of the 9-carbon-akyl-bridged bis-bipyridinium-based gemini amphiphile $\mathbf{9}^{4+}$ (D_2O, 25°C).

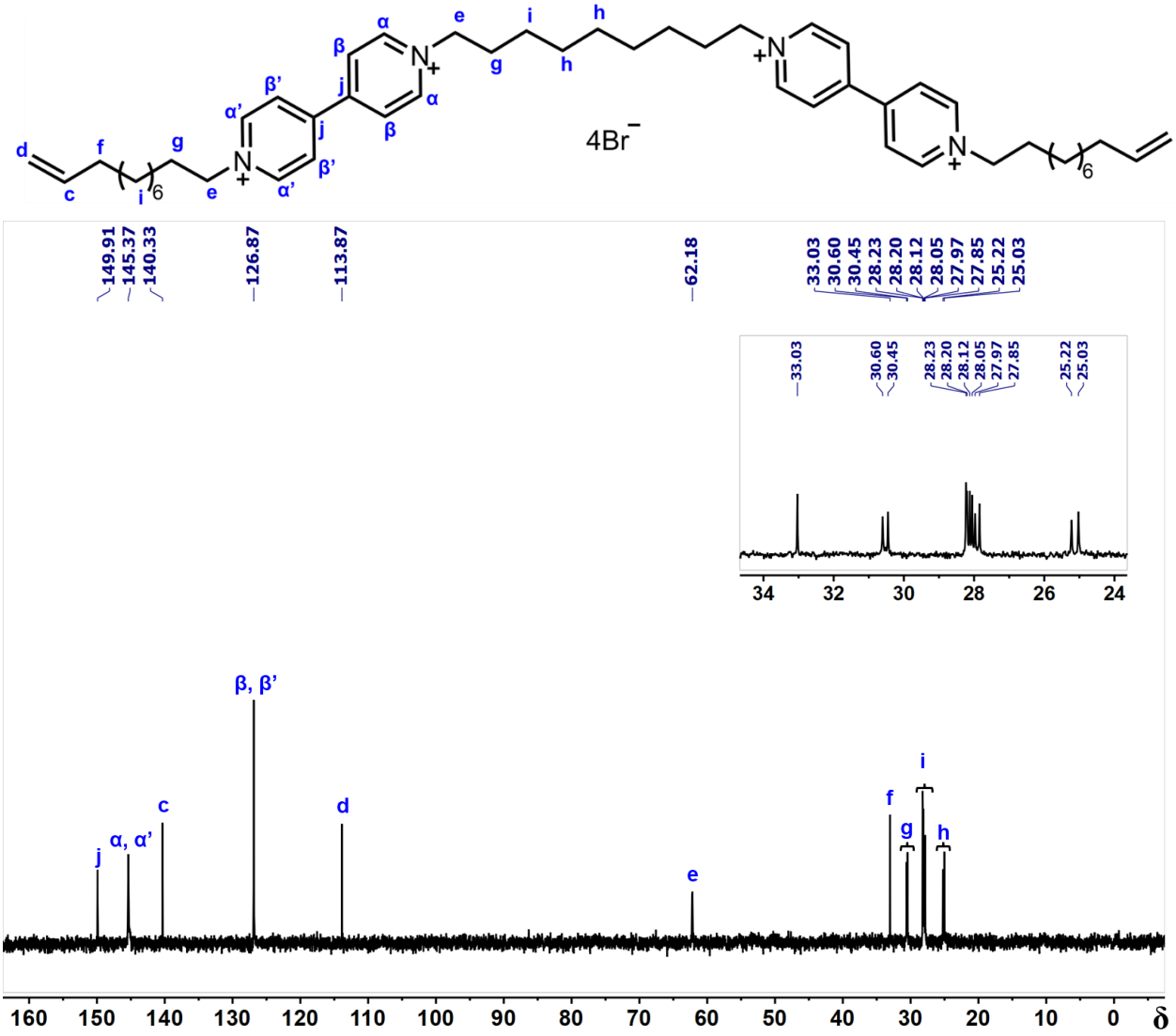

Figure S13. ^{13}C NMR spectrum of the 9-carbon-akyl-bridged bis-bipyridinium-based gemini amphiphile $\mathbf{9}^{4+}$ (D_2O, 25°C).

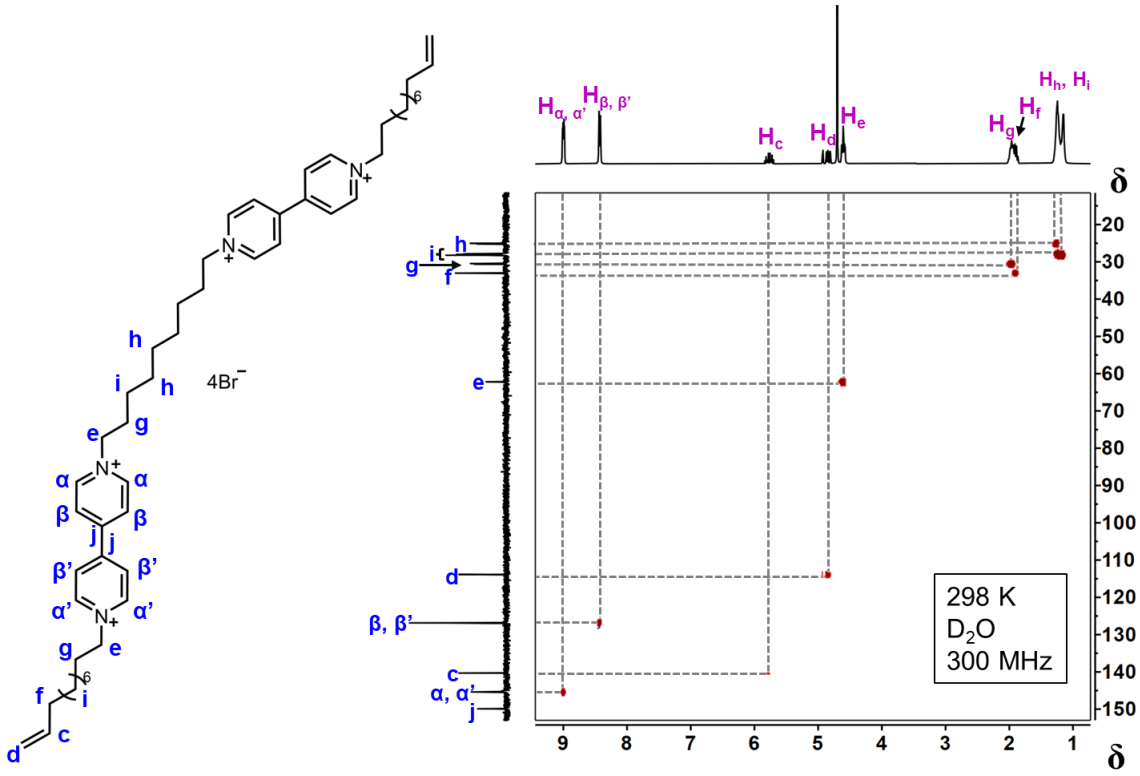

Figure S14. 2D HSQC NMR spectrum of the 9-carbon-akyl-bridged bis-bipyridinium-based gemini amphiphile $\mathbf{9}^{4+}$ (D_2O, 25°C).

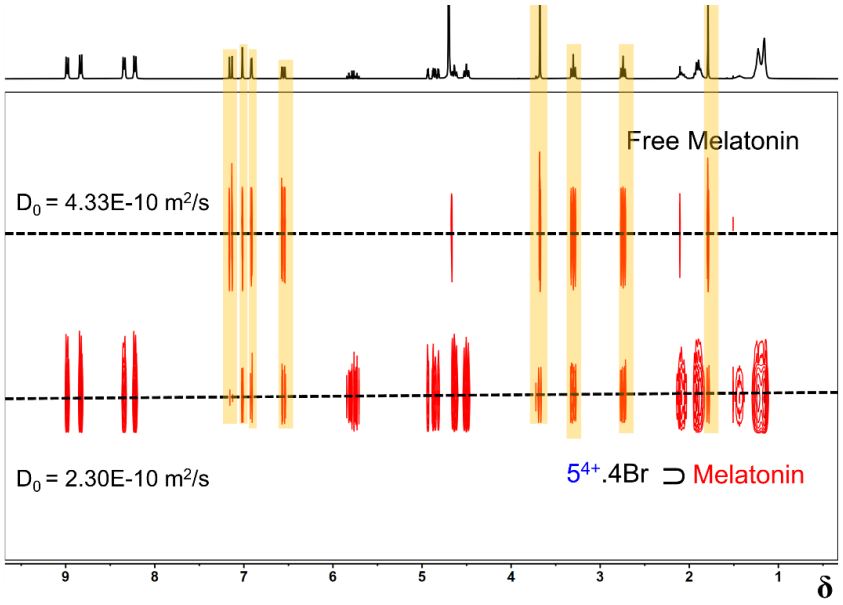

Figure S15. DOSY of mixed solution of $\mathbf{5}^{4+}$ and melatonin. Yellow highlighted regions represent the proton signals come from melatonin in the donor-acceptor charge-transfer complex $\mathbf{5}^{4+}\cdot$4Br ⊃ Melatonin.

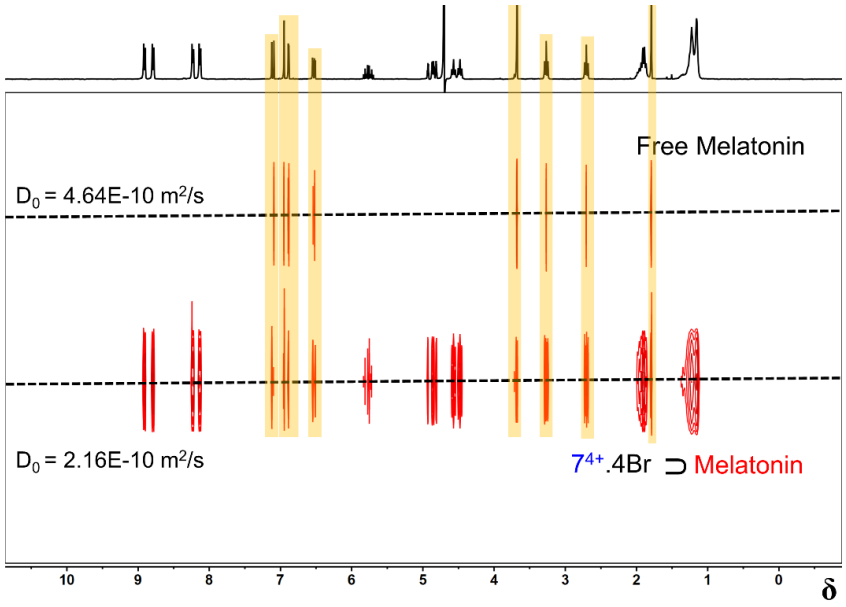

Figure S16. DOSY of mixed solution of $\mathbf{7}^{4+}$ and melatonin. Yellow highlighted regions represent the proton signals come from melatonin in the donor-acceptor charge-transfer complex $\mathbf{7}^{4+}\cdot$4Br ⊃ Melatonin.

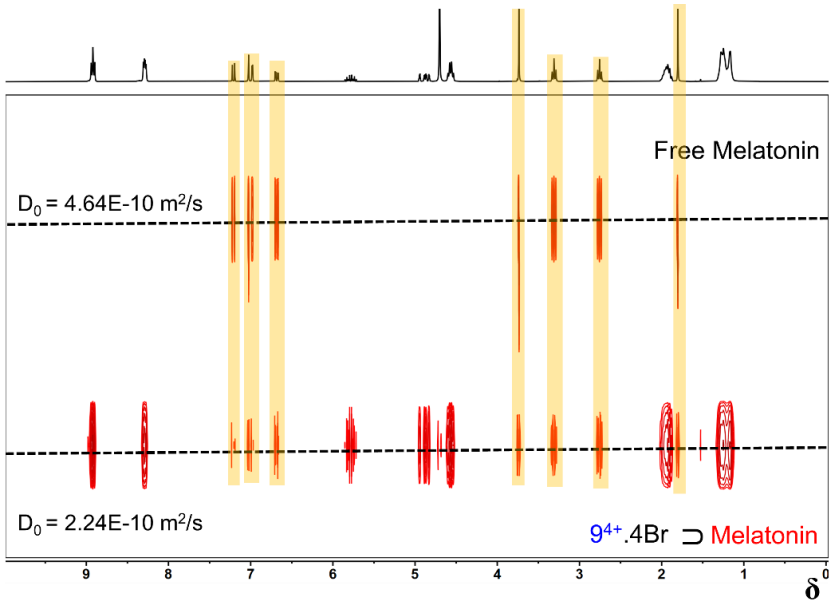

Figure S17. DOSY of mixed solution of $\mathbf{9}^{4+}$ and melatonin. Yellow highlighted regions represent the proton signals come from melatonin in the donor-acceptor charge-transfer complex $\mathbf{9}^{4+}\cdot$4Br ⊃ Melatonin.